12-2012

Radiative Double Electron Capture in Collisions of Fully-Stripped Fluorine Ions with Thin Carbon Foils

Tamer Mohammad Samy Elkafrawy
Western Michigan University, tamer_elkafrawy@hotmail.com

RADIATIVE DOUBLE ELECTRON CAPTURE IN COLLISIONS OF FULLY-STRIPPED FLUORINE IONS WITH THIN CARBON FOILS

by

Tamer Mohammad Samy Elkafrawy

A Dissertation
Submitted to the
Faculty of The Graduate College
in partial fulfillment of the
requirements for the
Degree of Doctor of Philosophy
Department of Physics
Advisor: John A. Tanis, Ph.D.

Western Michigan University
Kalamazoo, Michigan
December 2012

RADIATIVE DOUBLE ELECTRON CAPTURE IN COLLISIONS OF FULLY-STRIPPED FLUORINE IONS WITH THIN CARBON FOILS

Tamer Mohammad Samy Elkafrawy, Ph.D.

Western Michigan University, 2012

Radiative double electron capture (RDEC) is a one-step process in ion-atom collisions occurring when two target electrons are captured to a bound state of the projectile simultaneously with the emission of a single photon. The emitted photon has approximately double the energy of the photon emitted due to radiative electron capture (REC), which occurs when a target electron is captured to a projectile bound state with simultaneous emission of a photon. REC and RDEC can be treated as time-reversed photoionization (PI) and double photoionization (DPI), respectively, if loosely-bound target electrons are captured. This concept can be formulated with the principle of detailed balance, in which the processes of our interest can be described in terms of their time-reversed ones. Fully-stripped ions were used as projectiles in the performed RDEC experiments, providing a recipient system free of electron-related Coulomb fields. This allows the target electrons to be transferred without interaction with any of the projectile electrons, enabling accurate investigation of the electron-electron interaction in the vicinity of electromagnetic field.

In this dissertation, RDEC was investigated during the collision of fully-stripped fluorine ions with a thin carbon foil and the results are compared with the recent experimental and theoretical studies. In the current work, x rays associated with projectile charge-changing by single and double electron capture and no charge change by F^{9+} ions were observed and compared with recent work for O^{8+} ions and

with theory. Both the F^{9+} and O^{8+} ions had energies in the ~MeV/u range. REC, in turn, was investigated as a means to compare with the theoretical predictions of the RDEC/REC cross section ratio. The most significant background processes including various mechanisms of x-ray emission that may interfere with the energy region of interest are addressed in detail. This enables isolation of the contributions of REC and RDEC from the entire continuous spectrum of x-ray emission or at least ensures that the background processes have negligible contribution to the energy range of interest. Special emphasis is given to showing how the data analysis was carried out by the subtraction of the x rays due to contamination lines.

THE GRADUATE COLLEGE
WESTERN MICHIGAN UNIVERSITY
KALAMAZOO, MICHIGAN

Date 11/15/2012

WE HEREBY APPROVE THE DISSERTATION SUBMITTED BY

Tamer Mohammad Samy F. Elkafrawy

ENTITLED RADIATIVE DOUBLE ELECTRON CAPTURE IN COLLISIONS OF FULLY-STRIPPED FLUORINE IONS WITH THIN CARBON FOILS

AS PARTIAL FULFILLMENT OF THE REQUIREMENTS FOR THE

DEGREE OF Doctor of Philosophy

Physics
(Department)

John. A. Tanis, Ph.D.
Dissertation Review Committee Chair

Physics
(Program)

Thomas W. Gorczyca, Ph.D.
Dissertation Review Committee Member

Asghar N. Kayani, Ph.D.
Dissertation Review Committee Member

Murtadha A. Khakoo, Ph.D.
Dissertation Review Committee Member

Andrzej S. Warczak, Ph.D.
Dissertation Review Committee Member

APPROVED

Dean of The Graduate College

Date December 2012

ACKNOWLEDGMENTS

My first appreciation goes with no doubt to my dissertation supervisor, Prof. John A. Tanis, who acted to me as a role model of the genuine scientist. I would like to express my immense gratitude and high appreciation to all the deep discussions and the efforts he has done with me till the present PhD thesis took this shape. I learned much and benefitted a lot from him and it was my honor and pleasure working with him until the current work is done beautifully. On this path, I can never deny or forget the efforts done by the deceased Prof. Gaber Omar, the main supervisor of my Master thesis, on the field of theoretical atomic collisions at Ain Shams University, Egypt. He was the one who first introduced this field to me, which was the starting point of my career. Prof. Hassan Ramadan as an atomic-physics theoretician had a very special role supervising my Master thesis as a co-advisor, giving his full support, and always encouraging me. He guided my first steps in this research field and offered endless assistance throughout these years.

Special thanks go to Dr. Asghar N. kayani, the director of WMU accelerator facility, who has been always in support to my experimental work by teaching me the operation of the WMU accelerator facility, getting and tuning the produced beam, maintaining the ion source, and taking care of any serious or unexpected problems during the beam time given to my experiment. I am grateful to Prof. Andrzej S. Warczak for all the valuable discussions and communications related to the current work. I was lucky to have him on my dissertation committee as an expert on the topic of my dissertation. It was our pleasure that he was our collaborator over the past few years. I am also deeply indebted to Prof. Thomas W. Gorczyca and Prof. Murtadha A.

Khakoo for their distinctive role as dissertation committee members as well as for all the fruitful discussions, guidance, and continuing support. My sincere thanks should go to Allan Kern for his vital role as the accelerator engineer and Rick Welch, the machine shop supervisor, for designing the frames and ladder for the carbon foils.

My deep gratitude goes to Prof. Dean Halderson not only as an ideal model of the graduate advisor but also as a distinguished instructor of EM and QM graduate courses. I'm also very grateful to the former department chairman, Prof. Paul Pancella and the present chairperson, Prof. Kirk Korista, for their massive support and encouragement throughout my PhD journey. They never said NO when it was possible. I cannot also forget all the efforts done by our office coordinator Lori Krum, the former office assistant Kerry Kochran, the present office assistant Katie Easley, the deceased former manager of the undergraduate physics laboratories Robert Scherzer, and the electronics shop supervisor Benjamin Gaudio.

My thanks are extended to my Department of Physics at Ain Shams University, Cairo, Egypt for all kinds of support I was provided with over the entire period of my PhD dissertation. My sincere friends and colleagues are too many to mention them all but any help or support was provided from their side are highly appreciated. The real thanks and the deepest gratitude have to go to my mother and father, who brought me up and were the reason of every step of success I have achieved. No word can describe my wife's endless efforts and support throughout my PhD path. Simply, I would not have done my PhD without her. All of my mother, father, brother, sister, wife, and lovely children have been the light of my life.

Tamer Mohammad Samy Elkafrawy

TABLE OF CONTENTS

ACKNOWLEDGMENTS ii

LIST OF TABLES vii

LIST OF FIGURES viii

CHAPTER

I. INTRODUCTION 1

II. RADIATIVE SINGLE AND DOUBLE ELECTRON CAPTURE 7

2.1 Compton Profile 7

2.2 Radiative Electron Capture (REC) 9

2.2.1 Kinematics of REC 9

2.2.2 REC Cross Section 12

2.2.3 Angular Distribution of REC Photon Emission 16

2.3 Radiative Double Electron Capture (RDEC) 19

2.3.1 Kinematics of RDEC 19

2.3.2 The First Experiment Dedicated to RDEC: Testing the Principle of Detailed Balance 22

2.3.3 Yakhontov Predictions of RDEC/REC Ratio: Nonrelativistic Approach versus Relativistic Enhancement Prediction 24

2.3.4 The Second Attempt to Observe RDEC: Testing Yakhontov Approach 25

2.3.5 Mikhailov Nonrelativistic Approach versus Modulated Relativistic Enhancement Prediction for RDEC into the Projectile K-shell 27

Table of Contents—continued

CHAPTER

2.3.6 Nefiodov Nonrelativistic Approach for RDEC into the Projectile Metastable State $1s^1 2s^1$ 31

2.3.7 The First Observation of RDEC 33

2.3.8 The Most Recent Theoretical Model of RDEC 35

III. BACKGROUND PROCESSES 40

3.1 X-ray Emission from Bremsstrahlung 40

3.1.1 Electron-nucleus (e-n) Bremsstrahlung 41

3.1.2 Nucleus-nucleus (n-n) Bremsstrahlung 50

3.1.3 Nucleus-nucleus (n-n) versus Electron-nucleus (e-n) Bremsstrahlung 52

3.1.4 Electron-electron Bremsstrahlung 54

3.2 Nonradiative Electron Capture (NRC) 56

3.3 Double Radiative Electron Capture (DREC) 59

3.4 Pileup Effect 62

IV. EXPERIMENTAL SETUP 64

4.1 Standard Van de Graaff Generator 64

4.2 Tandem Van de Graaff Accelerator 66

4.3 SNICS Negative Ion Source 67

4.4 WMU Van de Graaff Accelerator Facility 69

4.5 Experiment Setup 70

4.6 Si(Li) X-ray Detector 73

4.7 Silicon Surface Barrier Particle Detector 74

Table of Contents—continued

CHAPTER

4.8 Data Acquisition System 74

4.9 Data Analysis 78

V. DATA ANALYSIS AND DISCUSSION 81

5.1 Singles Measurements of X-ray Emission versus PIXE Analysis 82

5.2 Generating X-ray Spectra Associated with Projectile Charge-changing 87

5.3 REC Analysis 90

5.4 RDEC Analysis 95

5.5 Analysis for Background Processes 100

5.6 RDEC Cross Sections 102

5.6.1 Total RDEC Cross Sections 102

5.6.2 The Ratio $R = \sigma_{RDEC}^{1s^2} / \sigma_{REC}^{1s}$ 104

5.6.3 The Ratio $R' = \sigma_{RDEC}^{1s^1 2s^1} / \sigma_{REC}^{1s}$ 105

5.6.4 The Ratio $R'' = \sigma_{RDEC}^{1s^1 2s^1} / \sigma_{RDEC}^{1s^2}$ 105

VI. CONCLUSION 109

APPENDIX

A. List of Abbreviations 112

BIBLIOGRAPHY 114

LIST OF TABLES

2.1 Measured versus calculated (from Bethe-Salpeter) total K-REC cross sections for the experiments discussed in Secs. 2.3.2 and 2.3.4. 33

2.2 Measured versus calculated KL-RDEC and KK-RDEC cross sections for the experiments discussed in Secs. 2.3.2 and 2.3.4. 38

2.3 Measured versus calculated RDEC/REC cross section ratios $R = \sigma_{RDEC}^{1s^2} / \sigma_{REC}^{1s}$ and $R' = \sigma_{RDEC}^{1s^1 2s^1} / \sigma_{REC}^{1s}$ as well as the KL-RDEC/KK-RDEC cross section ratio $R'' = \sigma_{RDEC}^{1s^1 2s^1} / \sigma_{RDEC}^{1s^2}$ for the experiments discussed in Secs. 2.3.2 and 2.3.4. 39

3.1 Cross-section scaling for the atomic processes of interest..... 62

5.1 Calculated energies given in ascending order of all x-ray emission lines for 2.21 MeV/u F^{9+} + C in the range of interest (up to 5 keV) as well as the ^{55}Fe lines. 87

5.2 Measured versus calculated (from Bethe-Salpeter) total K-REC cross sections for the four conducted RDEC experiments. 94

5.3 Distribution of RDEC counts based on the analysis trials given in Fig. 5.7..... 99

5.4 Cross sections and the corresponding probabilities in descending order for REC, RDEC, and the other background processes for 2.21 MeV/u F^{9+} + C..... 103

5.5 Measured versus calculated KL-RDEC and KK-RDEC cross sections for the four conducted RDEC experiments. 107

5.6 Measured versus calculated RDEC/REC cross section ratios $R = \sigma_{RDEC}^{1s^2} / \sigma_{REC}^{1s}$ and $R' = \sigma_{RDEC}^{1s^1 2s^1} / \sigma_{REC}^{1s}$ as well as KL-RDEC/KK-RDEC cross section ratio $R'' = \sigma_{RDEC}^{1s^1 2s^1} / \sigma_{RDEC}^{1s^2}$ for the four conducted RDEC experiments. 108

LIST OF FIGURES

2.1 Compton profile of the carbon atom in the amorphous state as calculated from Ref. [63]. 8

2.2 Schematic diagram for the atomic process REC into a fully-stripped ion showing electron capture and photon emission by a passing ion. 11

2.3 X rays in coincidence measurements at 132° for U^{92+} + N_2 at collision energies 49, 68, 220, and 358 MeV. 13

2.4 Angular distribution of x rays due to REC for S ions in collisions with C (left panel) and Ni (right panel) targets at (a) 20, (b) 30, and (c) 115 MeV. 17

2.5 Calculated angular distributions of x rays due to K-REC (upper panel), L-REC (middle panel) and M-REC (lower panel) for tin ions at collision energies of 20, 100, and 300 MeV/u. 18

2.6 Same as Fig. 2.2 but for the atomic process RDEC. Here the capture of two electrons is shown accompanied by the emission of a single photon of about twice the energy of REC. 20

2.7 X rays emitted for Ar^{18+} + C collisions at 11.4 MeV/u. 23

2.8 Spectrum of x rays associated with double capture (U^{90+}) emitted due to the collision of U^{92+} with Ar at 297 MeV/u. 26

2.9 The universal quantities of $Q(\kappa)$ (left panel) and $Q(\kappa)/H(\kappa)$ (right panel) as functions of Sommerfeld parameter κ. 29

2.10 The ratio $R'' = \sigma_{RDEC}^{1s^1 2s^1} / \sigma_{RDEC}^{1s^2}$ as a function of Sommerfeld parameter κ. 32

2.11 The universal quantities of $F(\kappa)$ (left panel) and $F(\kappa)/H(\kappa)$ (right panel) as functions of Sommerfeld parameter κ. 32

2.12 X rays associated with (a) double capture and (b) single capture for O^{8+} + C at 38 MeV. 35

3.1 Schematic showing the hyperbolic trajectory of the incoming electron in e-n bremsstrahlung, where *b* is the impact parameter, *Z* is the atomic number of the target atom and *e* is the charge of the incident electron. 42

3.2 Bremsstrahlung spectrum of a tungsten target bombarded with electrons over a voltage range of 20–50 kV. 44

3.3 Same as Fig. 2.2 but for the atomic processes ECC and RECC.. 47

3.4 Calculated contributions of AB, RI, and SEB versus measured contribution of AB for 1 MeV H^+ + Al (left panel) and versus the measured and calculated total contribution of the three processes for the x-ray emission for 4 MeV H^+ + Al (right panel), both at 90°. 50

3.5 The number of photons due to bremsstrahlung as a function of angle for central collisions of gold in the energy range 10 keV – 3 MeV. The three curves correspond to α, β, γ, which categorize as “full stopping”, “50% stopping” and “near transparency”, respectively. 51

3.6 Bremsstrahlung spectrum for 2 MeV H^+ + C. 53

3.7 Calculated contributions of NB, AB, SEB, and the total of the three processes versus the measured total contribution of the three processes for 1.5 MeV H^+ + Al at 90°. 54

3.8 Bremsstrahlung spectrum (full circles) measured at -34° for e + C at a collision energy of 300 keV in coincidence with 160 keV outgoing electrons at 28° 55

3.9 Same as Fig. 2.2 but for the atomic process NRC to the target K-shell. 56

3.10 Predicted total cross sections of electron capture, radiatively (dashed line), nonradiatively (dotted line), and the sum of both (solid line) for U^{92+} + N_2 versus projectile energy. 58

3.11 Same as Fig. 2.2 but for the atomic process DREC to the target K-shell... 61

4.1 Schematic diagram of a Van de Graaff accelerator: (1) high-voltage terminal, (2) upper needles (discharging electrode), (3) lower needles (charging electrode), (4) upper metal roller, (5) lower metal roller, (6) moving belt, (7) ion source, (8) ion beam, (9) high-voltage supplier. 65

4.2 Schematic diagram of SNICS II ion source by cesium sputtering. 68

4.3 Schematic of the tandem Van de Graaff accelerator facility at WMU. 70

4.4 Schematic diagram of the experiment setup in the target room in a top view of random scale. 72

4.5 Detection efficiency of SLP Series Si(Li) detector versus Be window thickness in the low-energy range ($0.3-10$ keV) and versus crystal thickness in the high-energy range (>10 keV). 73

4.6 Schematic diagram of the data acquisition system, showing only one particle channel as an example. 77

4.7 $q-2$ particle spectrum delivered from TAC to ADC with 2 ns per channel and FWHM of the time peak of ~ 45 ns. 79

4.8 $q-2$ particle-gated x rays: (a) with random events not subtracted, (b) associated with random events, (c) with random events subtracted. ... 80

5.1 Expected (calculated) REC and RDEC lines for 2.21 MeV/u F^{9+} on a C foil. 82

5.2 Measurements for singles x rays (in black) for 2.21 MeV/u F^{9+} superimposed on PIXE (in red) using a 3 MeV protons, both on the same C foil. 83

5.3 Drawing showing the scattering of H^{+} at 2.7° (in blue) and F^{9+} at 1.7° (in red) ions upon hitting the aperture prior to the Al frame. 85

5.4 Photon energy-calibration curve based on the characteristic lines Al Kα, K Kα, Ca Kα, Mn Kα, and Mn Kβ. 85

5.5 X rays associated with charge change and no charge change with random backgrounds subtracted for 2.21 MeV/u F^{9+} + C collisions: (a) for F^{7+}, (b) for F^{8+}, (c) for F^{9+}. 89

5.6 X rays associated with charge change for 2.21 MeV/u F^{9+} + C collisions: (a) for F^{8+} with the spectrum of x rays associated with F^{7+} normalized and superimposed on it, (b) for F^{9+} with the spectrum of x rays associated with F^{7+} normalized and superimposed on it, (c) for K-REC spectrum as a result of summing up the leftovers from the spectra F^{8+} (61.4%), F^{9+} (33.4%), F^{7+} (5.2%) (not shown), (d) Compton profiles of the two K-shell electrons (blue), the four L-shell electrons (red), and the sum of the two profiles (black), which represents the Compton profile of the C atom. 95

5.7 Analysis trials for RDEC showing the normalized spectra of x rays associated with F^{8+} (in red) superimposed on the spectra of x rays associated with F^{7+} (in black) in the left panels. 98

5.8 Fitting to give the average between the best two trials (b, b′) and (c, c′) of Fig. 5.7 showing x rays associated with charge change for 2.21 MeV/u F^{9+} + C collisions with random backgrounds subtracted: (a) for F^{7+} with the spectrum of x rays associated with F^{8+} normalized to it at the position of the K Kα line and superimposed on it, (b) for F^{7+} with normalized x rays associated with F^{8+} subtracted. 99

CHAPTER I

INTRODUCTION

One of the most well-known mechanisms of interaction between electromagnetic radiation and matter is the photoelectric effect (PE), which was first observed by Heinrich Hertz in 1887 [1]. The effect leads to the fundamental process of photoionization (PI) [2] during which a photoelectron is emitted from the target upon the absorption of a single photon of energy that is sufficient to free a bound electron. It should be noted that PI was first investigated only for neutral atomic and molecular targets [3,4] and later for multielectron ions, theoretically [5,6,7] and experimentally [8,9]. The neutral atom as a multielectron system causes a background of electron-electron (e-e) interactions during the process of PI, which in turn, is the origin of the discrepancies between measurements and theoretical predictions.

To resolve this issue, it is better to use a system free from these e-e interactions. The purest form of photon-electron (γ-e) interaction without interference from the Coulomb field of other orbital electrons requires a one-electron system as a target for the incident photon. The principle of detailed balance (PDB) [10,11,12] has been used to introduce an indirect way to investigate PI by measuring the time-reversed process of radiative recombination (RR) [13] for fully-stripped target ions. RR is a one-step process, where the incident electron is captured to a bound state of

the target atom with a simultaneous emission of a single photon. The one-step process of radiative electron capture (REC) [14] can also be treated as the time-reversed process of PI if a loosely-bound target electron is captured. When such a situation exists and if REC is studied in the projectile frame, REC in ion-atom collisions will not only correspond to RR in electron-ion collisions but the data of RR can also be folded into the Compton profile of the target electrons to generate the corresponding data of REC [15]. If a tightly-bound target electron is captured due to REC, there may be a complication in the comparison with the theoretical predictions and REC will not be an exact time-reversed process of PI. Performing REC for fully-stripped ions [16,17,18,19] offers the cleanest method for exploration of photoionization of H-like ions, allowing for observation of the purest form of the γ-e interaction.

Another consequence of PE is double photoionization (DPI), a process that has been considerably investigated over the past three decades for neutral atoms as well as for various ions [20]. It is a mechanism in which a single photon interacts with only one target electron, causing it to be ejected, but since two electrons are ejected, this process requires that the electrons interact and DPI is caused by the e-e correlation [21]. To avoid a strong background interaction due to the Coulomb field of the other electrons that do not interact with the incident photon, DPI was investigated experimentally by means of synchrotron radiation [22,23] and VUV lamps [24], mostly for low-*Z* noble gases such as He [25,26,27,28,29,30,31], Ne [32,33,34], and Ar [32,35], and theoretically for He [36,37,38,39] and rare gases in

general [40,41]. Little work has been done to investigate DPI of other elements, theoretically such as H_2 [42], and experimentally such as Be, Mg, and Ca [43].

Similar to the analogy with PI, DPI can be predicted by the investigation of the time-reversed process of radiative double electron capture (RDEC) to bare projectile ions in collisions with atoms. Accordingly, RDEC was addressed over the last two decades theoretically [44,45,46,47,48,49,50] and experimentally [51,52,53,54,55,56,57,58,59,60,61,62]. RDEC is also a one-step process in ion-atom collisions occurring when two target electrons are captured to a bound state of the projectile simultaneously with the emission of a single photon. The emitted photon has approximately double the energy of the photon emitted due to REC. Fully-stripped ions were used as projectiles in the performed RDEC experiments, providing a recipient system free of electron-related Coulomb fields. This allows the captured target electrons to be transferred without interaction with any of the projectile electrons, enabling accurate investigation of the electron-electron interaction in the vicinity of electromagnetic field. Hence, studying RDEC by bare projectiles provides a means to obtain a proper description of the two-electron wave function in the projectile continuum of various atomic systems.

Attempts to observe RDEC at the Gesellschaft für Schwerionenforschung mbH (GSI) complex accelerator facility at Darmstadt did not confirm the observation of RDEC primarily due to the poor statistics of the data. Although the observation of RDEC could not be verified during such experiments, an upper limit of the total

RDEC cross section was deduced during each experiment. This upper limit was found to be one order and four orders of magnitude lower than the first and the second approximations of Chernovskaya [50], respectively, three orders of magnitude lower than the relativistic prediction of Yakhontov [45], and three orders of magnitude higher than Mikhailov prediction [47] in the case of the relativistic heavy-ion collision system (U^{92+} + Ar at 297 MeV/u) [52]. In the case of the mid-*Z* projectile at nonrelativistic energy (Ar^{18+} + C at 11.4 MeV/u) [51], the upper limit was in fair agreement with Yakhontov, Mikhailov, and the second approximation of Chernovskaya [50], while it was found to be two orders of magnitude lower than the first approximation of Chernovskaya [50].

Optimizing for the best experimental conditions under which RDEC can be observed, solid light targets were suggested in a theoretical study for fast heavy ions [45], while solid-state targets were proposed in another theoretical approach for slow collisions [47] where the electrons in the valence zone behave as quasifree particles with a characteristic velocity, which is much smaller than that of the projectile even for slow collisions, determined by the target temperature. Such comparisons, in addition to the recent theoretical predictions [47,48,49] suggesting projectiles of moderate *Z* for low-energy collisions, were the motivation to conduct RDEC experiments under these conditions. The observation of RDEC was verified for the first time for the collision system 2.38 MeV/u O^{8+} + C [53,54,55,56,57], and then also for the second time for the collision system 2.21 MeV/u F^{9+} + C [58,59,58,61,62],

which is the topic of this thesis. Both successful observations were conducted at the tandem Van de Graaff accelerator facility located at Western Michigan University (WMU). The theoretical approaches were the motivation to perform the preceding attempts to observe RDEC as well as the two recent successful observations. Furthermore, theory offered predictions to which our measurements can be compared, allowing for testing the consistency of such predictions with measured cross sections.

The main goal of the work within this dissertation is to investigate RDEC during the collision of fully-stripped fluorine ions at 2.21 MeV/u with a thin carbon foil and compare the results to the recent experimental [54] and theoretical studies [12,45,47,49,50]. In this work, x rays associated with projectile charge-changing by single and double electron capture and no charge change by F^{9+} ions were observed and compared with recent work for O^{8+} ions and with theory. REC, in turn, was investigated as a means to compare with the theoretical predictions of the RDEC/REC cross section ratio.

In Chapter I, the basic concepts of the atomic processes pertaining to RDEC are explored, while REC and RDEC as the atomic processes of interest are discussed extensively in Chapter II with emphasis on their history and the theoretical approaches to which our results can be compared. Chapter III discusses in detail the most important background processes that may overlap with the desired processes. This enables extraction of REC and RDEC contributions more accurately from the entire spectrum of x-ray emission or at least ensures that the background processes

have negligible contribution to the energy range of interest. The setup of the current experiment including x-ray and particle detectors as well as the data acquisition system is discussed in Chapter IV. The concept of the Van de Graaff accelerator with emphasis on the facility located at WMU and the ion source used to generate the ion beam are also discussed in the same chapter. Chapter V is dedicated to showing the obtained results and how the singles data were analyzed to generate the x rays associated with charge-changed and unchanged projectile ions. Proton-induced x-ray emission (PIXE) analysis of the target is also addressed to determine the presence of any contamination lines. A discussion is introduced in this chapter, showing how the REC and RDEC cross sections were obtained by the subtraction of the x rays due to the contamination lines and then compared to various theoretical approaches. Chapter VI gives an overall view of what was achieved from the experiment and the final conclusions based on the obtained results. Suggestions for any similar prospective projects are also introduced.

CHAPTER II

RADIATIVE SINGLE AND DOUBLE ELECTRON CAPTURE

2.1 Compton Profile

The radiative single (REC) and double electron capture (RDEC) peaks have widths defined by the Compton profile $J(p_z)$ of the target electrons, describing the momentum p_z distribution of the bound electrons within the target atom. The momentum p_z is defined as the projection of the intrinsic momentum vector of the bound electron on the collision axis *Z*, which is defined by the direction of the projectile velocity. Both p_z and $J(p_z)$ are measured in the CGS system of measurements in $m_e e^2/\hbar$ and $\hbar/m_e e^2$, respectively, for electron mass m_e, electron charge *e*, and reduced Planck constant $\hbar$. The width of $J(p_z)$ increases with the increase of the atomic number and the binding energy of the electron. Hence, the distribution becomes broader for heavier targets and for inner-shell electrons rather than lighter atoms and outer-shell electrons, respectively.

Compton profiles of the individual bound electrons within the carbon atom in the amorphous state are drawn in Fig. 2.1 by means of the data given by Biggs [63]. The drawing shows that $J(p_z)$ is broader in width for the 1s electron than for L-shell

electrons. For an electron with principal and orbital quantum numbers n and l, respectively, the Compton profile can be expressed by

$$J_{nl}(p_z) = \frac{1}{2}\int_{p_z}^{\infty} \left|\chi_{nl}(p)\right|^2 p dp\,, \tag{2.1}$$

where $\chi_{nl}(p)$ is the Fourier transform of the spatial wave functions $R_{nl}(r)$. The integrated profile must fulfill the condition

$$2\int_{0}^{\infty} J_{nl}(p_z) dp_z = 1. \tag{2.2}$$

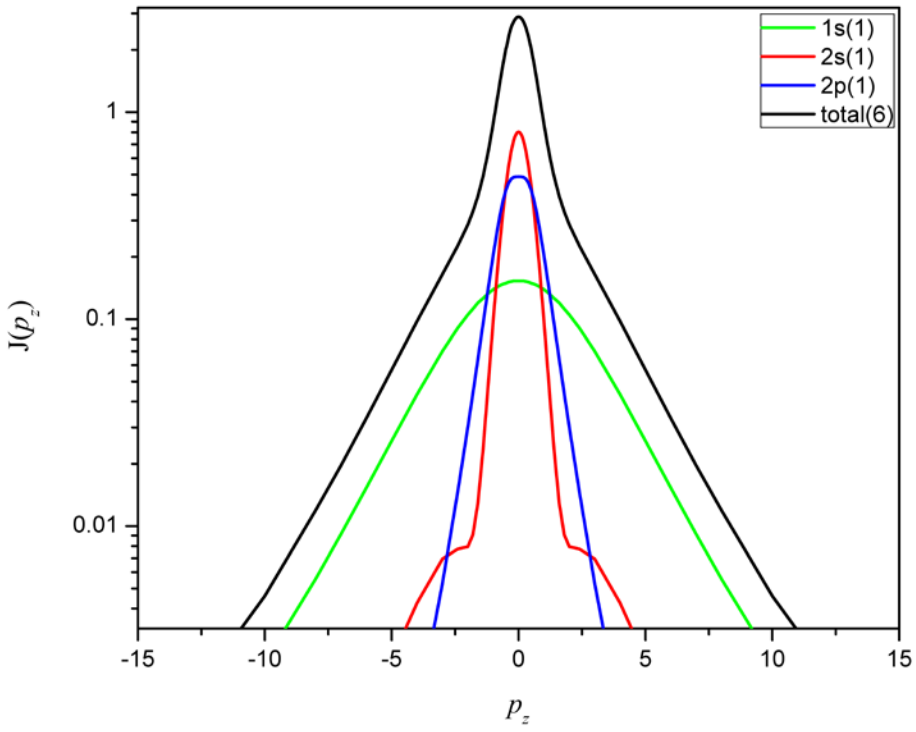

FIG. 2.1. Compton profile of the carbon atom in the amorphous state as calculated from Ref. [63]. Compton profiles of the 6 electrons are added up and represented by the black line, i.e., twice as the sum of the red, blue, and green profiles.

REC in ion-atom collisions is analogous to RR in electron-ion collisions if the requirements of the impulse approximation are verified and if REC is studied in the projectile frame, so that *ab initio* calculations of RR can be folded into the Compton profile of the target electrons to generate the corresponding data for REC [15].

2.2 Radiative Electron Capture (REC)

2.2.1 Kinematics of REC

One of the most significant and dominant mechanisms of continuous x-ray production and well-known processes during heavy-ion collisions with atoms is radiative electron capture (REC). Before it was observed forty years ago [14,64,65], it was theoretically studied by Stobbe [66] and Bethe and Salpeter [67]. Most of the attention at this time was devoted to very low projectile velocities [68] since its contribution was estimated to be small at high velocities. Following the first observation of REC, it was investigated more through many theoretical [69,70,71,72] and experimental [73,74,75,76,77,78,79] studies with the emphasis on fully-stripped projectile ions [16,17,18,19].

As indicated in Fig. 2.2, REC is a one-step process, where a target electron is captured to a projectile bound state with simultaneous emission of a single photon of energy $\hbar\omega_{REC}$. The photon energy is given [64] in nonrelativistic collisions under the requirements of the principle of conservation of energy by

$$\hbar\omega_{REC} + B_p = B_t + \frac{1}{2m_e}\left(\vec{p}_{et} + \vec{p}_e\right)^2, \tag{2.3}$$

$$\frac{1}{2m_e}\left(\vec{p}_{et} + \vec{p}_e\right)^2 = K_{et} + \vec{\upsilon}_p.\vec{p}_{et} + K_e, \tag{2.4}$$

where K_{et} (usually neglected especially for relativistic collisions) and K_e are the kinetic energy of the bound target electron and the kinetic energy of the captured target electron as calculated in the rest frame of the projectile, respectively. The binding energies B_t and B_p are negative values by convention, denoting the binding energies of the target electron before and after being captured, respectively. The vectors $\vec{p}_{et}$, $\vec{p}_e$, and $\vec{\upsilon}_p$ designate the momentum of the bound target electron before being captured, momentum of the captured target electron while it is moving towards the projectile in the rest frame of projectile, and the projectile velocity, which is the same as the velocity of the captured target electron in the rest frame of projectile, respectively. Eqs. (2.3) and (2.4) then simplify to

$$\hbar\omega_{REC} = K_e + K_{et} - B_p + B_t + \vec{\upsilon}_p.\vec{p}_{et}\,. \tag{2.5}$$

The peak dedicated to REC has a width and structure similar to the Compton profile of the captured target electron. Hence, it is necessary to introduce the REC photon energy defined in terms of the Compton profile variable p_z, which is given in terms of the angle φ between $\vec{\upsilon}_p$ and $\vec{p}_{et}$ by

$$p_z = \frac{\vec{\upsilon}_p.\vec{p}_{et}}{\upsilon_p} = p_{et}\cos\varphi\,. \tag{2.6}$$

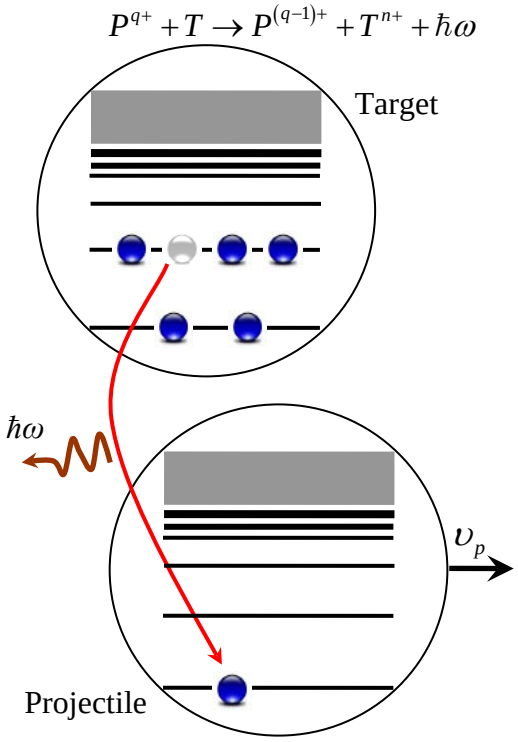

FIG. 2.2. Schematic diagram for the atomic process REC into a fully-stripped ion showing electron capture and photon emission by a passing ion.

Accordingly, Eqs. (2.5) and (2.6) allow for converting the momentum of a bound target electron into the energy of the photon emitted due to the capture of this electron into a projectile bound state and vice versa according to

$$\hbar\omega_{REC} = K_e + K_{et} - B_p + B_t + \upsilon_p p_z , \tag{2.7}$$

which can be rewritten for relativistic collisions as [80,81]

$$\hbar\omega_{REC} = m_e c^2 (\gamma - 1) - B_p + B_t + \gamma\upsilon_p p_z , \tag{2.8}$$

where K_{et} is neglected for relativistic collisions, while c and γ are the speed of light and the Lorentz factor, respectively, where $\gamma = 1/\sqrt{1-\beta^2}$ with $\beta = \upsilon_p / c$.

The centroid energy of REC into the projectile K-shell (K-REC) is given [81] in the laboratory frame by

$$\hbar\bar{\omega}_{REC} = \frac{(\gamma - 1) m_e c^2 - B_p}{\gamma(1 - \beta \cos\theta)}. \tag{2.9}$$

For Eq. (2.7), the kinetic energy of the captured electron K_e can be calculated by

$$K_e = E_p \left(m_e / m_p \right), \tag{2.10}$$

while for nonrelativistic hydrogenic atoms, i.e., H-like projectile ions, the binding energy B_n for an electron with principal quantum number *n* is given by

$$B_n = 13.6 \left(\frac{Z^2}{n^2} \right), \tag{2.11}$$

where Z is the charge of the nucleus, i.e., the atomic number, for projectile (Z_p) or target (Z_t) in the case of B_p or B_t, respectively. For multielectron ions, Z is replaced by the nucleus effective charge Z_{eff} seen by the bound target electron before being captured for B_t and after being captured for B_p. There are several approaches to calculate Z_{eff} [82,83], and for precise values, atomic codes such as Hartree-Fock (HF) can be used.

2.2.2 REC Cross Section

The comparison between the four panels of Fig. 2.3 [84] not only tells us that the REC peaks shift to lower energies as the projectile energy decreases but also it shows that such peaks are apparently broader in width than the peaks dedicated to the

characteristic x rays. In principal, the energies of the characteristic x rays, unlike the REC photon energies, should be independent of projectile energy. However, a shift of the characteristic x rays of energy $\hbar\omega_\circ$ towards lower energies with the increase of the projectile energy is observed in Fig. 2.3 and can be attributed to the Doppler (red) shift, causing the emitted photon to be observed at an energy given by

$$\hbar\omega_{red-shift} = \hbar\omega_\circ\left[\gamma\left(1-\beta\right)\right]. \tag{2.12}$$

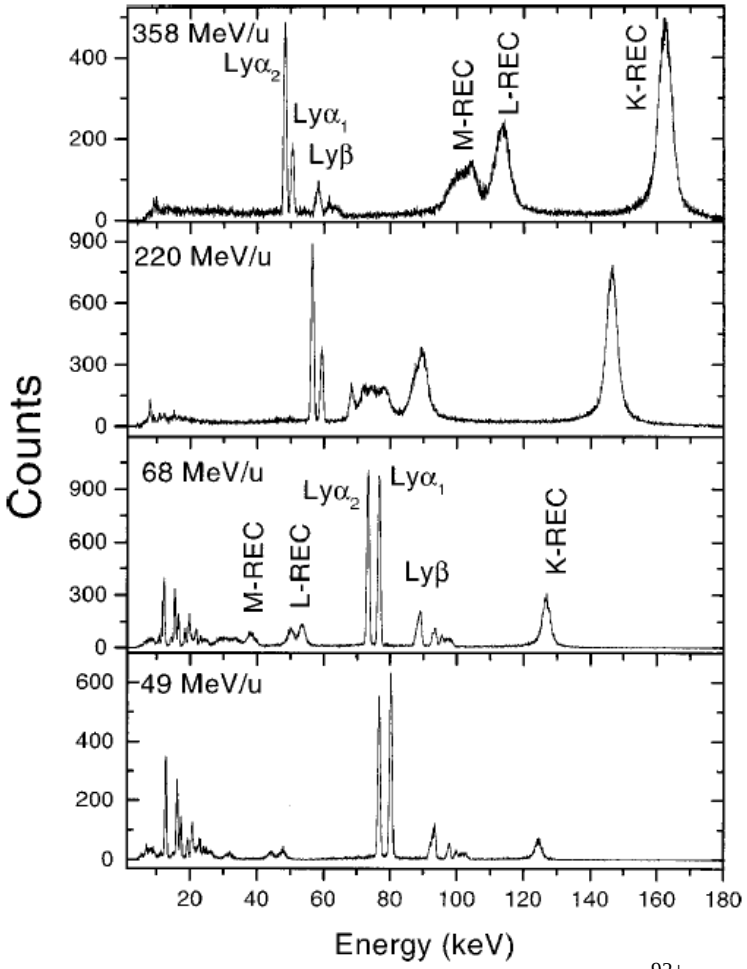

FIG. 2.3. X rays in coincidence measurements at 132° for U^{92+} + N_2 at collision energies 49, 68, 220, and 358 MeV. Spectra are not corrected for detection efficiency (from Ref. [84]).

One of the most reliable theoretical predictions of the total K-REC cross section σ_{REC}^{1s} is the formula derived by Stobbe [66] and estimated later by Bethe and Salpeter [67]. The Bethe-Salpeter formula was derived for a bare nucleus and σ_{REC}^{1s} is given per target electron within the non-relativistic dipole approximation by

$$\sigma_{REC}^{BS} = \left(9.16\times10^{-21}\right)\left(\frac{\kappa^3}{1+\kappa^2}\right)^2 \frac{\exp\left(-4\kappa\tan^{-1}\left(1/\kappa\right)\right)}{1-\exp\left(-2\pi\kappa\right)}\,\mathrm{cm}^2/\mathrm{atom}\,, \qquad (2.13)$$

where κ is the Sommerfeld parameter and is defined [49] in terms of the average momentum p_{ep} of the target electron after being captured to the projectile K-shell and the momentum p_e of captured target electron in the rest frame of projectile by

$$\kappa = \frac{p_{ep}}{p_e}. \qquad (2.14)$$

The Sommerfeld, sometimes called Coulomb, parameter measures how strongly the asymptotic wave function of the electron during the collision will be distorted by the Coulomb interaction, where strong distortion is for the collision systems with $\kappa > 1$. The momenta p_{ep} and p_e are defined by

$$p_{ep} = m_e\upsilon_{ep} = m_e c\alpha Z_p = \frac{m_e e^2 Z_p}{\hbar}\,, \qquad p_e = m_e\upsilon_p\,, \qquad (2.15)$$

where α and αZ_p are the fine structure constant given in the CGS system by $e^2/\hbar c$ and the Coulomb parameter, respectively, while υ_{ep} is the average velocity of the target electron after it transfers to the projectile K-shell. Consequently, the Sommerfeld parameter κ can be written as

$$\kappa = \frac{p_{ep}}{p_e} = \frac{\upsilon_{ep}}{\upsilon_p} = \frac{\alpha Z_p}{\beta} = \frac{Z_p e^2}{\hbar \upsilon_p}. \tag{2.16}$$

The adiabacity parameter η, as a value to judge how fast ($\eta > 1$) or slow ($\eta < 1$) the collision is, can be defined in terms of κ [18,79,85] by

$$\eta = \kappa^{-2} = \frac{K_e}{K_{ep}} = \left(\frac{\upsilon_p}{\upsilon_{ep}}\right)^2 = \left(\frac{\beta}{\alpha Z_p}\right)^2 \simeq (40.31)\frac{K_e(\mathrm{MeV})}{Z_p^2}. \tag{2.17}$$

For fast nonrelativistic collisions, the total REC cross section scales as [85,86]

$$\sigma_{REC} \propto \frac{Z_p^5 Z_t}{\upsilon_p^5}. \tag{2.18}$$

REC in ion-atom collisions corresponds to RR in electron-ion collisions if a loosely-bound target electron is captured under the validity of the impulse approximation conditions. Accordingly, both processes are considered as the time-reversed process of PI. Owing to the principle of detailed balance [10,11,12], σ_{REC} can be calculated from the corresponding photoionization cross section σ_{PI} [15,51,66] as given by

$$\sigma_{REC}(\beta) = Z_t \left(\frac{\hbar\omega}{\gamma\beta m_e c^2}\right)^2 \sigma_{PI}(\hbar\omega). \tag{2.19}$$

Measuring REC by fully-stripped projectile ions offers the cleanest method for exploration of photoionization of H-like ions. This allows for observation of the γ-e interaction in its purest form. If the photon dedicated to REC is emitted due to the

capture of an inner-shell target electron, Eq. (2.19) becomes inaccurate for conversion between the two processes.

2.2.3 Angular Distribution of REC Photon Emission

The angular distribution of K-REC as described by its differential cross section (DCS) within the dipole approximation in nonrelativistic collisions was given by Kleber in 1975 [71,80] and confirmed by Schule [87] in 1977 with a more general expression that is valid for relativistic and nonrelativistic collisions as given by

$$\frac{d\sigma_{REC}^{1s}}{d\Omega} = \sigma_{REC}^{\exp}\left(\frac{3}{8\pi}\right)\sin^2\theta\left(1-\beta\cos\theta\right)^{-4}. \tag{2.20}$$

The corresponding predicted differential K-REC cross section is given by

$$\frac{d\sigma_{REC}^{1s}}{d\Omega} = N_t\sigma_{REC}^{B-S}\left(\frac{3}{8\pi}\right)\sin^2\theta\left(1-\beta\cos\theta\right)^{-4}, \tag{2.21}$$

where the approximation $\left(1-\beta\cos\theta\right)^{-4} \simeq 1+4\beta\cos\theta$ can be used. The symbol N_t denotes the number target electrons, while θ is the x-ray observation angle with respect to the beam direction.

Angular distribution of x-ray emission due to K-REC is shown in Fig. 2.4 for S ions in collisions with C (left panel) and Ni (right panel) at 20, 30, and 115 MeV. The spectra show that the trend of $\sin^2\theta$ is well-verified over the tested range of x-ray observation angles.

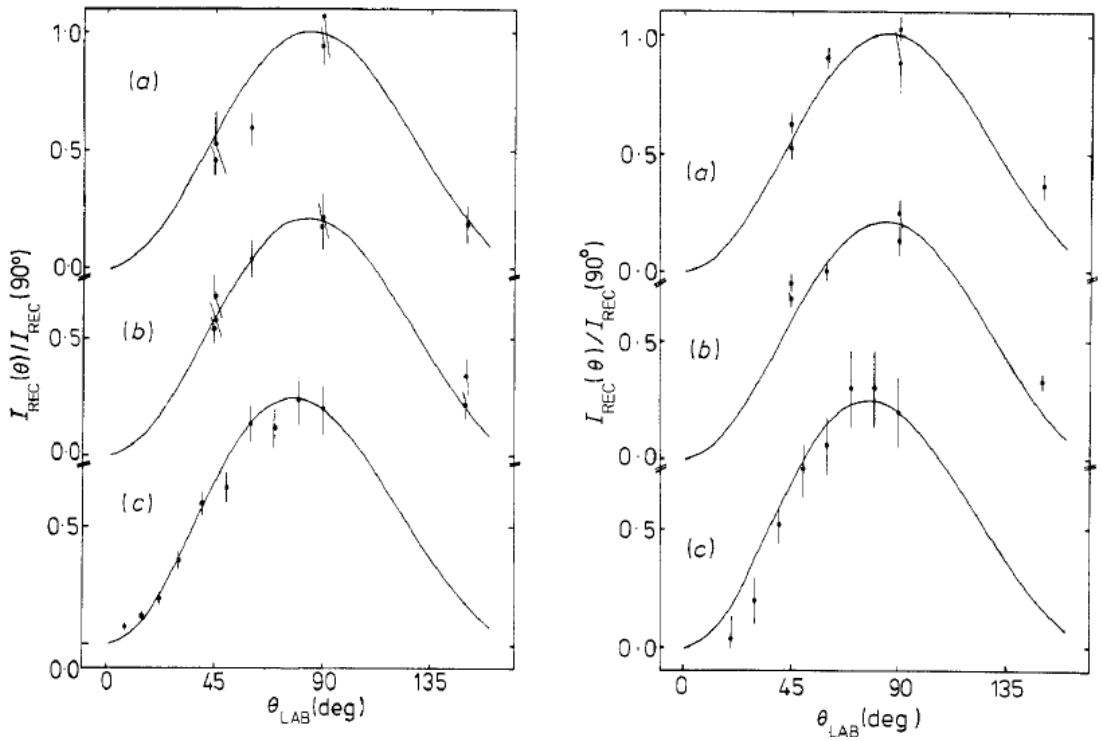

FIG. 2.4. Angular distribution of x rays due to REC for S ions in collisions with C (left panel) and Ni (right panel) targets at (a) 20, (b) 30, and (c) 115 MeV (from Ref. [87]).

The angular distributions of the photon emission in the form of the angle-differential REC cross section for capture into K, L, and M shells were predicted by Eichler [88] for Z_p = 50, 70, and 90 at collision energies 20, 100, and 300 MeV/u in nonrelativistic collisions as shown in Fig. 2.5 for Z_p = 50. The approximate behavior of the differential REC cross section for the capture into the orbit 2p was given by

$$\frac{d\sigma_{REC}^{2p}}{d\Omega} \propto \sin^2\theta\cos^2\theta \propto \sin^2 2\theta\,. \qquad (2.22)$$

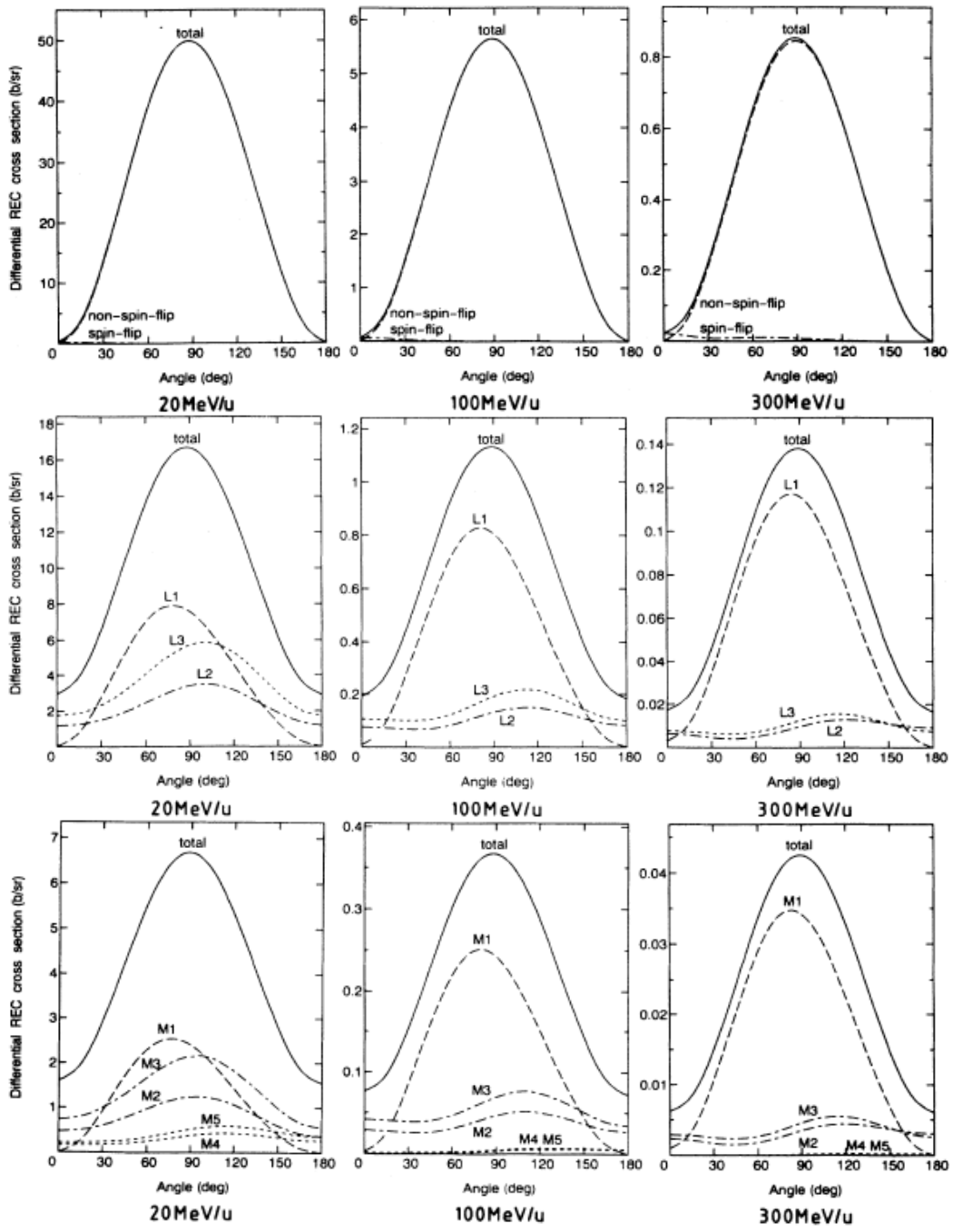

FIG. 2.5. Calculated angular distributions of x rays due to K-REC (upper panel), L-REC (middle panel) and M-REC (lower panel) for tin ions at collision energies of 20, 100, and 300 MeV/u. The contributions of REC into all subshells are also presented (from Ref. [88]).

To transform between differential REC cross sections at different observation angles [79,89], for instance, between the projectile (primed) and the laboratory (unprimed) systems, one can use Eq. (2.23) in light of the set of Eqs. (2.24).

$$\frac{d\sigma_{REC}(\theta)}{d\Omega} = \frac{d\sigma_{REC}(\theta')}{d\Omega'}\frac{d\Omega'}{d\Omega}, \tag{2.23}$$

$$\frac{d\Omega'}{d\Omega} = \frac{1}{\gamma^2(1-\beta\cos\theta)^2}, \qquad \cos\theta' = \frac{\cos\theta-\beta}{1-\beta\cos\theta}, \quad \sin\theta' = \frac{\sin\theta}{\gamma(1-\beta\cos\theta)}. \tag{2.24}$$

The double differential and total K-REC cross sections are related by [81]

$$\sigma_{REC}^{1s} = \frac{2}{3}\int d(\hbar\omega)\frac{d^2\sigma_{REC}^{1s}(\theta=90^\circ,\hbar\omega)}{d(\hbar\omega)d\Omega}, \tag{2.25}$$

while the double and single differential K-REC cross sections are related through Compton profile $J(p_z)$ as given by [81]

$$\frac{d^2\sigma_{REC}^{1s}(\theta,\hbar\omega)}{d(\hbar\omega)d\Omega} = \frac{1}{\hbar\gamma\beta c}\left(\frac{d\sigma_{REC}^{1s}}{d\Omega}\right)J(p_z). \tag{2.26}$$

2.3 Radiative Double Electron Capture (RDEC)

2.3.1 Kinematics of RDEC

As indicated in Fig. 2.6, RDEC is a one-step process where two electrons are captured from one target atom to a projectile bound state during a single collision with simultaneous emission of a single photon of about double the energy of REC. The RDEC photon energy is then given by

$$\hbar\omega_{RDEC} = 2K_e + 2K_{et} - B_p^{(1)} - B_p^{(2)} + B_t^{(1)} + B_t^{(2)} + \left(\vec{\upsilon}_p.\vec{p}_{et}\right)^{(1)} + \left(\vec{\upsilon}_p.\vec{p}_{et}\right)^{(2)}, \tag{2.27}$$

where K_{et} and K_e are defined in the rest frame of the projectile as the kinetic energies of the bound and captured target electrons, respectively, while B_t and B_p are negative values by convention denoting the binding energies of the target electron before and after being captured, respectively. The vectors $\vec{\upsilon}_p$ and $\vec{p}_{et}$ designate the projectile velocity and the momentum of the bound target electron before being captured, respectively, while the indices (1) and (2) denote the first and the second captured target electrons.

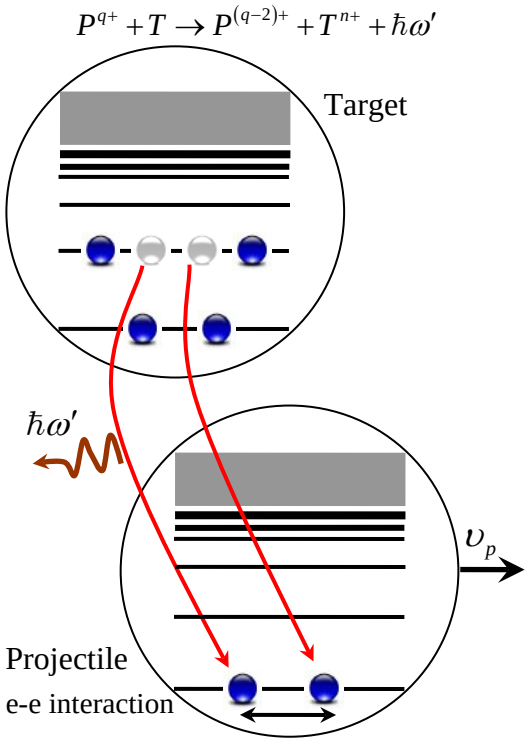

FIG. 2.6. Same as Fig. 2.2 but for the atomic process RDEC. Here the capture of two electrons is shown accompanied by the emission of a single photon of about twice the energy of REC.

If the target electrons are captured through the same channels, i.e., two identical target electrons are captured to the same orbit, or in other words they transfer from identical orbits to identical orbits, Eq. (2.27) simplifies to

$$\hbar\omega_{RDEC} \simeq 2\hbar\omega_{REC} = 2\left(K_e + K_{et} - B_p + B_t + \vec{\upsilon}_p.\vec{p}_{et}\right). \qquad (2.28)$$

Similar to REC, each RDEC peak has a width and structure defined by the sum of Compton profiles of the two captured electrons. Referring to Eq. (2.6), Eq. (2.27) can be rewritten in terms of the Compton variable p_z as

$$\hbar\omega_{RDEC} = 2K_e + 2K_{et} - B_p^{(1)} - B_p^{(2)} + B_t^{(1)} + B_t^{(2)} + \left(\upsilon_p p_z\right)^{(1)} + \left(\upsilon_p p_z\right)^{(2)}. \qquad (2.29)$$

The two captured electrons are correlated due to the mutual Coulomb interaction between them, while the emitted photon satisfies the law of conservation of energy between the initial and final states of the collision partners. The target electrons can be captured from the same orbit or from two different orbits to the projectile K-shell (KK-RDEC) or to both K- and L-shells (KL-RDEC). The RDEC photon with the lowest energy is emitted when two K-shell electrons are captured from the target atom to the projectile metastable state $1s^1 2s^1$, while the photon of highest energy is released if two valence target electrons (L-shell) are captured to the projectile ground state $1s^2$. Although the angular distribution of RDEC photon emission has not been reported yet in the literature, it was assumed in this dissertation that RDEC photons are emitted with the same angular distribution as REC.

2.3.2 The First Experiment Dedicated to RDEC: Testing the Principle of Detailed Balance

Measurements looking for RDEC started in 1994 with an experiment conducted at the GSI accelerator complex facility at Darmstadt as the first attempt to observe the process for the collision system 11.4 MeV/u Ar^{18+} + C [51]. A stainless-steel attenuator for which the attenuation was 0.999% was used to suppress possible pileup events (see Section 3.4 below) from REC photons. The observation of RDEC could not be verified as shown in Fig. 2.7 due to the poor statistics of the collected data. However, the few counts collected in the RDEC energy range allowed an upper limit of 5.2 mb/atom to be deduced for the total RDEC cross section σ_{RDEC}.

Owing to the principle of detailed balance and similar to REC, σ_{RDEC} can be found from the corresponding double photoionization cross section σ_{DPI} as given by

$$\sigma_{RDEC}(\beta) = AZ_t(Z_t - 1)\left(\frac{\hbar\omega'}{2\gamma\beta m_e c^2}\right)^2 \sigma_{DPI}(\hbar\omega'), \qquad (2.30)$$

where the value $A \le 1$ describes the phase space fraction accessible to RDEC. According to Warczak [51], Eqs. (2.19) and (2.30) can be utilized to find the ratio R for the capture into the projectile K-shell by

$$R = \frac{\sigma_{RDEC}^{1s^2}}{\sigma_{REC}^{1s}} = A(Z_t - 1)\left(\frac{\hbar\omega'}{2\hbar\omega}\right)^2 \frac{\sigma_{DPI}(\hbar\omega')}{\sigma_{PI}(\hbar\omega)}. \qquad (2.31)$$

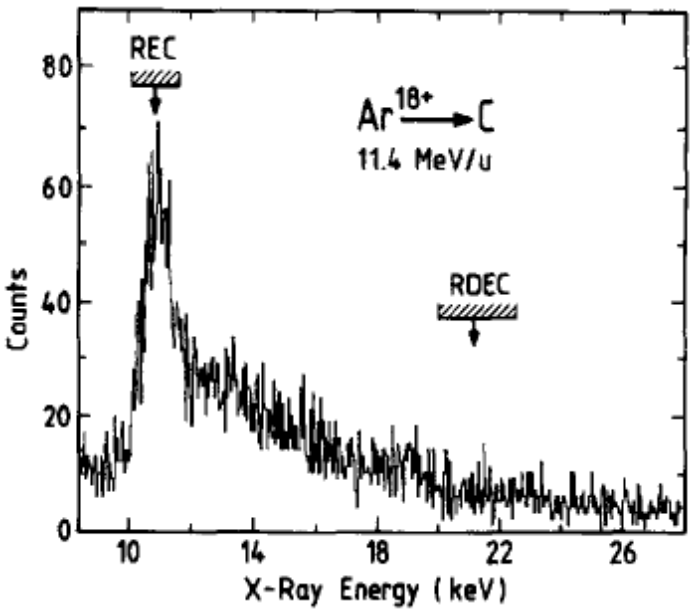

FIG. 2.7. X rays emitted for Ar^{18+} + C collisions at 11.4 MeV/u (from Ref. [51]).

The experimental value of *R* corresponding to the provided upper limit of σ_{RDEC} (5.2 mb/atom) was found to be 3.1×10^{-6}. This value was a factor of 10 less than the theoretical curves given for $A=1$ based on the double photoionization [90] and 100 times lower than a prediction given by Miraglia and Gravielle [91].

For an RDEC photon of energy $\hbar\omega' = 2\hbar\omega$, *R* can be rewritten as

$$R = \frac{\sigma_{RDEC}^{1s^2}}{\sigma_{REC}^{1s}} = A\left(Z_t - 1\right)\left[\frac{\sigma_{PI}\left(2\hbar\omega\right)}{\sigma_{PI}\left(\hbar\omega\right)}\right]\left[\frac{\sigma_{DPI}\left(2\hbar\omega\right)}{\sigma_{PI}\left(2\hbar\omega\right)}\right], \qquad (2.32)$$

where the ratio $\sigma_{DPI}\left(2\hbar\omega\right)/\sigma_{PI}\left(2\hbar\omega\right)$ was found to tend to a constant value [90] as the energy of the incident photon increases above the threshold. This is given by

$$\frac{\sigma_{DPI}\left(2\hbar\omega\right)}{\sigma_{PI}\left(2\hbar\omega\right)} = \frac{0.0932}{Z_p^2}, \qquad (2.33)$$

while the ratio $\sigma_{PI}(2\hbar\omega)/\sigma_{PI}(\hbar\omega)$ can be obtained from tabulated cross section values for the high-energy limit [92] where the photon energy exceeds the threshold of the double photoionization. This implies

$$\sigma_{RDEC}^{1s^2} = A(Z_t - 1)\left(\frac{0.0932}{Z_p^2}\right)\left[\frac{\sigma_{PI}(2\hbar\omega)}{\sigma_{PI}(\hbar\omega)}\right]\sigma_{REC}^{1s}. \tag{2.34}$$

The principle of detailed balance can be simplified in the light of the photon energy dependence of single photoionization (PI) given in the literature [90,92] by

$$\sigma_{PI}(\hbar\omega) \propto \left(\frac{1}{\hbar\omega}\right)^5. \tag{2.35}$$

This yields a factor of 1/32 for the PI ratio, allowing Eq. (2.34) to be rewritten as

$$R = \left(\frac{\sigma_{RDEC}^{1s^2}}{\sigma_{REC}^{1s}}\right) = A(Z_t - 1)\left(\frac{0.003}{Z_p^2}\right). \tag{2.36}$$

2.3.3 Yakhontov Predictions of RDEC/REC Ratio: Nonrelativistic Approach versus Relativistic Enhancement Prediction

The discrepancy found in the results obtained from the Ar^{18+} experiment [51] with the available theoretical estimations [90,91] was the motivation for Yakhontov [44,45] to perform nonrelativistic calculations modeled particularly to accommodate the requirements of the collision system (Ar^{18+} + C collisions at 11.4 MeV/u). The calculated upper limit of *R* was estimated to be 3.6×10^{-6}, which is in good agreement with the value 3.1×10^{-6} obtained by Warczak [51]. The corresponding $\sigma_{RDEC}^{1s^2}$ was obtained by summing up over the two possible polarizations of the photon and

integrating over the direction of photon emission. It was found to be 1.85 mb/atom, which is in fair agreement with the upper limit of 5.2 mb/atom obtained by Warczak [51]. Moreover, a scaling law is derived within Ref. [45], showing that

$$R \propto Z_p^{-5}, \tag{2.37}$$

which can be utilized in finding R for a nonrelativistic collision system in terms of another R of a different nonrelativistic system, provided that both systems have the same or very close Sommerfeld parameters. A reference value can be taken as $R^{\mathrm{AR}} = 3.6 \times 10^{-6}$.

Although the nonrelativistic calculations were of main interest in the Yakhontov approach [45], a relativistic treatment was also introduced, assuming a strong enhancement of $\sigma_{RDEC}^{1s^2}$ compared to the nonrelativistic estimation by a factor F defined in detail within Ref. [45]. The factor $F = \sigma_2/\sigma_1$ was evaluated as 1 and 7 for Ar and U, respectively. For R enhancement, the factor F turns into $F^8 = R_2/R_1$.

2.3.4 The Second Attempt to Observe RDEC: Testing the Yakhontov Approach

This scaling rule derived by Yakhontov [45] was tested during the second attempt to observe RDEC [52] at the ESR storage ring of GSI for the collision system (U^{92+} + Ar at 297 MeV/u). The observation of RDEC during this experiment [52] was not verified again due to the very poor statistics within the RDEC energy domain as indicated in Fig. 2.8.

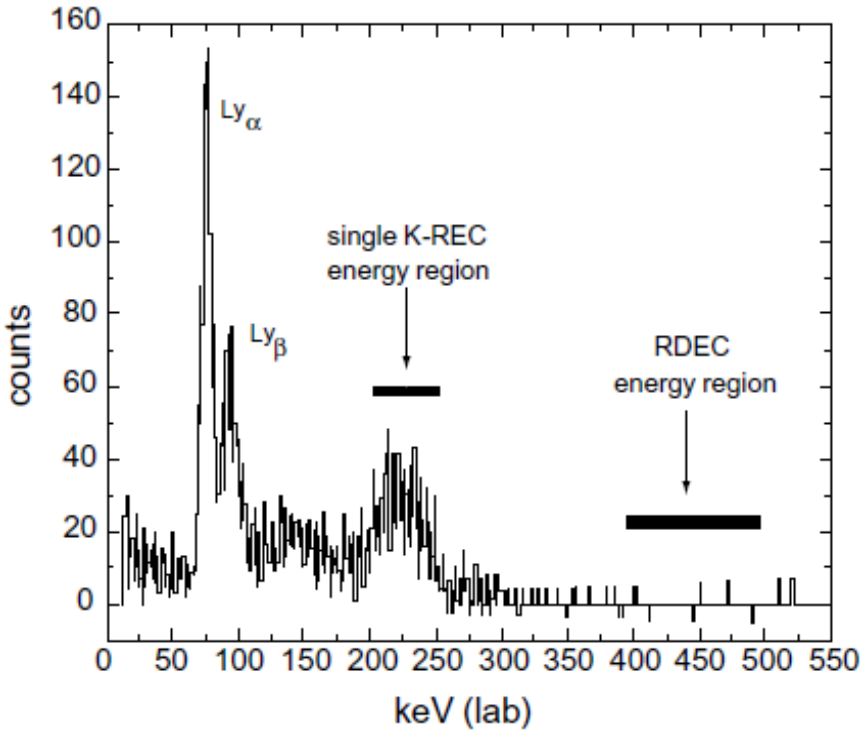

FIG. 2.8. Spectrum of x rays associated with double capture (U^{90+}) emitted due to the collision of U^{92+} with Ar at 297 MeV/u (from Ref. [52]).

Again, an upper limit of σ_{RDEC} was obtained and found to be 10 mb/atom based on the very few counts collected within the RDEC energy domain. This upper limit of 10 mb/atom was found to be 5×10^2 times lower and 1×10^4 times higher [52] than the Yakhontov relativistic and nonrelativistic predictions, respectively [45], giving a certain discrepancy between the experiment and theory as well as between the relativistic and nonrelativistic approaches of Yakhontov by six orders of magnitude. Other works that did not confirm the observation of RDEC were performed for 10 MeV/u Ar^{18+} + C at Texas A&M in 2001 [93] and 30 MeV/u Cr^{24+} + He and N_2 at GSI in 2011 [94].

2.3.5 Mikhailov Nonrelativistic Approach versus Modulated Relativistic Enhancement Prediction for RDEC into the Projectile K-shell

The huge discrepancy between the results obtained from the U^{92+} + Ar experiment [52] and the predictions introduced by Yakhontov [45] stimulated Mikhailov [47] and Nefiodov [49] to perform new nonrelativistic calculations of RDEC to explain the origin of the disagreement between theory and experiment in the case of heavy-ion collisions. A detailed treatment of both predictions is given below in terms of the universal functions $Q(\kappa)$, $H(\kappa)$, and $F(\kappa)$ as derived quantities from numerical integration within the dipole approximation and taking into account the leading orders of perturbation theory. The functions are given in terms of the Sommerfeld parameter κ, which is utilized to conclude how fast ($\kappa \gg 1$) or slow ($\kappa \ll 1$) the collision is, while for the near-threshold domain ($\kappa \simeq 1$), the K-shell-$\sigma_{DPI}(\hbar\omega')$ reaches its maximum.

According to the Mikhailov approach [47], RDEC of tightly-bound as well as valence electrons into the ground state $1s^2$ of bare projectile ions within the nonrelativistic domain of collision energy is the topic of question. The leading orders of $1/Z_p$ and αZ_p expansions were considered. If two tightly-bound target electrons are captured to the K-shell of light projectiles, then the total RDEC cross section can be written as

$$\sigma_{RDEC}^{1s^2} = \frac{2^{19}}{3}\frac{\sigma_\circ Z_t^3}{\nu Z_p^5} Q(\kappa), \tag{2.38}$$

where $\sigma_\circ = \alpha^3 a_\circ^2$ is a constant given in terms of the fine structure α and the Bohr radius $a_\circ$. The ratio $\nu = V/V_\circ$ is a dimensionless volume defined in terms of the effective localization volume V of the two captured electrons within the target atom and calibrated in units of $V_\circ = \left(a_\circ/Z_t\right)^3$. If two K-shell target electrons are captured, then V is given by $V = \pi\left(a_\circ/Z_t\right)^3$ and hence, $\nu = \pi$. If at least one of the two electrons is captured from other target bound states, i.e., other than the K-shell, then V is denoted by V_n and given by $V_n = \pi\left(a_\circ n/Z_{eff}\right)^3$. This implies that ν is denoted by ν_n and defined as $\nu_n = V_n/V_\circ = \pi\left(nZ_t/Z_{eff}\right)^3$, where n is the principal quantum number from which the outer target electron is captured and Z_{eff} is the effective charge of the target nucleus as seen by the target orbital electron before being captured to the projectile. The effective charge is given by $Z_{eff} = Z_t - \delta_n$, where δ_n is the screening correction defined by the average fractional number of target electrons between the nucleus and the electron to be captured. For a carbon atom as a target, the two singlet pairs $(1s)^2$ and $(2s)^2$ and the triplet pair $(2p)^2$ have $\delta_n^{1s} = 0.3$ and $\delta_n^{2s} = \delta_n^{2p} = 2.75$, respectively [82]. It is expected that much higher values of $\sigma_{RDEC}^{1s^2}$ can be obtained during slow collisions of multicharged ions with solid targets. The universal function $Q(\kappa)$ for a collision of Sommerfeld parameter κ can be obtained from the left panel of Fig. 2.9.

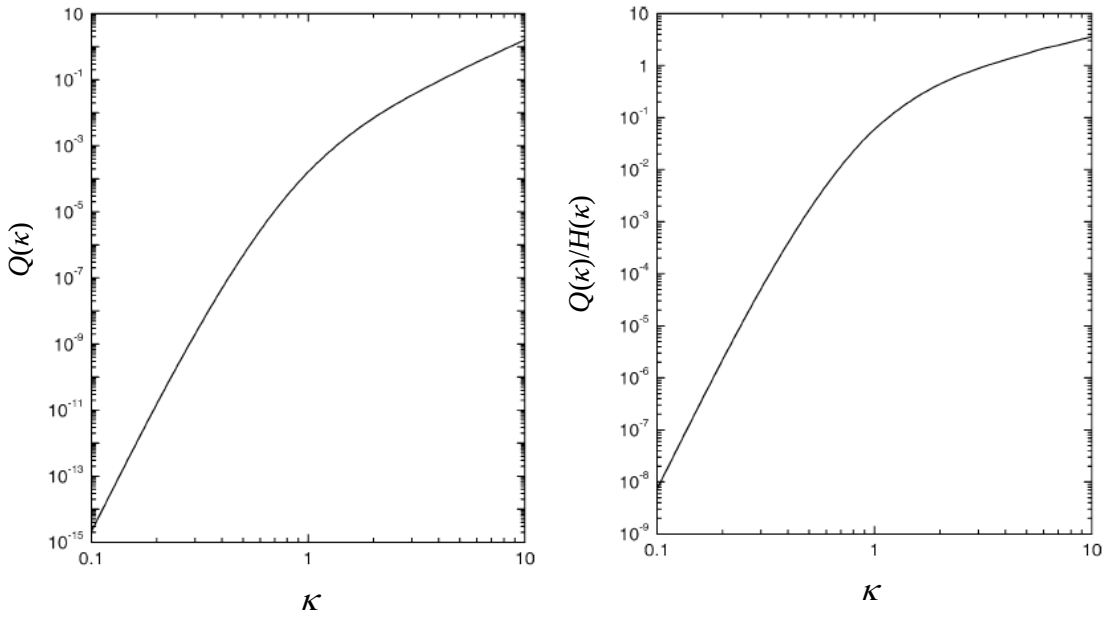

FIG. 2.9. The universal quantities of $Q(\kappa)$ (left panel) and $Q(\kappa)/H(\kappa)$ (right panel) as functions of Sommerfeld parameter κ (adapted from Ref. [47]).

The K-REC to a bare ion has a total cross section given according to Akhiezer [95] and Bethe-Salpeter [67] by

$$\sigma_{REC}^{1s} = \frac{2^{10}}{3}\pi^2\sigma_\circ Z_t H(\kappa), \tag{2.39}$$

$$H(\kappa) = \left(\frac{\kappa}{\varepsilon_\delta}\right)^2 \frac{\exp\left(-4\kappa\tan^{-1}(1/\kappa)\right)}{1-\exp(-2\pi\kappa)}, \tag{2.40}$$

where $\varepsilon_\delta = 2\left(1+\kappa^{-2}\right)$ is given as the dimensionless photon energy. The ratio R according to Eqs. (2.38) and (2.39) can then be written as

$$R = \frac{\sigma_{RDEC}^{1s^2}}{\sigma_{REC}^{1s}} = \frac{2^9}{\pi^2}\frac{Z_t^2}{\nu Z_p^5}\frac{Q(\kappa)}{H(\kappa)}, \tag{2.41}$$

where the universal ratio $Q(\kappa)/H(\kappa)$ corresponding to a specific Sommerfeld parameter κ can be estimated from the right panel of Fig. 2.9.

If two valence target electrons are captured into the projectile ground state $1s^2$, then the total RDEC cross section is given by

$$\sigma_{RDEC}^{1s^2} = \frac{2^{19}}{3}\frac{\sigma_\circ\left(n_e a_\circ^3\right)}{Z_p^5}Q(\kappa) = \frac{2^{19}}{3}\frac{n_e \alpha^3 a_\circ^5}{Z_p^5}Q(\kappa), \tag{2.42}$$

where $n_e = \left(N_V \rho_t N_A\right)/M_t$ is the target electron density in cm^{-3} given in terms of the number of valence target electrons N_V, Avogadro's number N_A, volume density ρ_t, and molar mass M_t of the target. For amorphous carbon, which is the target used for this work, $N_V = 4$, $\rho_t = 1.95$ g/cm^3, and $M_t = 12$ g/mol, giving $n_e = 3.91\times10^{23}$ cm^{-3}.

Mikhailov estimated the same factor of enhancement suggested by Yakhontov differently into a simpler form given by

$$F' = \alpha^{-\left(\alpha Z_p/\sqrt{2}\right)^2}. \tag{2.43}$$

The modulated factor of enhancement $F' = \sigma_2/\sigma_1$ was evaluated to be 1 and 3 for Ar and U, respectively. Similar to the R enhancement in the Yakhontov prediction, this approach gives an enhancement of R by $F'^8 = R_2/R_1$. This implies an agreement with the enhanced R value between the two relativistic approaches given by Yakhontov [45] and Mikhailov [47] in the case of the Ar^{18+} experiment, while a discrepancy of three orders of magnitude was found in case of the U^{92+} experiment.

2.3.6 Nefiodov Nonrelativistic Approach for RDEC into the Projectile Metastable State $1s^1 2s^1$

This approach is limited to the capture of tightly-bound target electrons into the projectile metastable state $1s^1 2s^1$ within the nonrelativistic domain of collision energies. As seen from Fig. 2.10, it is predicted that the cross section of RDEC into the excited state $1s^1 2s^1$ is enhanced drastically for slow collisions ($\kappa \gg 1$) compared to the cross section for RDEC into the projectile K-shell. Nefiodov [49] calculated the RDEC cross section into the projectile excited state $1s^1 2s^1$ to be given by

$$\sigma_{RDEC}^{1s^1 2s^1} = \frac{2^{15}}{3} \frac{\sigma_\circ Z_t^3}{\nu Z_p^5} F(\kappa), \tag{2.44}$$

where the universal function $F(\kappa)$ for a given Sommerfeld parameter κ can be found from the left panel of Fig. 2.11. Referring to Eqs. (2.39) and (2.44), the RDEC/REC ratio is given by

$$R' = \frac{\sigma_{RDEC}^{1s^1 2s^1}}{\sigma_{REC}^{1s}} = \frac{2^5}{\pi^2} \frac{Z_t^2}{\nu Z_p^5} \frac{F(\kappa)}{H(\kappa)}, \tag{2.45}$$

where the universal ratio $F(\kappa)/H(\kappa)$ for a given Sommerfeld parameter κ can be estimated from the right panel of Fig. 2.11. The KL-RDEC/KK-RDEC cross section ratio can be expressed based on Eqs. (2.38) and (2.44) by

$$R'' = \frac{\sigma_{RDEC}^{1s^1 2s^1}}{\sigma_{RDEC}^{1s^2}} = \frac{1}{2^4} \frac{F(\kappa)}{Q(\kappa)}. \tag{2.46}$$

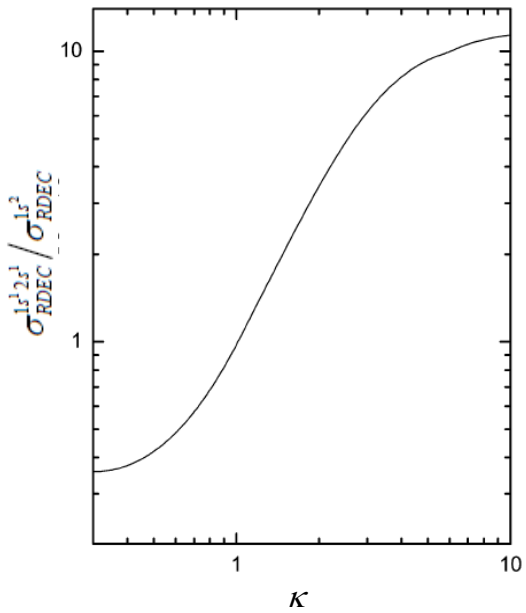

FIG. 2.10. The ratio $R'' = \sigma_{RDEC}^{1s^1 2s^1} \big/ \sigma_{RDEC}^{1s^2}$ as a function of Sommerfeld parameter κ. (adapted from Ref. [49]).

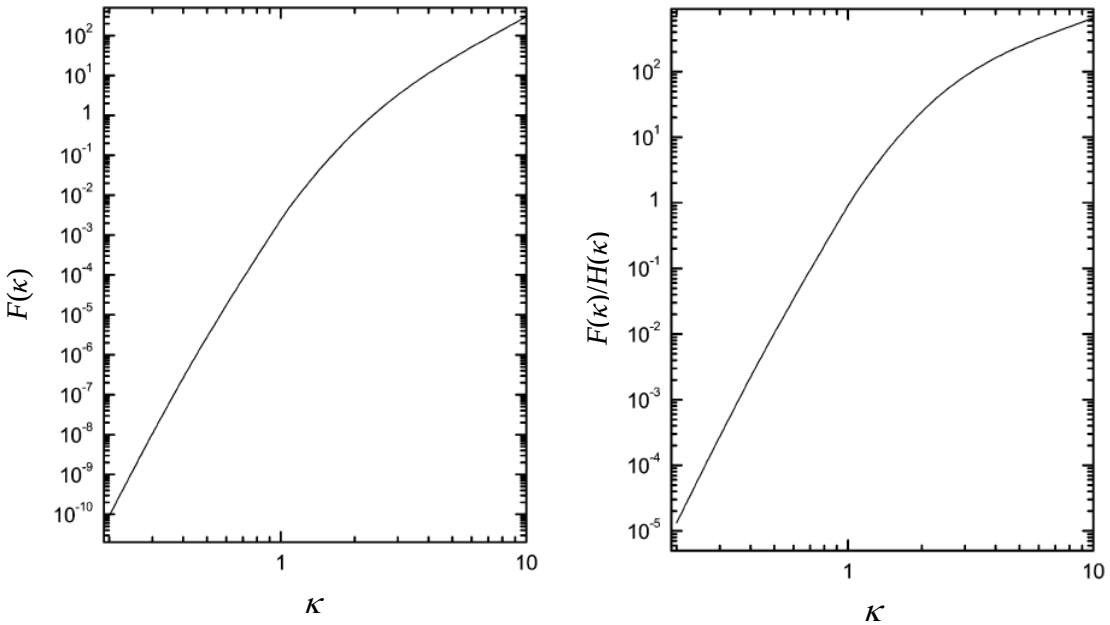

FIG. 2.11. The universal quantities of $F(\kappa)$ (left panel) and $F(\kappa)/H(\kappa)$ (right panel) as functions of Sommerfeld parameter κ. (adapted from Ref. [49]).

No universal graph was introduced for the ratio $F(\kappa)/Q(\kappa)$, hence the left panels of Figs. 2.9 and 2.11 are to be used individually, or simply Fig. 2.10 can be directly used. The value obtained for R'' is more reliable than the values obtained from Eqs. (2.41) and (2.45) since it does not depend on the dimensionless volume ν as an origin of large error.

All the REC and RDEC cross sections with the ratios included from theory and experiment are tabulated within Tables 2.1, 2.2, and 2.3 for the Ar^{18+} and U^{92+} experiments conducted at GSI in 1994 [51] and 2002 [52], respectively.

TABLE 2.1. Measured versus calculated (from Bethe-Salpeter) total K-REC cross sections for the experiments discussed in Secs. 2.3.2 and 2.3.4.

Z_p	E_p (MeV/u)	κ	Z_t	σ_{REC}^{1s} (b/atom)	
				B-S [67]	Exp
18 [51]	11.4	0.84	6	360	685 ± 40
92 [52]	297	0.84	18	1080	---

2.3.7 The First Observation of RDEC

RDEC was first observed by our group using the tandem Van de Graaff accelerator facility at Western Michigan University for the collision system O^{8+} with a thin carbon foil of thickness 1.3×10^{17} atom/cm^2 at 2.38 MeV/u. The carbon foil was mounted at 45° to the beam direction and x rays were registered at an observation angle of 90° in coincidence with ions that captured one and two electrons or no electrons. Si-surface barrier particle detectors counted the charge-changed projectile ions. PIXE analysis of the target foil was performed with 3-MeV protons and no

evidence of characteristic x rays due to contaminations was found in the REC (1.7–2.3 keV) or RDEC (2.8–4.2 keV) energy ranges.

A beam of 38 MeV O^{7+} was also used so that a projectile system of a half-filled K-shell can be used to block the KK-RDEC. This reflects on a difference in the structure of the x rays in the RDEC energy region, which was verified by finding no significant structure in the case of the O^{7+} beam compared to an obvious structure in the RDEC energy domain in the case of the O^{8+} beam.

The data acquisition system allowed for the x rays to be registered in coincidence with particles so that spectra dedicated to x rays associated with single (O^{7+}) and double capture (O^{6+}) were generated as shown in the panels (a) and (b), respectively, of Fig. 2.12. Evidence for RDEC structure was observed in the energy region corresponding to these events in the spectra of x rays associated with double and single capture in a ratio of about 1:10, respectively. Also, REC events were seen in both the spectra of x rays associated with single and double capture, respectively. Having RDEC in the spectrum of x rays associated with single capture (O^{7+}) was attributed to the prompt ionization of the electrons captured to L-shell for which the ionization probability is about one order of magnitude larger than the K-shell ionization [96,97]. Appearance of REC in the x-ray spectrum associated with double capture (O^{6+}) was attributed to nonradiative electron capture (NRC) accompanying REC as uncorrelated events. No contribution was found to the RDEC energy domain

from any of the background processes. The total number of RDEC events measured was 357 giving a total RDEC cross section of 5.5 ± 3.2 b/atom

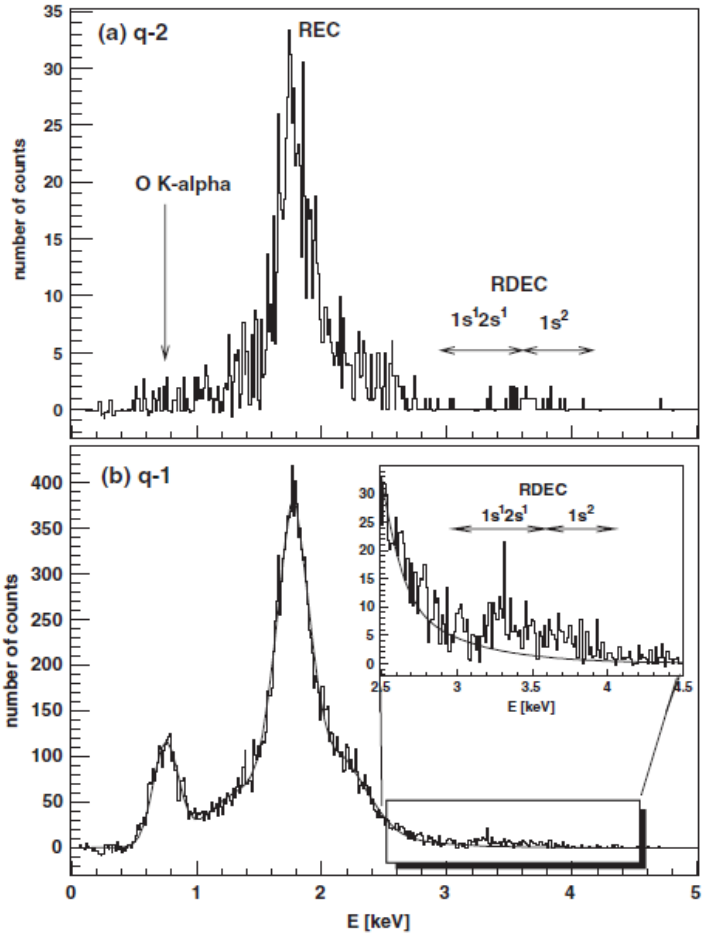

FIG. 2.12. X rays associated with (a) double capture and (b) single capture for O^{8+} + C at 38 MeV. The solid line in (b) represents the sum of the REC Compton profile and the Gaussian distribution of the O Kα line fitted to the spectrum (from Ref. [54]).

2.3.8 The Most Recent Theoretical Model of RDEC

In this theoretical model [50], all calculations are performed within the framework of Quantum Electrodynamics (QED) and the line-profile approach (LPA) [98]. It is assumed that two target electrons of equal energies and momenta are

captured in the same direction to the projectile K-shell. The cross section is then integrated over the direction of the emitted photon. The amplitude U_{if} of electron capture is defined via the *S*-matrix given by

$$S_{\mathrm{if}} = \left(-2\pi i\right)\delta\left(E_{\mathrm{f}} - E_{\mathrm{i}}\right)U_{\mathrm{if}}\,. \tag{2.47}$$

Then, the transition probability is given by

$$dw_{\mathrm{if}} = 2\pi\frac{1}{V^2}\left|U_{\mathrm{if}}\right|^2\delta\left(E_{\mathrm{f}} - E_{\mathrm{i}}\right)\frac{d^3\boldsymbol{k}}{\left(2\pi\right)^3}, \tag{2.48}$$

where E_{i} and E_{f} denote the initial and final energies of the entire system. The RDEC cross section is expressed by

$$d\sigma_{\mathrm{if}} = \frac{edw_{\mathrm{if}}}{J}, \tag{2.49}$$

where *e* and *J* are the electron charge and current density of the captured electrons, respectively. The current density is given by

$$J = en_e\upsilon_p, \tag{2.50}$$

where $n_e = N_e/V$ and υ_p are the target-electron density and the projectile velocity in the laboratory frame, respectively. These expressions yields a formula describing the total RDEC cross section by

$$\sigma_{RDEC} = \lim_{N\to\infty}\left(\frac{\omega}{2\pi}\right)^2\left[\frac{K_e}{p_e}\frac{1}{4\pi}N^4\frac{K_e}{2\pi p_e N^2 S}\right]\int dp_\gamma dp_{2e}\left|U_{i,\mathrm{k}\lambda s}\right|^2, \tag{2.51}$$

where N and S are the normalization constant and the area of the cross section of the reaction volume for one incident electron, respectively, while the factor $1/4\pi$ represents the average over the direction of the electron momenta and the last term in the square brackets is for the volume contributions. The momenta p_γ and p_{2e} are denote the emitted photon and the sum of the momenta of the two captured electrons, respectively, while λ represents the photon polarization. Eq. (2.51) simplifies to

$$\sigma_{RDEC} = \lim_{N\to\infty} \frac{1}{2S}\left(\frac{\omega N K_e}{2\pi^2 p_e}\right)^2 \int dp_\gamma dp_{2e} \left|U_{i,\vec{p}_\gamma \lambda s}\right|^2 . \tag{2.52}$$

Two approximations were employed with this theoretical approach. In the first approximation, the electrons are supposed to be distributed homogeneously in the atom $\left(\sigma_{RDEC,A}\right)$, while the second approximation takes into account only the K-shell electrons neglecting all other electrons and assumes the electrons to be distributed homogeneously within the K-shell sphere $\left(\sigma_{RDEC,K}\right)$. As shown in Table 2.2, the two approximations underestimated all the given upper limits of KK-RDEC cross section sections except that $\sigma_{RDEC,A}^{1s^2}$ overestimated the upper limit of 5.2 mb/atom obtained for KK-RDEC in the case of the Ar^{18+} experiment. However, $\sigma_{RDEC,K}$ was 3–4 orders of magnitude lower than the given upper limits for all the RDEC experiments, while $\sigma_{RDEC,A}^{1s^2}$ was found to be one order of magnitude lower than the measured cross sections for the RDEC experiments of U^{92+}, O^{8+} as well as the present work of F^{9+}.

TABLE 2.2. Measured versus calculated KL-RDEC and KK-RDEC cross sections for the experiments discussed in Secs. 2.3.2 and 2.3.4. The abbreviations Che, Nef, Mik, Yak, PDB, and Exp stand for Chernovskaya, Nefiodov, Mikhailov, Yakhontov, principle of detailed balance, and experiment, respectively.

Z_p	E_p (MeV/u)	κ	Z_t	$\sigma_{RDEC}^{1s^1 2s^1}$ (mb/atom)			$\sigma_{RDEC}^{1s^2}$ (mb/atom)				
				Che [50]	Nef [49]	Exp	Che [50]	Mik [47]	Yak [45]	PDB [12]	Exp
18 [51]	11.4	0.84	6	--- ---	2.2	---	120[1] 4.3[2]	3.2[3] 0.003[4]	1.85	45	≤5.2
92 [52]	297	0.84	18	--- ---	6×10^{-4}	---	1.73 0.003	0.025 8×10^{-7}	5000[5] 0.001[6]	5.8	≤10

[1] First approximation involving the whole atom
[2] Second approximation involving only the K-shell
[3] For the capture of two K-shell target electrons
[4] For the capture of two valence target electrons
[5] Relativistic
[6] Nonrelativistic

TABLE 2.3. Measured versus calculated RDEC/REC cross section ratios $R = \sigma_{RDEC}^{1s^2} / \sigma_{REC}^{1s}$ and $R' = \sigma_{RDEC}^{1s^1 2s^1} / \sigma_{REC}^{1s}$ as well as the KL-RDEC/KK-RDEC cross section ratio $R'' = \sigma_{RDEC}^{1s^1 2s^1} / \sigma_{RDEC}^{1s^2}$ for the experiments discussed in Secs. 2.3.2 and 2.3.4. The abbreviations Mik, Yak, Mir, Amu, PDB, Nef, and Exp stand for Mikhailov, Yakhontov, Miraglia, Amusia, principle of detailed balance, Nefiodov, and experiment, respectively.

Z_p	E_p (MeV/u)	κ	Z_t	R ($\times 10^{-6}$)						R' ($\times 10^{-6}$)		R''	
				Mik [47]	Yak [45]	Mir [91]	Amu [90]	PDB [12]	Exp	Nef [49]	Exp	Nef [49]	Exp
18 [51]	11.4	0.84	6	9	3.6	~310	~31	45	≤ 3.1	2	---	0.63	---
92 [52]	297	0.84	18	0.023	0.001	---	---	5.8	---	6×10^{-4}	---	0.63	---

CHAPTER III

BACKGROUND PROCESSES

In ion-atom collisions, several background processes are likely to contribute to the raw x rays and may overlap with the x rays due to REC and RDEC. In the current study, possible contributions from electron-nucleus (e-n) bremsstrahlung, nuclear bremsstrahlung (NB), electron-electron (e-e) bremsstrahlung, the two-step process of uncorrelated double radiative electron capture (DREC), REC combined with nonradiative electron capture to a projectile bound state (NRC), as well as pileup are taken into account during the analysis of the observed x rays. The present work was performed for the collision system of 2.21 MeV/u F^{9+} ions with a thin carbon foil of thickness $(7.7 \pm 1.1) \times 10^{17}$ atom/cm^2 and the background processes are considered in this domain. The most significant background processes are discussed below in detail.

3.1 X-ray Emission from Bremsstrahlung

One of the most significant and well-known mechanisms of continuous x-ray production in atomic scattering is bremsstrahlung [99] for which energies of the emitted photon E_γ and the inelastically-scattered electrons E_{e2} [100] are both continues. These processes are discussed in turn below.

3.1.1 Electron-nucleus (e-n) Bremsstrahlung

Electron-nucleus (e-n) bremsstrahlung is the dominant kind of background radiation, emitted when an electron scatters from an ion. Bremsstrahlung is German for “braking radiation” and comes from “bremsen” for “brake” and “strahlung” for “radiation”. X-ray emission due to bremsstrahlung has been the subject of early [101] and recent [102] reviews. The radiation was first seen in 1895 by German physicist W. C. Rontegn [103] when highly-energetic electrons were stopped within a thick metallic target, and more generally when a charge decelerates, or “is braked”, when passing through the Coulomb field of another charge. The observation of such radiation was verified in case of electron-ion, ion-atom [104,105] as well as ion-ion collisions [106], while calculation of it was first done by means of the first Born approximation in 1934 by Bethe and Heitler [107].

In electron-ion collisions, the deflection accompanied with a speed reduction from to υ_{e2} of the incident electron may be attributed to the Coulomb interaction with the target nucleus, which is the main force governing this process. In the nonrelativistic approach, the associated energy loss ΔK_e of an electron, incoming with energy E_{e1} and scattered with energy E_{e2}, is given by

$$\Delta K_e = \frac{m_e}{2}\left(\upsilon_{e1}^2 - \upsilon_{e2}^2\right) = E_{e1} - E_{e2}. \tag{3.1}$$

The principle of conservation of energy implies the emission of photons, meaning that the kinetic energy loss ΔK_e of the electron is converted into the form of

a photon as indicated in Fig. 3.1 for e-n bremsstrahlung. ΔK_e can be expressed in terms of the Planck constant h, the speed of light c and the emitted wavelength λ by

$$\Delta K_e = \frac{hc}{\lambda} = E_\gamma . \tag{3.2}$$

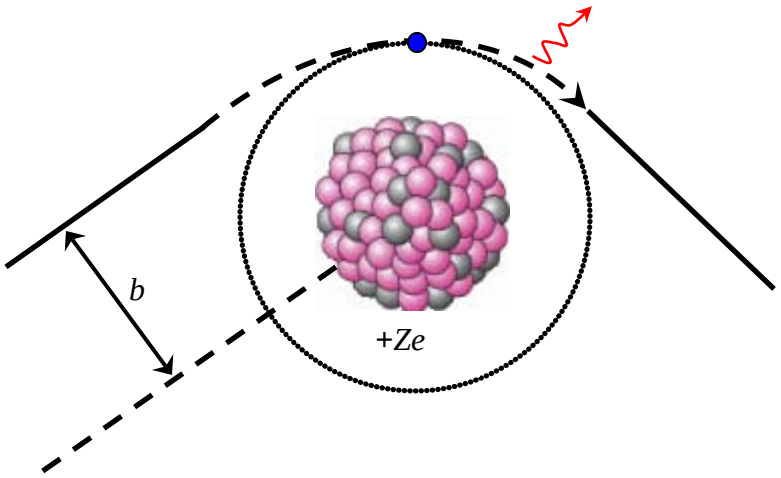

FIG. 3.1. Schematic showing the hyperbolic trajectory of the incoming electron in e-n bremsstrahlung, where b is the impact parameter, Z is the atomic number of the target atom and e is the charge of the incident electron.

The continuous range of x-ray emission has its origin in the fact that not all the electrons are decelerated to the same degree. This can be attributed to the different impact parameter b of each electron, assuming that all incident electrons have the same kinetic energy. This indicates that the larger impact parameter has less braking and, in turn, has longer emitted wavelength, giving a smaller bremsstrahlung cross section. For the same energy of the incoming electron and assuming the same distance of closest approach, a fully-stripped ion will give the maximum bremsstrahlung cross section compared to a minimum cross section for singly-

charged (H-like) ions. This is due to the screening effect caused by the target bound electrons, which reduces the nuclear effective charge seen by the incident electron. The bremsstrahlung spectrum is characterized by a cutoff frequency (higher limit). This limit is reached when the electron is stopped ($\upsilon_{e2} = 0$, i.e., $E_{e1} = \Delta K_e$) in the target and corresponds to a lower limit of the emitted wavelength λ_0 (in nm) given by Duane-Hunt [108] in terms of E_{e1} (in keV) as

$$\lambda_0 = \frac{hc}{\Delta K_e} = \frac{1.24}{E_{e1}}. \tag{3.3}$$

The emission of soft x rays has a lower limit of 1.24 keV, which is the least kinetic energy of the incident electron required for x-ray emission. If the impact parameter is too large, the electron feels little Coulomb field of the target nucleus and hence, the incoming electron does not undergo bremsstrahlung.

The spectral distribution of the emitted x rays due to bremsstrahlung is given in terms of radiation intensity *I*, empirical parameter k', and electron current *i* by the Kramers formula [109] given by

$$I(\lambda) = \frac{k'iZ}{\lambda^2}\left(\frac{\lambda}{\lambda_0} - 1\right). \tag{3.4}$$

The maximum intensity $I_{\max}$ may be determined in terms of an empirical parameter k'' given by the Ulrey formula [110]

$$I_{\max} = k''iZ\Delta K_e^2. \tag{3.5}$$

It was found that the continuous spectrum from bremsstrahlung shifts to shorter wavelengths and becomes more intense with the increase of the energy of the incoming electron (or the captured electron in the rest frame of projectile in case of ion-atom collisions) as shown in Fig. 3.2.

It should be noticed that Z in the text above and section 3.1.4 is used for the target atomic number in case of electron-ion collisions, while the terms Z_p and Z_t are used for the atomic numbers of the projectile and target nuclei, respectively, in case of ion-atom collisions. Similarly, the projectile velocity is denoted υ_e in electron-ion collisions and υ_p in ion-atom collisions.

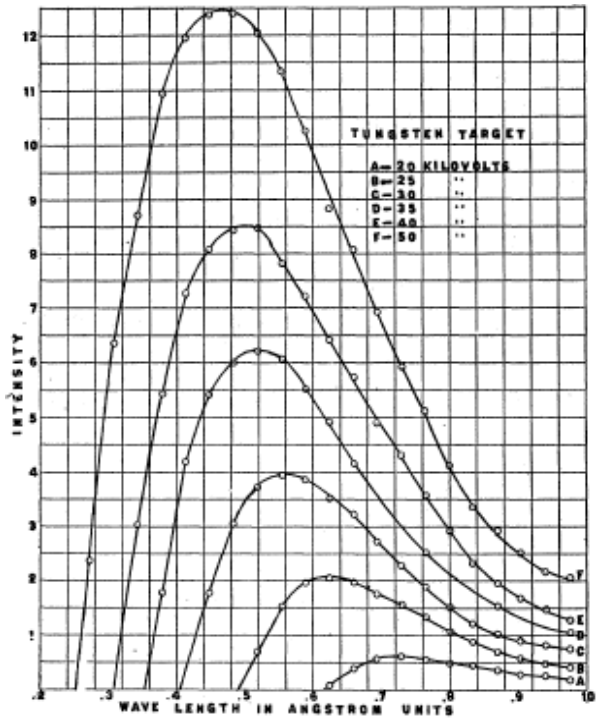

FIG. 3.2. Bremsstrahlung spectrum of a tungsten target bombarded with electrons over a voltage range of 20–50 kV (from Ref. [110]).

The captured electron in ion-atom collisions encounters various mechanisms of e-n bremsstrahlung in the vicinity of the projectile such as radiative electron capture to continuum (RECC) [85,111,112,113,114,115,116,117], radiative ionization (RI) [118,119], secondary electron bremsstrahlung (SEB) [104,120], and atomic bremsstrahlung (AB) [121,122,123,124].

RECC can be treated as quasi-free electron bremsstrahlung (QFEB) [125,126] and is sometimes called [113] primary bremsstrahlung (PB) [81] or radiative ionization (RI), depending on the analogy of the production mechanisms. However, RI within this dissertation is interpreted differently from RECC as indicated by Ishii [119]. During RI, the target electron is not captured to the projectile continuum (QFEB) but ionized away from the projectile with simultaneous emission of a photon. If the target electron is ionized and transferred to the projectile continuum then, this is QFEB as a special case of RI.

RECC was first observed by Kienle [127] and Schnopper [128] with a maximum nonrelativistic photon energy emitted [129] given by

$$T_r = \frac{m_e \upsilon_p^2}{2\left(1.6\times10^{-19}\right)} = \left(\frac{m_e}{M_p}\right) E_p , \tag{3.6}$$

where E_p is the projectile energy in eV/u and υ_p is the velocity of the projectile in m/s, which is the same as the velocity of the ejected target electron in the projectile

rest frame, while the masses m_e and M_p are given in kg for the ejected target electron and projectile, respectively. The relativistic value of T_r is given by [81]

$$T_r = \left[\sqrt{\left(\gamma\beta + \frac{p_z}{m_e c} \right)^2 + 1} - 1 \right] m_e c^2 . \tag{3.7}$$

Eqs. (3.8) [130] and (3.9) [131] are introduced to show the trend of the differential RECC cross section and its complementary process, nonradiative electron capture to the continuum (ECC) [132,133,134,135], respectively.

$$\frac{d\sigma_{RECC}}{d\upsilon_p'}(nl \to cont) \sim \frac{2^6}{3} Z_p^3 \left(\frac{e^2}{\hbar c} \right)^3 \left(\frac{e^2}{\hbar \upsilon_p} \right)^3 \left(\frac{1}{\upsilon_p^2} \right) \left(\sqrt{\left(\upsilon_p' - \upsilon_p \right)^2 + \left(\upsilon_p \theta_\circ \right)^2} - \left| \upsilon_p' - \upsilon_p \right| \right) \left(\pi a_\circ^2 \right), \tag{3.8}$$

$$\frac{d\sigma_{ECC}}{d\upsilon_p'}(nl \to cont) \sim \frac{2^{17}}{5} Z_p^3 Z_t^5 \left(\frac{e^2}{\hbar \upsilon_p} \right)^{10} \left(\frac{1}{\upsilon_p^2} \right) \left(\sqrt{\left(\upsilon_p' - \upsilon_p \right)^2 + \left(\upsilon_p \theta_\circ \right)^2} - \left| \upsilon_p' - \upsilon_p \right| \right) \left(\pi a_\circ^2 \right), \tag{3.9}$$

where $a_\circ$ is the reduced Planck constant and $\hbar$ is the Bohr radius. The laboratory velocities of projectile in the 4π space and of the target electrons ejected into a cone of specific semi-angle $\theta_\circ$ are denoted by υ_p and υ_p', respectively. The υ_p - dependence of the differential cross section is υ_p^{-5} and υ_p^{-12} for RECC and ECC, respectively. Schematic diagrams for the mechanisms are viewed in Fig. 3.3. A scaling law for the RECC total cross section [86] was addressed later given by

$$\sigma_{RECC} \propto \frac{Z_p^2 Z_t}{\upsilon_p^2} . \tag{3.10}$$

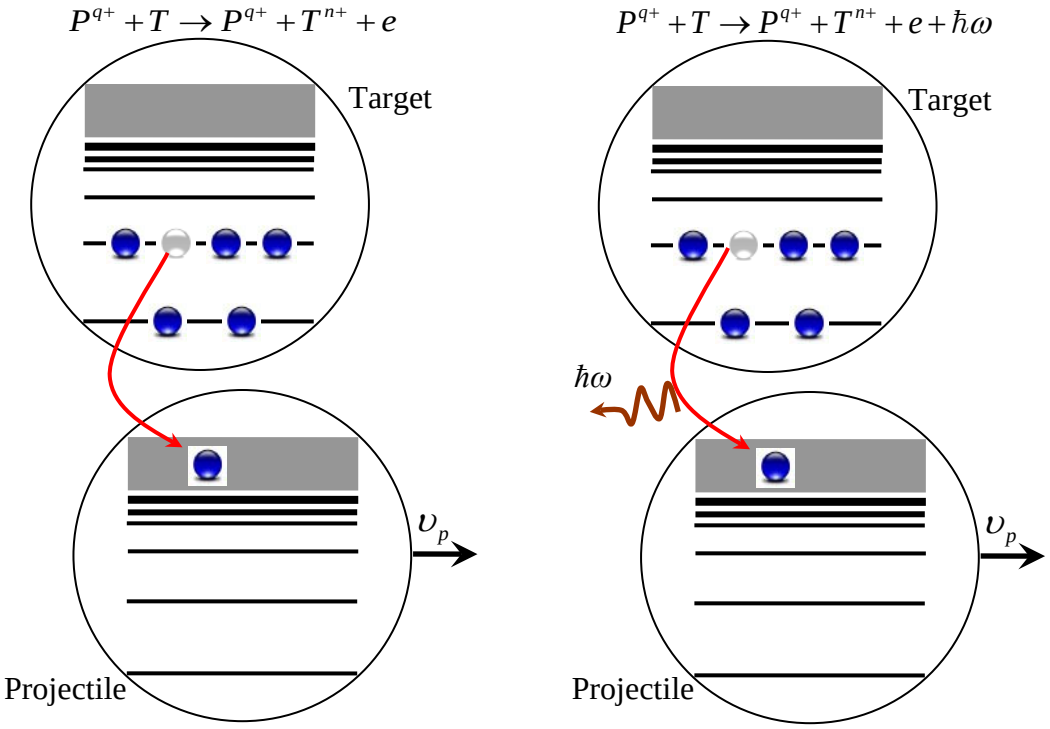

FIG. 3.3. Same as Fig. 2.2 but for ECC (left panel) and RECC (right panel).

The double differential RI cross section (DDCS) according to Ishii [119] is given by

$$\frac{d^2\sigma_{RI}}{d(\hbar\omega)d\Omega}=\frac{2a_\circ^2\alpha^5}{\pi\hbar\omega}Z_p^2\left(\frac{c}{\upsilon_p}\right)^2\sum_n\int_{\delta_n/n^2}^{\infty}dW\int_{Q_{\min}}^{\infty}\frac{dQ}{Q}F_{n,W}(Q)\left(1-\frac{Q_{\min}}{Q}+\left(\frac{3}{2}\frac{Q_{\min}}{Q}-\frac{1}{2}\right)\sin^2\theta\right),$$

$$Q_{\min}=\frac{\left(WZ_n^2R_y+\hbar\omega\right)^2}{2m_e\upsilon_p^2Z_n^2R_y}, \qquad (3.11)$$

where $F_{n,W}(Q)$ is given by Merzbacher and Lewis [136], the variables Q and W are given by Inokuti [137], while δ_n and Z_n are the screening factor for an atomic shell and the effective charge seen by the orbital electron, respectively, both for principal quantum number n. The symbols ω and θ denote the angular frequency of the

emitted photon and the observation angle of x rays with respect to the projectile velocity υ_p, respectively, while α and R_y denote the fine structure of the atom and the Rydberg constant, respectively. However, RI should be more significant in slow than in fast collisions [118] and it is hard to derive a scaling rule for such process.

The SEB process involves two steps and occurs if a target electron is ejected due to the Coulomb interaction with the projectile then scattered by the Coulomb field of another target nucleus. SEB is characterized [129] by a photon energy

$$T_m = 4\left(\frac{m_e}{M_p}\right)E_p = 4T_r\,, \tag{3.12}$$

which corresponds to the maximum energy transferred from a projectile of mass M_p to a free electron at rest. However, SEB was found to be less important for low-*Z* targets such as Be and C [138,139] based on the cross section calculated from the Koch bremsstrahlung formula (3BN) [101] and the scaling rule [123,140] given by

$$\sigma_{SEB} \propto \frac{Z_p^2 Z_t^2}{\upsilon_p^2}\,. \tag{3.13}$$

The double differential cross section for SEB according to Ishii [119] is given in terms of C_1 and C_2 as defined in detail in the same publication by

$$\frac{d^2\sigma_{SEB}}{d(\hbar\omega)d\Omega} = \frac{1}{2\pi}Z_p^2 Z_t^2\left(\frac{e^2}{\hbar c}\right)^5 a_\circ^2\frac{m_e c^2}{(\hbar\omega)^2}\left(C_1 + C_2\sin^2\theta\right). \tag{3.14}$$

The AB, also called polarization bremsstrahlung (PBS) [119,141,142], was first recognized in the middle of the 1970s [143,144,145,146,147] and is completed if

a target electron is excited to the target continuum due to the Coulomb field of the projectile then de-excited with the simultaneous emission of a single photon. A scaling law for the differential AB cross section [148] was addressed later by

$$\frac{d\sigma_{AB}}{d(\hbar\omega)} \propto \frac{Z_p^2}{\upsilon_p^2}. \tag{3.15}$$

In heavy-ion-atom collisions, the double differential cross section is given by [119]

$$\frac{d^2\sigma_{AB}}{d(\hbar\omega)d\Omega} = \frac{8a_\circ^2\alpha^5}{\pi\hbar\omega}\left(\frac{c}{\upsilon_p^2}\right)\int_{\omega/\upsilon_p}^{\infty}\frac{dq}{q}\left\{1-\left(\frac{\omega}{q\upsilon_p}\right)^2+\left(\frac{3}{2}\left(\frac{\omega}{q\upsilon_p}\right)^2-\frac{1}{2}\right)\sin^2\theta\right\}$$
$$\times\left|Z_pS_{Zt}(q)-Z_tS_{Zp}(q)\right|^2, \tag{3.16}$$

where $Z_pS_{Zt}(q)$ and $Z_tS_{Zp}(q)$ are the AB contributions from the target and projectile atoms, respectively, and $\left|Z_pS_{Zt}(q)-Z_tS_{Zp}(q)\right|^2$ vanishes for symmetric collisions, i.e., when $Z_p = Z_t$.

The calculations [149] for AB, RI and SEB are compared with experimental results of AB and the total contribution of the three processes as shown in Fig. 3.4 for a thin Al foil bombarded with protons at collision energies of 1 (left panel) and 4 MeV (right panel), respectively. For 1-MeV protons, the predominant calculated part of the continuous x rays is due to AB, which is in excellent agreement with the experiment, while the contributions of SEB and RI are small and can be neglected. On the other hand, the main calculated part of continuous x rays in case of 4-MeV protons originates from SEB compared to the very small contributions of RI and AB.

The net calculated contribution of SEB, AB, and RI is again in excellent agreement with the experiment.

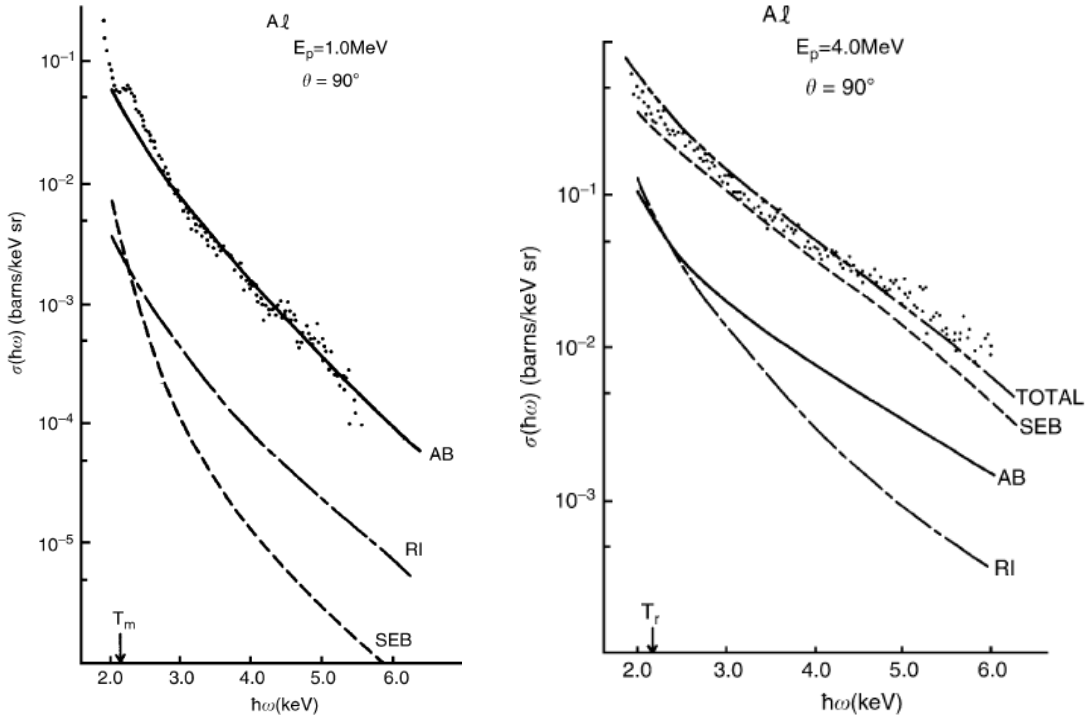

FIG. 3.4. Calculated contributions of AB, RI, and SEB versus measured contribution of AB for 1 MeV H^+ + Al (left panel) and versus the measured and calculated total contribution of the three processes for the x-ray emission for 4 MeV H^+ + Al (right panel), both at 90° (from Ref. [119]).

3.1.2 Nucleus-nucleus (n-n) Bremsstrahlung

Nucleus-nucleus (n-n) bremsstrahlung, also called nuclear bremsstrahlung (NB), was intensively treated theoretically [150,151] and first observed for heavy-ions collisions in 1976 [152], provided that this component of the continuous spectrum is isolated from the other x-ray emission processes. It was shown in a more recent study of n-n bremsstrahlung for ultrarelativistic collisions [153] that the

bremsstrahlung radiation emitted at relativistic energies for heavy-ion collisions is a sensitive indicator of the collision transparency, i.e., how decelerated the positive charges are. It was also found that the bremsstrahlung emission dominates at relatively-low photon energies (less than a few MeV) as shown in Fig. 3.5 and is concentrated at angles within 10° to the line of the colliding beams.

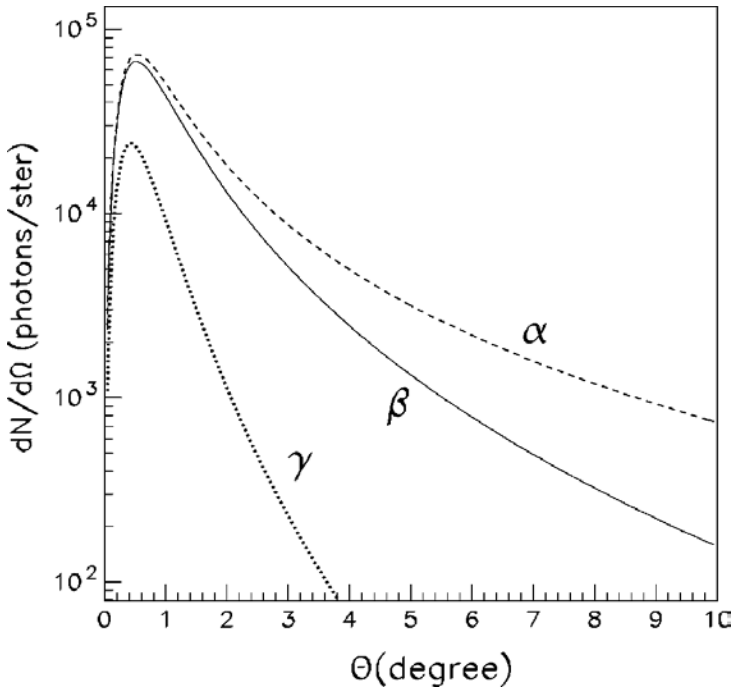

FIG. 3.5. The number of photons due to bremsstrahlung as a function of angle for central collisions of gold in the energy range 10 keV – 3 MeV. The three curves correspond to α, β, γ, which categorize as "full stopping", "50% stopping", and "near transparency", respectively (from Ref. [153]).

The double differential cross sections of n-n bremsstrahlung can be evaluated [119] by means of the second Born approximation according to Heitler [154] from a formula [155] given by

$$\frac{d^2\sigma_{NB}}{d(\hbar\omega)d\Omega}=\frac{Z_p^4Z_t^2}{\pi\hbar\omega}\left(\frac{e^2}{m_ec^2}\right)^2\left(\frac{m_e}{M_p}\right)^2\frac{e^2}{\hbar c}\left(\frac{c}{\upsilon_p}\right)^2\left(1-\frac{M_pZ_t}{Z_pM_t}\right)^2$$

$$\times\left(\ln\frac{4E_p}{\hbar\omega}-\ln\frac{Z_pZ_te^2}{\hbar\upsilon_p}-\frac{1}{2}-\frac{1}{2}\left(\ln\frac{4E_p}{\hbar\omega}-\ln\frac{Z_pZ_te^2}{\hbar\upsilon_p}-\frac{3}{2}\right)\sin^2\theta_\omega\right). \qquad (3.17)$$

A scaling law for the differential NB cross section [148] was addressed later by

$$\frac{d\sigma_{NB}}{d(\hbar\omega)}\propto\frac{Z_p^2Z_t^2}{\upsilon_p^2}. \qquad (3.18)$$

3.1.3 Nucleus-nucleus (n-n) versus Electron-nucleus (e-n) Bremsstrahlung

The x-ray contribution from QFEB, SEB, AB, and NB are shown in Fig. 3.6 [119] for 2 MeV protons striking with carbon. This figure shows that QFEB and SEB are predominant in the photon-energy region $\hbar\omega\le T_r$ and $T_r<\hbar\omega<T_m$, respectively [129], while AB extends over a wide range lower and higher than T_m with a similar trend to SEB. On the other hand, the figure shows that NB has a very small contribution to the continuous x-ray spectrum compared to the other e-n bremsstrahlung processes for x-ray energies less than about 10 keV. This requires that NB has to be given special care during measurements of this process by taking into account the background target γ rays and signal pileup.

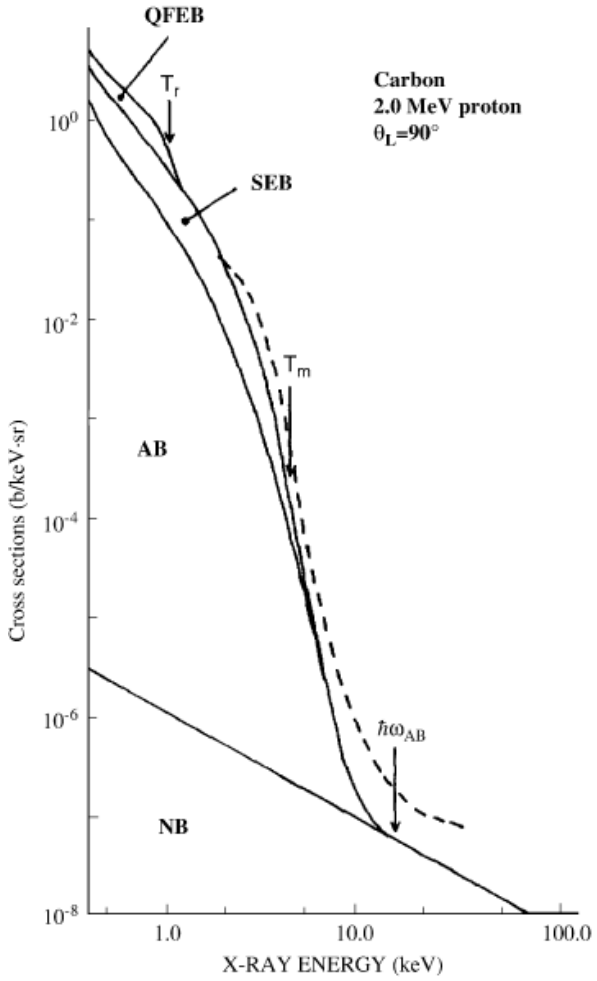

FIG. 3.6. Bremsstrahlung spectrum for 2 MeV H^+ + C (from Ref. [119]). The dashed line is for the experimental results taken by Folkmann [104].

The differential cross sections of continuous x rays are shown in Fig. 3.7 for 1.5 MeV H^+ + Al collisions at 90° [156]. In this figure, the NB contribution is predicted by means of Eq. (3.17), allowing for the conclusion that the cross section of NB becomes a minimum at 90°, while SEB and AB were calculated by means of Eqs. (3.14) and (3.16), respectively. It is seen that the contribution of NB is predominant in

the energy region $\hbar\omega > 15$ keV, while AB is predominant in the energy region $\hbar\omega < 15$ keV and SEB can be neglected in the energy region $\hbar\omega > 10$ keV.

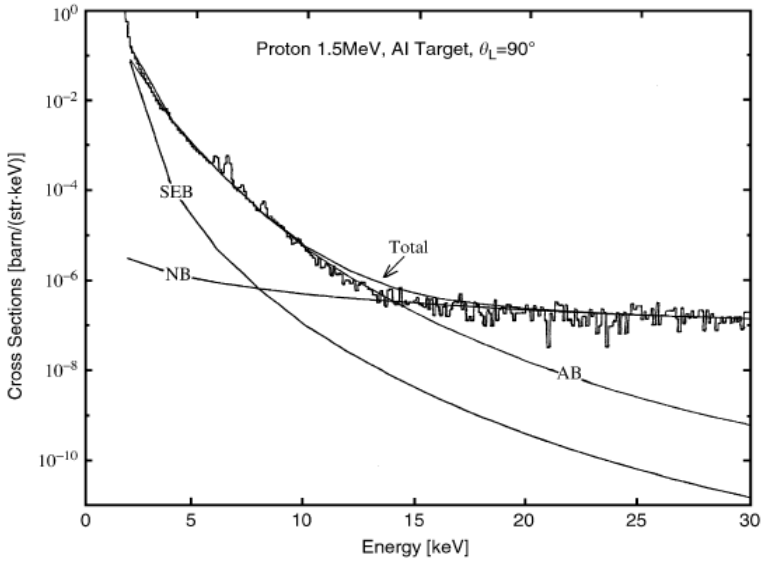

FIG. 3.7. Calculated contributions of NB, AB, SEB, and the total of the three processes versus the measured total contribution of the three processes for 1.5 MeV H^+ + Al at 90° (from Ref. [119]).

3.1.4 Electron-electron (e-e) Bremsstrahlung

Electron-electron (e-e) bremsstrahlung originates from the interaction between the incoming electrons and the bound target electrons. It is particularly hard to measure the DDCS $\left(d^2\sigma/d\Omega_e dE_e\right)$ of such process [157,158,159]. The contribution of e-e bremsstrahlung can be isolated from the total bremsstrahlung only by measuring the triply-differential cross sections (TDCSs) $\left(d^3\sigma/d\Omega_e d\Omega_\gamma dE_e\right)$ by means of the technique of γ-e coincidences [99,160,161]. This technique was suggested by Scherzer in 1932 [162] and calculated by Hodes in 1953 [163] in the Born

approximation, i.e., first order perturbation theory, then applied by Nakal and coworkers in 1966 [164,165,166]. The e-e bremsstrahlung was found to have a contribution of $1/Z$ of the net bremsstrahlung radiation [167] based on which it can be neglected in the case of high-Z targets. In general, e-e bremsstrahlung is not taken into account in most of the bremsstrahlung measurements due to its small contribution to the total bremsstrahlung emission [168]. In contrast, the cross section of e-n bremsstrahlung scales closely to Z^2 for unshielded nuclei [168,169], while there is no simple Z-dependence for shielded nuclei [169]. The contribution of e-e versus e-n bremsstrahlung is shown in Fig. 3.8 for e + C in which a peak dedicated to e-e bremsstrahlung appears at 91 keV followed by a peak for e-n bremsstrahlung at 140 keV.

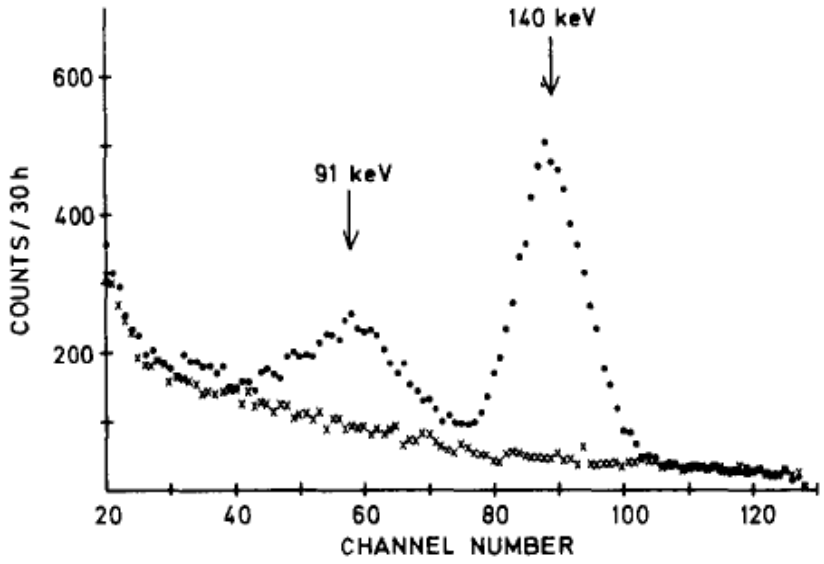

FIG. 3.8. Bremsstrahlung spectrum (full circles) measured at -34° for e + C at a collision energy of 300 keV in coincidence with 160 keV outgoing electrons at 28°. The measured random coincidences (crosses) are also shown (from Ref. [161]).

3.2 Nonradiative Electron Capture (NRC)

In NRC, sometimes called Coulomb capture [170], a target electron is captured to the bound state of the projectile without an accompanying photon emission as indicated in Fig. 3.9. Instead, the difference between the projectile initial and final states is converted to a kinetic energy gained by the projectile. NRC dominates at velocity matching conditions, i.e., when the projectile velocity υ_p matches the orbital velocity υ_{et} of the target electron.

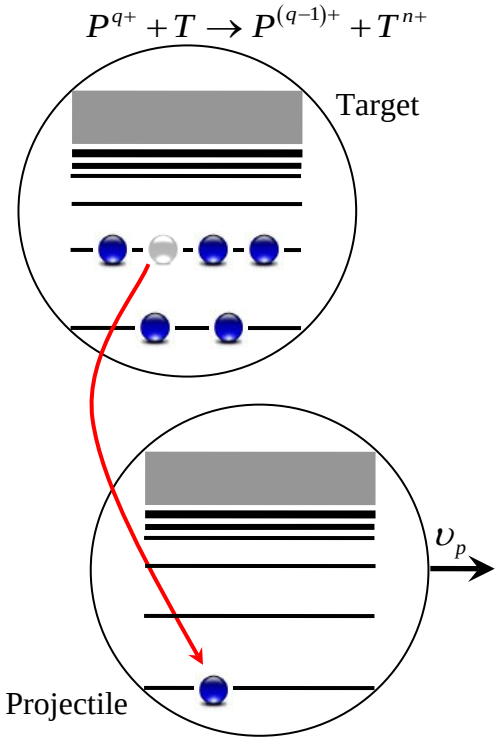

FIG. 3.9. Same as Fig. 2.2 but for the atomic process NRC to the target K-shell.

According to Schlachter [171] and provided that the conditions of single collision exist, the total cross section σ_{NRC} in cm^2/atom can be calculated by means of the semi-empirical formula given by

$$\sigma_{NRC} = 1.1\times10^{-8}\left(\frac{q^{3.9}Z_t^{4.2}}{E_p^{4.8}}\right), \tag{3.19}$$

where q is the projectile charge state and E_p is measured in keV/u.

It is possible that REC counts appear in the spectrum of x rays associated with double capture if two target electrons are captured independently to the same projectile, one radiatively (REC) and the other nonradiatively (NRC). In such case, NRC accompanies REC as two uncorrelated processes. Hence, the estimation for the probability of having NRC accompanying REC helps avoid underestimating the REC cross section by considering the additional counts that appear in a different capture channel (double capture). Thus, a more accurate RDEC/REC cross section ratio can be obtained for the sake of comparison with the theoretical predictions of such a ratio. The individual contributions of both REC and NRC as well as their net contribution are shown in Fig. 3.10 for U^{92+} + N_2 [84]. The dipole approximation was used to obtain σ_{REC}, while the eikonal approach was used to calculate σ_{NRC}. The solid line refers to the sum of REC (dashed line) and NRC (dotted line) predictions.

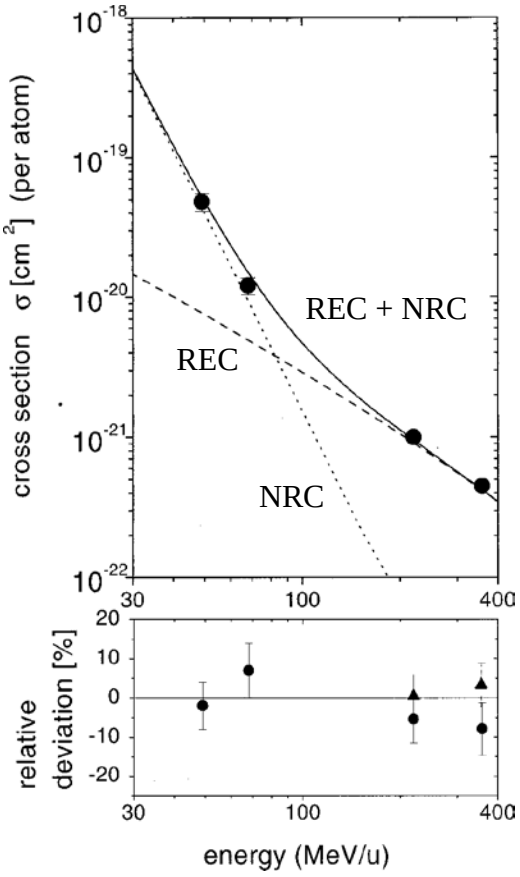

FIG. 3.10. Predicted total cross sections of electron capture, radiatively (dashed line), nonradiatively (dotted line), and the sum of both (solid line) for U^{92+} + N_2 versus projectile energy. The lower part of the figure indicates the relative deviation between experiment and theory, i.e., $\left(\sigma_{theory}-\sigma_{\exp}\right)/\sigma_{theory}$. The solid triangles refer to the cross sections obtained from rigorous relativistic calculations, whereas the full circles refer to the dipole approximation (adapted from Ref. [84]).

However, σ_{NRC} scales differently if specific capture channels from target to projectile are taken into account, such as $1s \to 1s$ and $1s \to 2p$ [131] as given by

$$\sigma_{NRC}\left(1s \to 1s\right) \sim \frac{2^{18}}{5} Z_p^5 Z_t^5 \left(\frac{e^2}{\hbar \upsilon_p}\right)^{12} \left(\pi a_\circ^2\right), \tag{3.20}$$

$$\sigma_{NRC}\left(1s \to 2p\right) \sim \frac{2^{16}}{3} Z_p^7 Z_t^5 \left(\frac{e^2}{\hbar \upsilon_p}\right)^{14} \left(\pi a_\circ^2\right). \tag{3.21}$$

For fast but nonrelativistic collisions, σ_{NRC} scales as

$$\sigma_{NRC} \propto \frac{Z_p^5 Z_t^5}{\upsilon_p^{11}}. \tag{3.22}$$

3.3 Double Radiative Electron Capture (DREC)

Double radiative electron capture (DREC) can contribute at the energy-region of REC in the spectrum of x rays associated with single capture when two REC photons are emitted due to the capture of two uncorrelated target electrons by the same projectile, i.e., during a single ion-atom collision as indicated in the schematic diagram viewed in Fig. 3.11. Each of the DREC photons has the same energy of the REC photon, while the two captured electrons transfer independently to the projectile. The estimation of the DREC contribution helps avoid overestimating the REC cross section by subtracting the DREC contribution from the REC counts in the double capture channel, i.e., when REC is accompanied with NRC as indicated in Sec. 3.2, while it is very unlikely that DREC contribute to RDEC in the double capture channel when the two DREC photons are emitted in the same direction and registered as a single photon of double energy. This all reflects into a more reliable REC cross section as well as RDEC/REC cross section ratio for the sake of comparison with various theoretical predictions.

A numerical evaluation of the total DREC cross section σ_{DREC} from a target of atomic number Z_t was given by Meyerhof [172] based on the independent-electron approximation [173]. If $P_\circ(b)$ is the probability of a single-electron capture to a fully-stripped ion, then for a target electron density $\rho(R)$ and a projectile-to-

target distance R as the hypotenuse of the right-angle triangle whose other two sides are the impact parameter b and the travel path of the beam z, $P_\circ(b)$ is given [131] by

$$P_\circ(b) = \sigma_{REC}(Z_t = 1) \int_{-\infty}^{\infty} dz \rho(R). \tag{3.23}$$

Accordingly, the REC cross section σ_{REC} for a target of atomic number Z_t in terms of $\sigma_{REC}(Z_t = 1)$, which can be calculated from Eq. (2.13), can be expressed by

$$\sigma_{REC}(Z_t) = \int_0^{\infty} db 2\pi b P_\circ(b). \tag{3.24}$$

Substituting Eq. (3.23) into Eq. (3.24) gives

$$\sigma_{REC}(Z_t) = \sigma_{REC}(Z_t = 1) \int_0^{\infty} db 2\pi b \int_{-\infty}^{\infty} dz \rho(R). \tag{3.25}$$

Since the electron density is normalized, this requires that

$$\int_0^{\infty} db 2\pi b \int_{-\infty}^{\infty} dz \rho(R) = Z_t. \tag{3.26}$$

The atomic density can be calculated by means of the Thomas-Fermi theory [174] and it can be deduced from Eqs. (3.25) and (3.26) that

$$\sigma_{REC}(Z_t) = Z_t \sigma_{REC}(Z_t = 1). \tag{3.27}$$

Introducing $P_1(b)$ as the probability of single electron capture to any H-like ion, the DREC cross section σ_{DREC} for a given target can be expressed similarly by

$$\sigma_{DREC}(Z_t) = \int_0^{\infty} db 2\pi b P_\circ(b) P_1(b). \tag{3.28}$$

A numerical evaluation of σ_{DREC} for a target of atomic number Z_t [172] yields

$$\sigma_{DREC}\left(Z_t\right) = 0.13\sqrt{Z_t}\,\sigma^2_{REC}\left(Z_t\right)a_\circ^{-2}, \tag{3.29}$$

which was verified about two decades later [175] at the GSI complex accelerator facility.

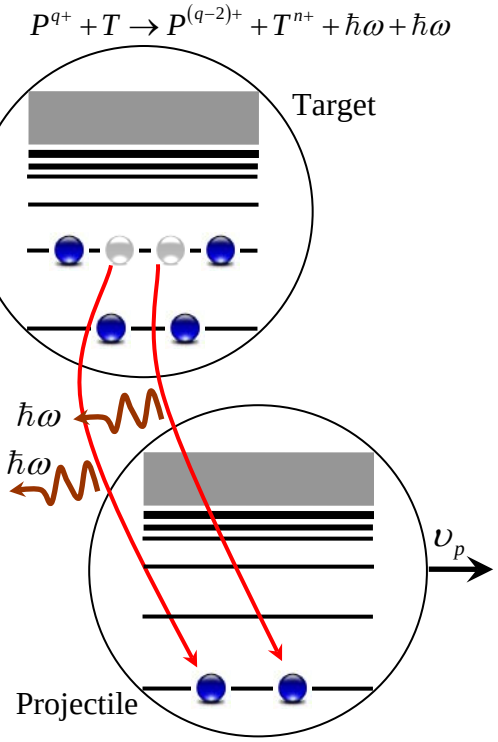

FIG. 3.11. Same as Fig. 2.2 but for the atomic process DREC to the target K-shell.

Table 3.1 summarizes the scaling rules of the cross sections for the atomic processes of interest.

TABLE 3.1. Cross-section scaling for the atomic processes of interest.

Atomic process	Scaling laws of the cross sections
NRC	$\sigma_{NRC} \propto \frac{Z_p^5 Z_t^5}{\upsilon_p^{11}}$ [86,170]
REC	$\sigma_{REC} \propto \frac{Z_p^5 Z_t}{\upsilon_p^5}$ [85,86]
RECC	$\sigma_{RECC} \propto \frac{Z_p^2 Z_t}{\upsilon_p^2}$ [86]
SEB	$\sigma_{SEB} \propto \frac{Z_p^2 Z_t^2}{\upsilon_p^2}$ [86]
AB	$\frac{d\sigma_{AB}}{d(\hbar\omega)} \propto \frac{Z_p^2}{\upsilon_p^2}$ [148]
NB	$\frac{d\sigma_{NB}}{d(\hbar\omega)} \propto \frac{Z_p^4 Z_t^2}{\upsilon_p^2}$ [148]

3.4 Pileup Effect

If more than one photon is incident on the x-ray detector at the same time, then a single photon of energy equal to the sum of the individual energies is detected and a pileup event is registered. This is more likely to happen in the case of higher-beam intensities than for lower-beam intensities as a result of the increase of the number of the pileup photons, which is directly proportional to the square of the beam intensity. The higher probability of pileup at high beam intensities is attributed to the excess of the rate of collisions and hence of the rate of emitted photons through

radiative processes. Pileup as a mechanism applies to characteristic x-ray emission lines, REC or any other source of x-ray emission. The pileup from more than two photons can usually be neglected because of its exceedingly small probability.

The pileup of interest is the one originating from the superposition of two REC photons as emitted from two projectile ions and registered as a single photon of double energy in the spectrum of x rays associated with single capture at the RDEC energy region. An accurate measurement of the REC probability is required so that the corresponding pileup probability can be calculated. In turn, the corresponding number of REC counts lost into pileup counts can be estimated.

The practical technique to block the pileup is to use an attenuator to reduce the photons detected by $>90\%$ in the REC energy range so that the photons causing the pileup are attenuated before they are simultaneously registered. Hence, the number of events dedicated to pileup will be drastically reduced to a limit that can be ignored. The pileup of REC photons will be negligible if the REC rate is low enough. Although a disadvantage of this technique is the reduction of the measured REC cross section as a result of the suppression of most of the photons, a correction factor based on calculations of the attenuation percentage [176] in the energy range under study can be used. Separate short-time measurements of REC with and without using the attenuator can also be performed to determine the actual percentage of reduction of REC photons due to the attenuator. A calculation of the contribution of pileup to the present experimental results is presented in Chapter V.

CHAPTER IV

EXPERIMENTAL SETUP

4.1 Standard Van de Graaff Generator

This work was conducted at the tandem Van de Graaff accelerator facility at Western Michigan University (WMU). The concept of a Van de Graaff generator [177,178] is to store electrostatic charges with the aid of a rotating belt or charging chain so that very high voltages accumulate on the high-voltage terminal. The ideal terminal needs to be a metal of hollow shape [177] based on the fact that all geometrical shapes of electrically-charged conductors have no electric field inside, allowing the terminal to keep adding charges continuously until a saturation between charging and discharging is achieved, i.e., the maximum electrostatic voltage is reached. The Van de Graaff generator was invented in 1929 by American physicist Robert J. Van de Graaff and developed by the same inventor at Princeton University. A model able to generate 1 MV was described in 1931 [178].

A schematic diagram of a basic Van de Graaff accelerator is seen in Fig. 4.1, where an insulating belt runs over two rollers. The upper roller is placed inside the metal terminal and is dedicated to transfer the electrostatic charges. Two electrodes (needles) are placed in contact with the belt at the positions of the two rollers. The upper and lower needles are manufactured to be connected to the terminal and a high

DC potential, respectively, so that the high electric field ionizes the air around the positively-charged lower needles, causing them to repel the ionized air ions to the belt. The belt then transfers the charges accumulated on the lower portion of it to the upper roller and the needles above it until saturation is reached between charging and discharging. At this stage, the terminal of potential V is ready to repel and accelerate any positive charge q that may originate from the accelerator ion source if brought close to the terminal. The produced kinetic energy of the beam is accordingly qV.

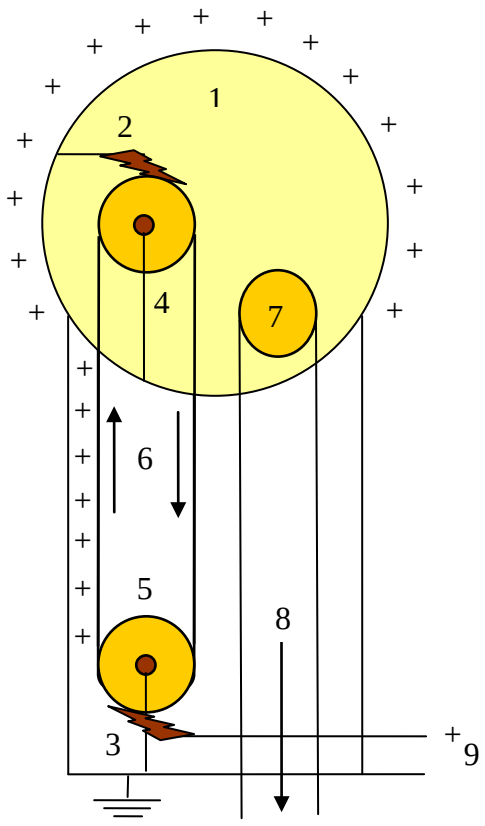

FIG. 4.1. Schematic diagram of a Van de Graaff accelerator: (1) high-voltage terminal, (2) upper needles (discharging electrode), (3) lower needles (charging electrode), (4) upper metal roller, (5) lower metal roller, (6) moving belt, (7) ion source, (8) ion beam, (9) high-voltage supplier.

4.2 Tandem Van de Graaff Accelerator

The concept of acceleration is a bit different in the case of tandem Van de Graaff accelerators [179] such as the one existing at WMU for which the maximum terminal high voltage is 6 MV and other accelerators for which the terminal voltage can reach up to 20 MV [178,179,180]. The accelerator vacuum tube has to be pumped out to an appropriate low pressure (10^{-8}–10^{-7} Torr) before producing the desired beam. Negative ion sources are then used to produce singly-charged negative ions to be attracted with a kinetic energy V to the positively-charged terminal. The terminal is located at the middle of the vacuum tube where two or more electrons are stripped from each singly-charged negative ion by means of a gas, such as O_2, or a thin foil, such as carbon [179]. The charging and discharging electrodes are located at the entrance and the center of the vacuum tube, respectively. At this stage, the terminal high voltage is used for the second time to repel the positively-charged ions with a kinetic energy of qV, where q is the desired beam charge. The total number of electrons removed is equal to $q+1$, giving a net beam kinetic energy of

$$(V + qV) = (q+1)V\,. \tag{4.1}$$

A dielectric gas is not only needed to fill the region around the Van de Graaff terminal (tank) to help avoid the sparks due to tank discharge, but also to condition the machine before reaching high terminal voltages (≥ 5 MV at the tandem Van de Graaff accelerator at WMU). Tank sparks occur inside the tank with loud “bangs”, causing a sudden drop in the terminal voltage, and produce gaseous byproducts that

can react adversely with the needles. Tube sparks are another type of discharge and are considered worse as they discharge inside the vacuum tube with no sound and liberate gas, causing an increase of the vacuum pressure. The ideal dielectric gases are the inert ones such as the very expensive SF_6 and Freon [179]. A mixture of CO_2 and N_2 can be a replacement if seeking a dielectric of lower price. Less dielectric gases are usually used with higher pressures (200–290 psi) than those used in the case of SF_6 (60 psi), where the higher pressure provides more insulation.

4.3 SNICS Negative Ion Source

A fully-stripped fluorine beam with energy 42 MeV was obtained following the production of negative fluorine ions from source of negative ions by cesium sputtering (SNICS II) as well as the subsequent acceleration as shown in Fig. 4.2. In addition, a beam of 3 MeV H^+ from the same ion source was used to conduct elemental analysis of the carbon targets utilizing PIXE measurements.

Cesium-sputtering negative ion sources are widely used in tandem accelerators. The Cs plays a major role in the operation process where the Cs vapor comes out of the Cs oven after it is heated up and enters into a fully-enclosed volume (within the ion source) surrounding the ionizer surface and the cathode. The temperature of the Cs oven can be adjusted so that the flow of Cs into the source is controlled. The ionizer surface is kept hot, causing some of the Cs to become ionized, while some of the Cs condenses on the front of the cooled cathode. The ionized

portion of Cs then accelerates to the cooled cathode, allowing for particles sputtering through the condensed portion of Cs. The sputtered ions are negative, neutral, or positive based on the material of the cathode. The sputtered positive ions pick up electrons from the condensed layer of Cs, allowing for the production of a negative ion beam for which the current is a function of the cathode composition, voltage on the cathode, the Cs ion flux, and the cathode temperature controlled by the cooling fluid. An exclusively-designed sealed housing made of metal with O-rings only at the area of the cathode allows the body of the source to stay warm with respect to the cooled cathode. The SNICS II is provided with a valve on the cathode holder assembly, allowing for changing the cathode while keeping the source under vacuum.

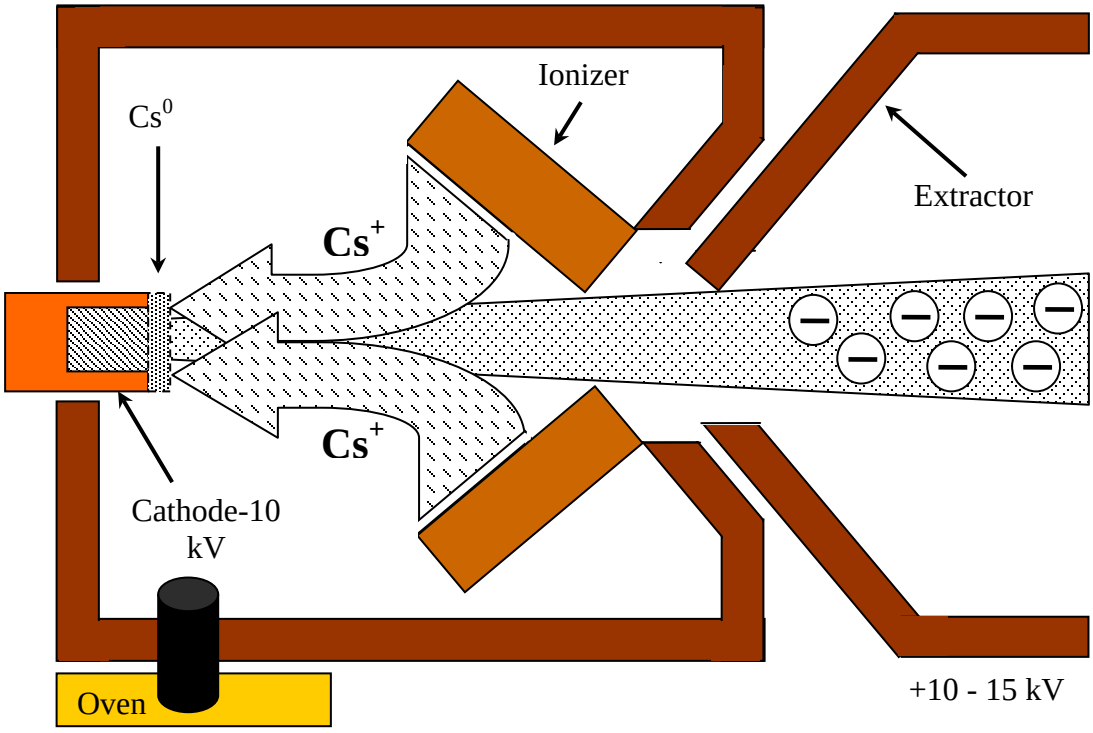

FIG. 4.2. Schematic diagram of SNICS II ion source (top view).

4.4 WMU Van de Graaff Accelerator Facility

A schematic diagram is presented in Fig. 4.3 [181] for the tandem Van de Graaff accelerator at WMU [182]. A 90° analyzing magnet following the accelerator was used to select the desired charge state and energy followed by a carbon-foil post-stripper as a means to produce higher charge states that can not be reached using only the gas stripper (O_2) at the terminal of the accelerator. The beam energy *(q+1)V* emerging from the 90° analyzing magnet (F^{7+}) will be slightly reduced after passing through a post stripper of thicknesses 10.0 ± 1.5 μg/cm^2. The outgoing beam energy was estimated to be reduced by about 0.3% of the incoming beam energy for the same charge state [183,184]. The thickness and density of the stripper foil are the factors governing the reduced amount of beam energy. Since the accelerator at WMU is limited to a maximum terminal high voltage of 6 MV, a beam of F^{9+} was not possible to be directly obtained using only the gas stripper. A beam of F^{7+} instead was extracted from the accelerator using a terminal voltage of 5.25 MV then post-stripped to singly-charged (H-like) and fully-stripped fluorine ions, while some of the incoming He-like ions remain unchanged. A switching magnet then directed the appropriate charge state into the beam line.

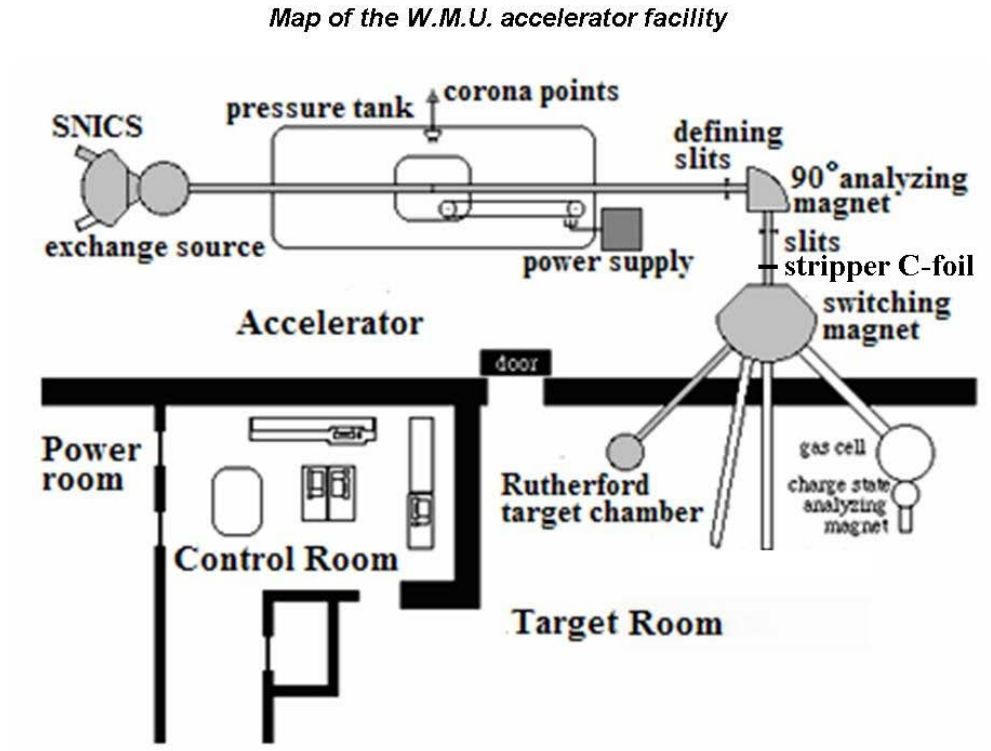

FIG. 4.3. Schematic of the tandem Van de Graaff accelerator facility at WMU (top view) (adapted from Ref. [181]).

4.5 Experiment Setup

Looking downstream, the experiment was set up in the farthest (30°) left beam line as shown in Fig. 4.4. A rotatable holder with space for four aluminum frames was used and target carbon foils of mass areal density 10.9 ± 1.6 μg/cm^2 were mounted on the frames. This setup enabled for an easy optimization of the target position during the experiment. The holder was positioned at 45° to the incoming beam, which corresponds to an atomic target thickness of $(7.7 \pm 1.1) \times 10^{17}$ atom/cm^2 and ensures direct detection of the photons. At such a position, the entire active area of the Si

single crystal is utilized and is not blocked by any part of the aluminum frames on which the carbon foils are mounted. In fact, x-ray attenuation due to absorption does not appreciably occur if the beam passes at 45° inclination through a 10.9 ± 1.6 $\mu g/cm^2$-thick carbon foil based on the calculated attenuation of 0.3–0.1% for the x-ray energy range of 2 – 4 keV, respectively [176].

A ladder of four steps was used to facilitate selecting the desired foil out of the three that were mounted. The fourth frame was left empty so that the background could be determined and to ensure that the emitted x rays originate only from the collisions with the carbon foils and not, for instance, from the aluminum frame or any other impurities that might exist on the frame surface. A 2-mm-wide collimator was used to ensure a good beam collimation at the target as illustrated in Fig. 4.4.

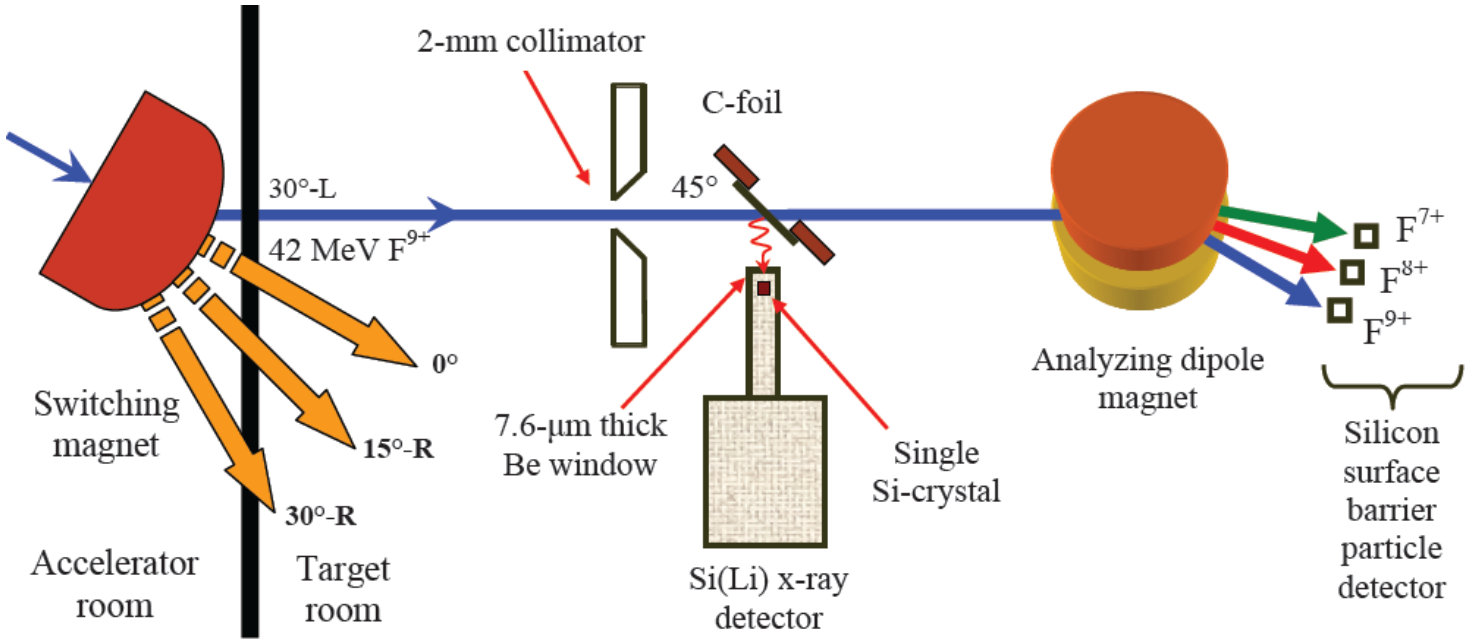

FIG. 4.4. Schematic diagram of the experiment setup in the target room in a top view of random scale (not 1:1).

4.6 Si(Li) X-ray Detector

A Si(Li) detector was used to detect the emitted x rays. The detector had an ultra-thin Be window of thickness 7.6 μm and a single Si(Li) crystal of active diameter, thickness and active area of ≥ 4 mm, 5 mm, and ≥ 12.5 mm^2 [185], respectively. It was mounted perpendicular to the beam line (19.0 ± 0.8 mm from the Si(Li) single crystal and 14.0 ± 0.6 mm from the Be window to the center of the foil mounted at the center of the beam line), giving a detection solid angle of $\Delta\Omega = 0.035 \pm 0.002$ sr. The dimensions given for the Be window and Si crystal correspond to a detection efficiency of 75–100% in the x-ray energy range 1.5–15 keV, respectively, as shown in Fig. 4.5 [185,186]. The Si(Li) detector used had an actual energy resolution (FWHM) of 240 eV at the energy of the characteristic line Mn Kα (~5.9 keV) obtained from a standard ^{55}Fe radioactive source.

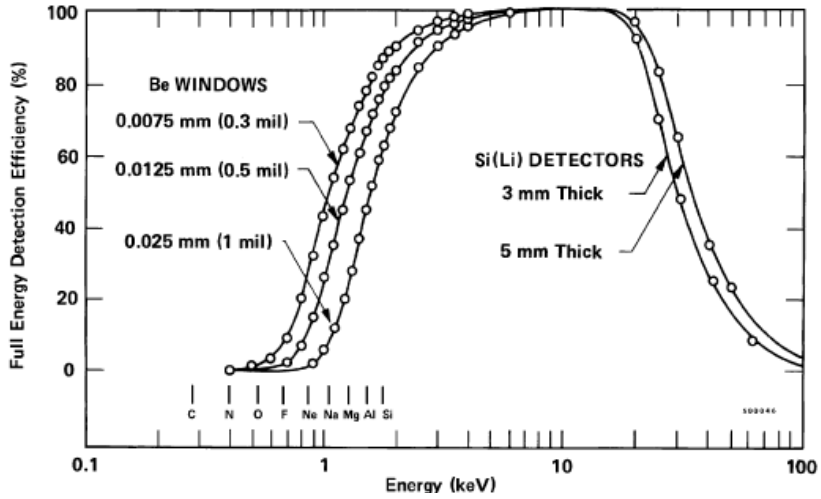

FIG. 4.5. Detection efficiency of SLP Series Si(Li) detector versus Be window thickness in the low-energy range (0.3–10 keV) and versus crystal thickness in the high-energy range (>10 keV) (from Ref. [185]).

4.7 Silicon Surface-Barrier Particle Detector

A dipole analyzing magnet located about 1 m after the target chamber was used to separate the charge states coming out of the collision region. Charge-changed projectile ions with charge states $q-2$, $q-1$ as well as the charge state q of the primary beam were detected individually by three ion-implanted silicon surface-barrier particle detectors [187,188]. The charges $q-2$, $q-1$, and q for the present experiment with incident 2.21 MeV/u F^{9+} ions were registered in the ratios 1.0:18.3:9.2, respectively. Each detector had an active area and active thickness, also called minimum depletion depth, of 300 mm^2 and 100 μm, respectively.

4.8 Data Acquisition System

The data acquisition (DAQ) system provides the required coincidence techniques to isolate the correlated processes. A circuit schematic diagram of the electronics setup is shown in Fig. 4.6. Emitted photons were analyzed in coincidence with ions of outgoing projectile charge states $q-2$, $q-1$, and q using NIM modules and a CAMAC module unless mentioned otherwise.

Signals from the x-ray and particle detectors were amplified by timing filter amplifiers (TFA) and then sent to constant fraction discriminators (CFD) to deliver a logic signal. The output signal from the x-ray detector was also sent to a spectroscopy amplifier so that the voltage signal is amplified from the mV scale to a few-volt scale, providing the correct input for the further modules, i.e., the linear

gate and stretcher (LGS) and single channel analyzer (SCA). A non-gated LGS, called “slow” by convention, was used to register the unconditioned x rays that were not affected by the x-ray TFA.

The x-ray CFD output was split into two signals, one of which was used to gate another LGS, called “fast”, to indicate the recording of only the x rays that started the time-to-amplitude converters (TACs). A TAC records photon-particle coincidences on a timing basis (<2 μs in this case) by starting on a photon as represented by the x-ray CFD output signal, and stopping on a particle event as represented by the output signal of the CFD dedicated to the particle detector. An ORTEC AD811 CAMAC octal analog-to-digital converter (ADC) [189] is then started by the TAC analog output signal for which the amplitude is proportional to the time difference of the properly-delayed signals.

The amplified signal from the spectroscopy amplifier was split into two unipolar outputs and one bipolar output. The two unipolar outputs were used as input signals for the fast (gated) and slow (non-gated) LGSs mentioned above. The ADC was used to deliver the energy (x rays) of both gated and non-gated events as well as time (TAC) spectra of all charge-changed and unchanged projectiles to the computer.

The bipolar output was processed through an SCA followed by a logic converter that split the logic signal produced into two signals. The first was processed through a gate and delay generator (GDG) and used as a strobe to enable the inputs of all TACs and LGSs, while the second was processed through another GDG and split

into two signals. The first signal was sent through one GDG and used as an external strobe pulse to start the conversion by enabling all eight linear gates (inputs) of the ADC, while the second signal was processed through another GDG followed by a level-adaptor (LA8000) and used as a master trigger for the computer. On the other hand, six scalars were used to count the two charge-changed and unchanged projectile ions as well as TFA, SCA and Si(Li) detector counts. A pre-scalar was used with the counter so that the number of incoming counts was reduced by 10 or a multiple of 10.

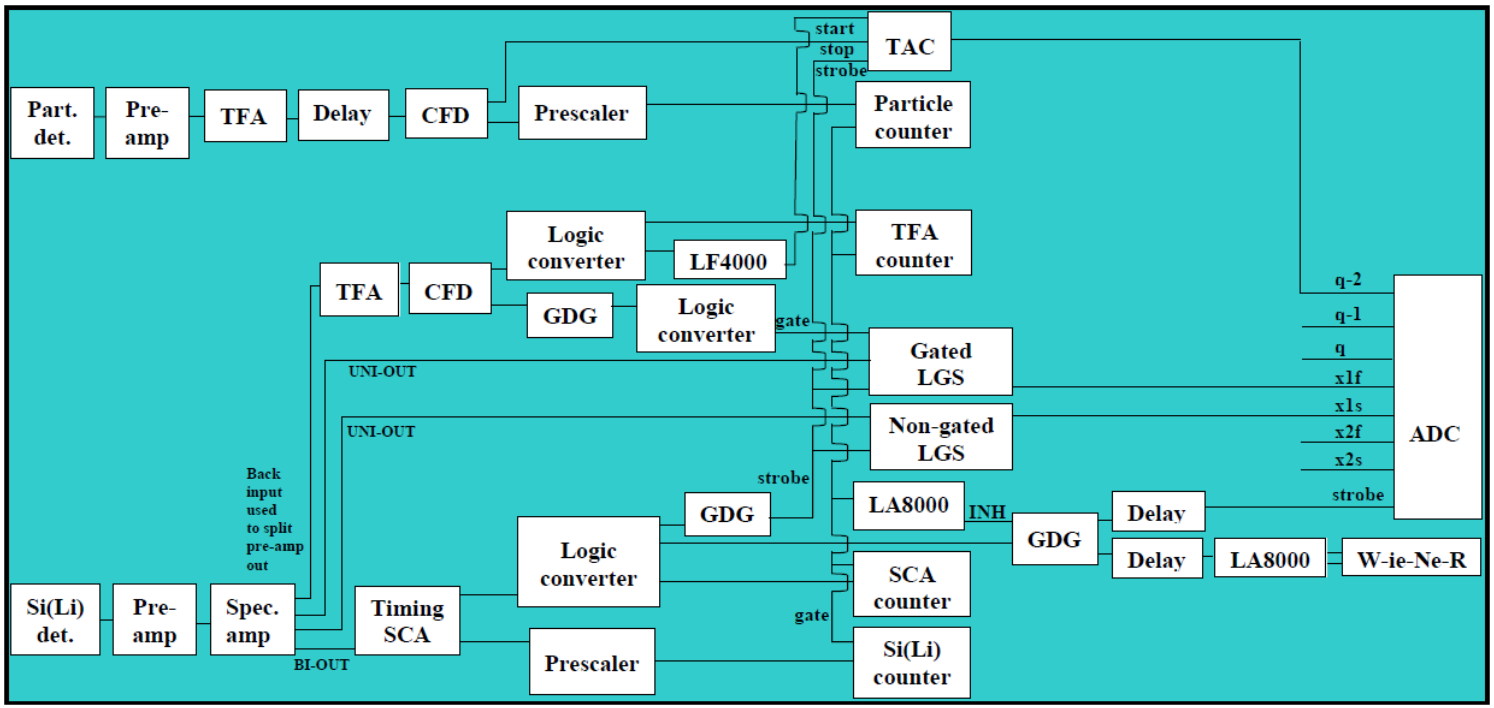

FIG. 4.6. Schematic diagram of the data acquisition system, showing only one particle channel as an example.

4.9 Data Analysis

Two sorts of histograms were created by the computer after receiving the data from the DAQ system, namely, singles (uncorrelated) x-rays and particle histograms in SpecTcl [190,191] event list mode, the powerful data analysis tool developed by the National Superconducting Cyclotron Laboratory (NSCL) at Michigan State University. It is based on an oriented C++ framework and provides various data analysis operations. The SpecTcl-formatted data files were converted into ROOT format so that the ROOT data analysis framework developed by the European Organization for Nuclear Research (CERN) [192] could be utilized to analyze the data. In order to study the correlated processes, x-ray spectra associated with projectile charge changing need to be generated. These could have, and were, also generated with the SpecTcl software for online monitoring of the data.

ROOT was started in the context of the NA49 [193] experiment at CERN and is well-known for being very efficient when handling and analyzing large amounts of raw data. ROOT proved it can efficiently analyze the Large Hadron Collider (LHC) raw data after it was tested with the huge amount of 10 TB of raw data per run of data generated from NA49, which is the same as the rates expected to be delivered by the LHC experiments at CERN. ROOT as an open source can be easily linked to external libraries, which makes it a leading platform on which simulation, data acquisition, and data analysis systems can be established in a C++ environment.

The spectra delivered from the ADC to the computer were converted to a format so that the required environment could be used in the ROOT software. A C++ analysis code was written to apply the conditions of coincidences so that histograms of particle-gated x rays could be generated. This can be established by setting a condition on the particle histogram in the form of a gate of interval length (=a) around the spectrum peak as shown in Fig. 4.7 to be applied on the total collected x rays (gated x rays). The average background was subtracted by setting another window of length (=b) over a wide range and away from the time peak and then dividing the number of background counts obtained in correspondence of the interval length (=b) by a factor (=b/a) to give the background counts corresponding to the same length (=a) of the window around the spectrum peak. This background time window is taken in the same spectrum below or above the time peak.

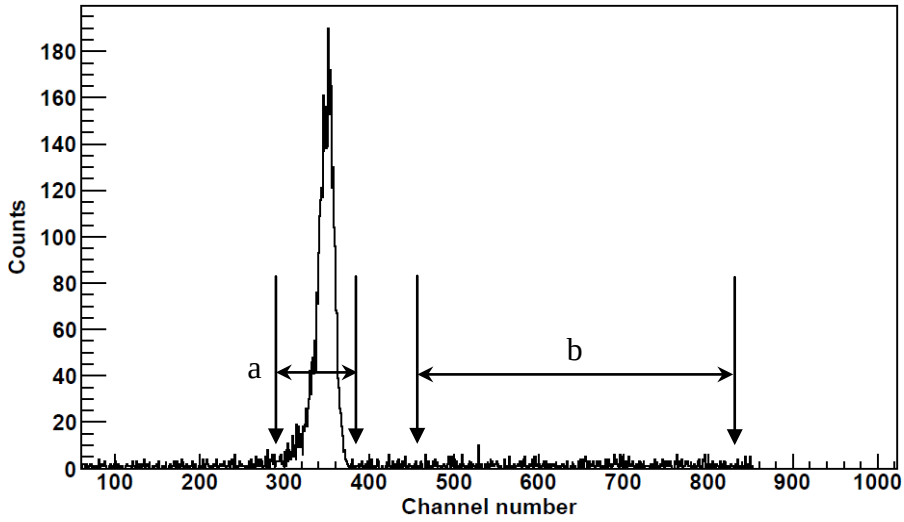

FIG. 4.7. $q-2$ particle spectrum delivered from TAC to ADC with 2 ns per channel and FWHM of the time peak of ~45 ns.

Particle-gated x-ray histograms are then generated by applying the former condition on the raw x rays and subtracting the particle-gated x rays associated with the background as indicated in Fig. 4.8.

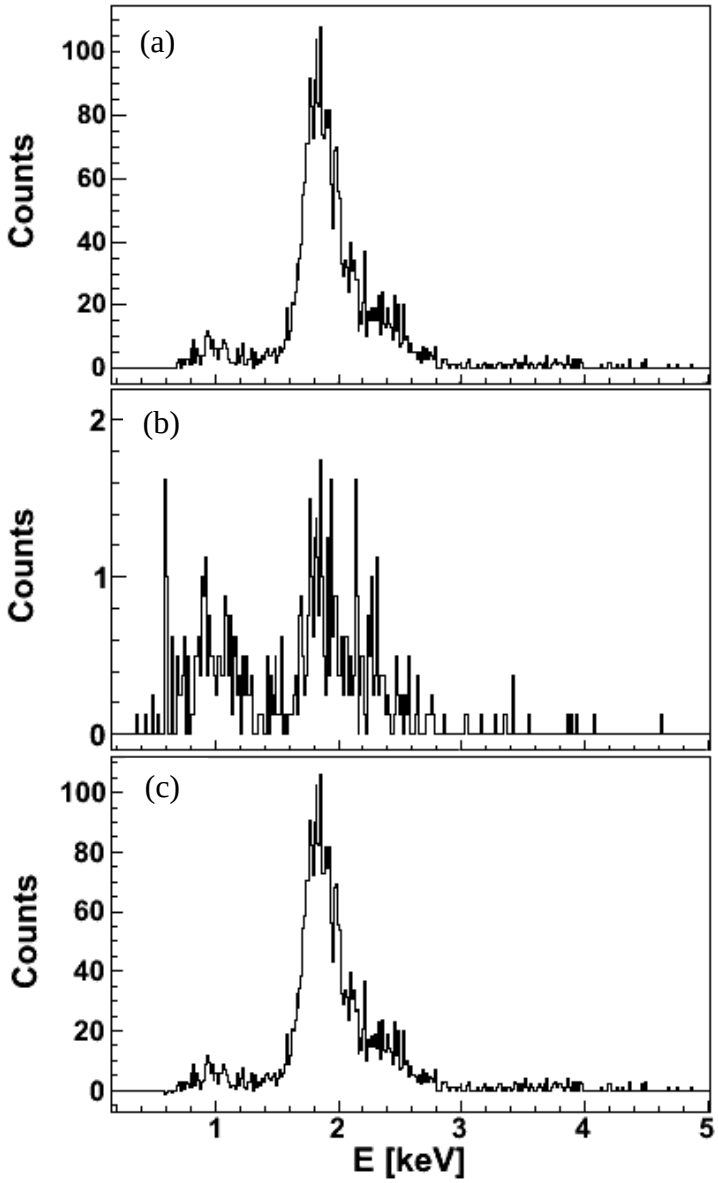

FIG. 4.8. $q-2$ particle-gated x rays: (a) with random events not subtracted, (b) associated with random events, (c) with random events subtracted.

CHAPTER V

DATA ANALYSIS AND DISCUSSION

The main goal of the current work was to investigate REC and RDEC during collisions of fully-stripped fluorine ions at 2.21 MeV/u with a thin carbon foil and to compare the results to the recent experimental [54] and theoretical studies [12,45,49,50]. The projectile and beam energy for this work were selected based on the theoretical calculations to give the best conditions for observation of RDEC [47,48,49], which indicated that low-energy collisions and mid-*Z* projectiles would be a good choice. The range $2 \le Z_p \le 35$ was suggested by Mikhailov [48], while the range $15 \le Z_p \le 35$ was recommended by Nefiodov [49]. This was based on the solid light targets recommended in a theoretical approach for fast collisions [45] and for slow collisions in another theoretical study [48]. The light solid targets were suggested for RDEC experiments as a means of enhancement of the cross section for electron capture from the solid valence band. A significant contribution to the total RDEC cross section is thought to be obtained when the target electrons are captured to the projectile metastable state ($1s^1 2s^1$).

In the current work, x rays associated with projectile charge-changing to single and double electron capture and no charge change by F^{9+} ions were observed and compared with recent work for O^{8+} [54] ions and with theory [12,45,47,49,50].

A thin carbon foil target of mass areal density 10.9 ± 1.6 μg/cm^2, corresponding to the atomic target thickness of $(7.7 \pm 1.1) \times 10^{17}$ atom/cm^2 when the holder was positioned at 45° to the beam line, was used during this experiment.

5.1 Singles Measurements of X-ray Emission versus PIXE Analysis

Proton-induced x-ray emission (PIXE) analysis of the target carbon foil was conducted with 3 MeV protons to determine the contribution of x rays from impurities in the foil to x rays in the expected energy ranges as indicated in Fig. 5.1 for K-REC (1.8–2.5 keV), KL-RDEC (2.9–3.9 keV), and KK-RDEC (3.9–4.7 keV). During PIXE atomic states of the target atoms are excited by the incident protons and then de-excited with the emission of characteristic x rays. Percentage of the contaminations in the target can be estimated based on the intensities of the lines.

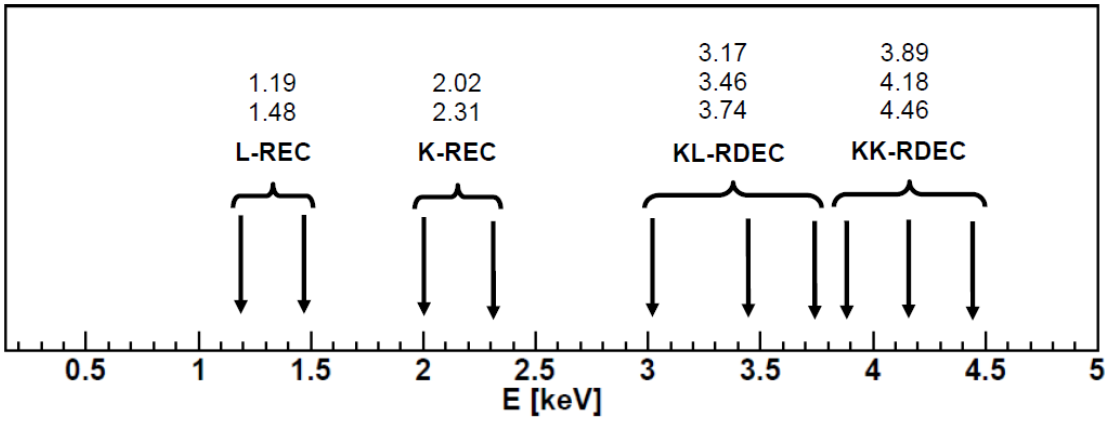

FIG. 5.1. Expected (calculated) REC and RDEC lines for 2.21 MeV/u F^{9+} on a C foil. All the individual energies indicated in the figure are given in keV.

As seen in Fig. 5.2, the PIXE results (in red) are compared with the spectrum of singles x rays (in black) obtained for F^{9+} + C collisions. According to the PIXE

analysis of the target carbon foil as shown in the figure, evidence that the foil has contaminations from Si, S, K, and Ca was seen.

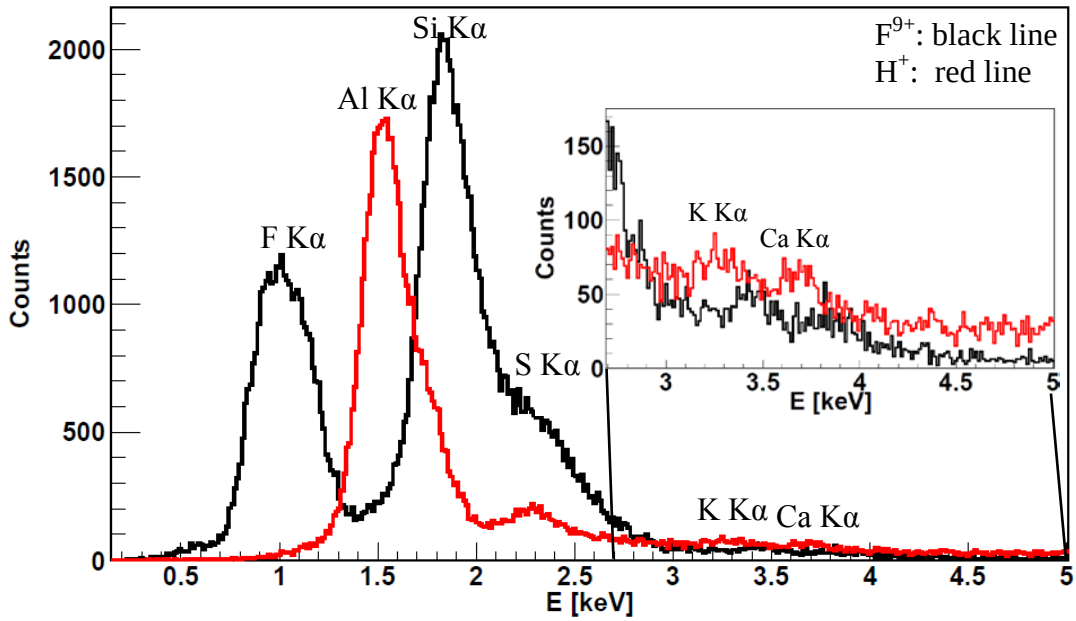

FIG. 5.2. Measurements for singles x rays (in black) for 2.21 MeV/u F^{9+} superimposed on PIXE (in red) using a 3 MeV protons, both on the same C foil.

The Al Kα line was measured only in the case of PIXE, which may be caused by the larger scattering of the protons than the F^{9+} ions. This happens if the protons hit the aluminum frame on which the target carbon foil is mounted as a result of touching the edge of the aperture set prior to the foil. The larger scattering of protons compared to the F^{9+} scattering can be found from the principles of Rutherford scattering assuming that the two ions (H^+, F^{9+}) have the same impact parameter *b*, which is given in terms of Coulomb constant k_e, the projectile kinetic energy K_p and the projectile scattering angle θ_p by

$$b = \frac{Z_p Z_t e^2}{4\pi\varepsilon_\circ M_p \upsilon_p^2} \cot\left(\frac{\theta_p}{2}\right) = \frac{1}{2}\frac{Z_p Z_t e^2}{k_e K_p} \cot\left(\frac{\theta_p}{2}\right), \tag{5.1}$$

from which the projectile scattering angle θ_p can be obtained and given by

$$\theta_p = 2\tan^{-1}\left(\frac{Z_p Z_t e^2}{4\pi\varepsilon_\circ M_p \upsilon_p^2 b}\right) = 2\tan^{-1}\left(\frac{1}{2}\frac{Z_p Z_t e^2}{k_e K_p b}\right), \tag{5.2}$$

For 3 MeV protons and 42 MeV F^{9+}, Eq. (5.2) leads to

$$R_{H/F} = \frac{\tan\left(\theta_{H^+}/2\right)}{\tan\left(\theta_{F^{9+}}/2\right)} = \frac{Z_H K_F}{Z_F K_H} = 1.56, \tag{5.3}$$

which in turn indicates a larger scattering angle for protons than for the F^{9+} ions. The scattering angle for protons to hit the aluminum frame can be calculated from the geometry of the aperture relative to the Al frame of the foil assuming the least scattering when the protons hit the barrier between the carbon foil and its frame. For a 2-mm wide aperture 7.5 cm from the foil center that is mounted on a frame of diameter 1 cm set at an inclination of 45°, this gives an estimate for the scattering angle of protons of about 2.7°. The corresponding scattering angle of the fluorine ions was found accordingly by means of Eq. (5.3) to be about 1.7° as shown in Fig. 5.3. Inaccurate alignment or steering of the produced beam might be also an origin of emission of the Al Kα line during PIXE. The scattering differential cross section can be found accordingly by means of

$$\frac{d\sigma}{d\Omega} = \left(\frac{Z_p Z_t e^2}{8\pi\varepsilon_\circ M_p \upsilon_p^2}\right)\csc^4\left(\frac{\theta_p}{2}\right) = \left(\frac{Z_p Z_t e^2}{4k_e K_p}\right)^2 \csc^4\left(\frac{\theta_p}{2}\right). \tag{5.4}$$

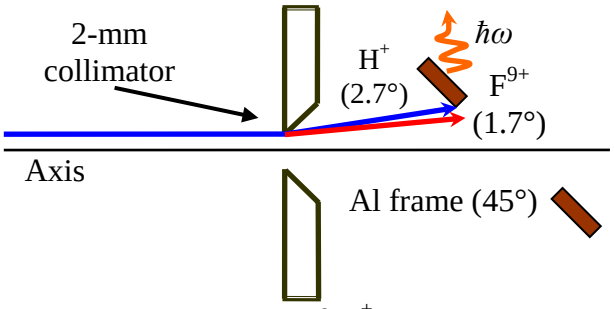

FIG. 5.3. Drawing showing the scattering of H^+ at 2.7° (in blue) and F^{9+} at 1.7° (in red) ions upon hitting the aperture prior to the Al frame. The protons are assumed to have the least scattering when they hit the edge of the Al frame.

The ^{55}Fe standard radioactive source and PIXE analysis were used to produce a 5-point photon energy-calibration curve based on the characteristic lines Al Kα, K Kα, Ca Kα, Mn Kα, and Mn Kβ for which the error in channel number is about 0.5, 1.0, 1.5, 2.5, and 3.0 channels, respectively. The calibration curve is given in Fig. 5.4.

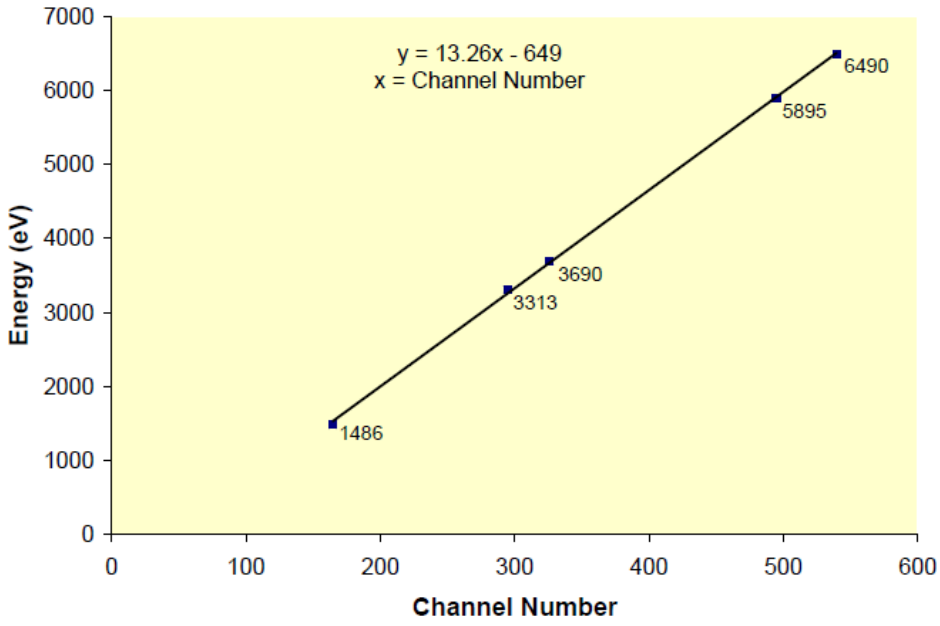

FIG. 5.4. Photon energy-calibration curve based on the characteristic lines Al Kα, K Kα, Ca Kα, Mn Kα, and Mn Kβ. The energies as well as the line equation are given on the graph in eV, where x denotes the channel number.

The characteristic Kα lines of all contaminations come at lower energies in the case of PIXE than in case of the F^{9+} beam. In the case of F^{9+} beam, but not for PIXE, characteristic lines due to heavier contaminations, such as K and Ca, were found to be shifted to higher energies than the lighter ones, such as Si and S. The shift has found to be in the range of 15–25 eV per L-shell vacancy for the lines Si Kα up to Ca Kα [194,195]. This is attributed mainly to single ionization in the case of PIXE versus multiple ionization in the case of multi-charged ions, such as F^{9+}. The multiple ionization has been shown for oxygen ions with beam energies close to that used in the current experiment [194,195].

Calculated energies with uncertainties of REC, RDEC, and discrete characteristic x-ray emission lines are listed in Table 5.1 for the current experiment. The highest uncertainty was found to be for the beam energy based on device (accelerator machine) error (0.5%) and estimation error of the kinetic energy reduction due to the foil stripper (0.3%), while the uncertainty in the characteristic lines and the binding energy is obtained from literature [196,197].

TABLE 5.1. Calculated energies given in ascending order of all x-ray emission lines for 2.21 MeV/u F^{9+} + C in the range of interest (up to 5 keV) as well as the ^{55}Fe lines.

X-ray emission line	Energy (eV)
F^{8+} Kα	826 ± 1
L-REC of K-shell electron	1195 ± 10
L-REC of valance electron	1479 ± 12
Al $K\alpha_{1,2}$ (weighted average)	1486 ± 1
Si $K\alpha_{1,2}$ (weighted average)	1739 ± 1
K-REC of K-shell electron	2018 ± 16
K-REC of valence electron	2306 ± 18
S $K\alpha_{1,2}$ (weighted average)	2307 ± 1
KL-RDEC of two K-shell electrons	3172 ± 25
K $K\alpha_{1,2}$ (weighted average)	3313 ± 3
KL-RDEC of one valence and one K-shell electrons	3456 ± 28
Ca $K\alpha_{1,2}$ (weighted average)	3690 ± 4
KL-RDEC of two valence electrons	3740 ± 30
KK-RDEC of two K-shell electrons	3893 ± 31
KK-RDEC of one valence and one K-shell electrons	4177 ± 33
KK-RDEC of two valence electrons	4461 ± 36
Mn $K\alpha_{1,2}$ (weighted average)	5895 ± 11
Mn $K\beta_{1,3}$ (weighted average)	6490 ± 12

5.2 Generating X-ray Spectra Associated with Projectile Charge-changing

For the F^{9+} beam incident on the carbon foil, data were obtained for x rays associated with double capture (F^{7+}), with single capture (F^{8+}), and with no capture (F^{9+}) as shown in Fig. 5.5(a,b,c), respectively. In all cases, the small contribution from random x rays was subtracted from each of the spectra shown, according to the procedure described in Sec. 4.9. The F Kα line has been observed in the spectrum of

x rays associated with single capture (F^{8+}), while almost no evidence was seen for this line in the spectra for x rays associated with double capture and no capture. This provides evidence that there is essentially no crossover of x rays from the F Kα line among the various spectra. However, there is expected to be some crossover for K-REC, primarily to F^{9+}, which involves simultaneous ionization and x-ray emission. This occurs when a target electron is captured to the projectile K-shell then promptly ionized for which the probability one order of magnitude less than the probability of L-shell ionization [96,97]. Target x rays, such as the characteristic lines from the contaminations, appear in all of the spectra as it is expected to have target x rays associated with no capture by the projectile as well as with single and double electron capture. The Si Kα and S Kα lines overlap partially with the lower energy side of the K-REC structure as can be inferred from Table 5.1 and Fig. 5.5(b) in the x rays associated with single capture. Evidence for RDEC is seen in the x rays associated with double capture in Fig. 5.5(a) although the spectrum overlaps partially with the K Kα and Ca Kα lines as seen in Fig. 5.5(b).

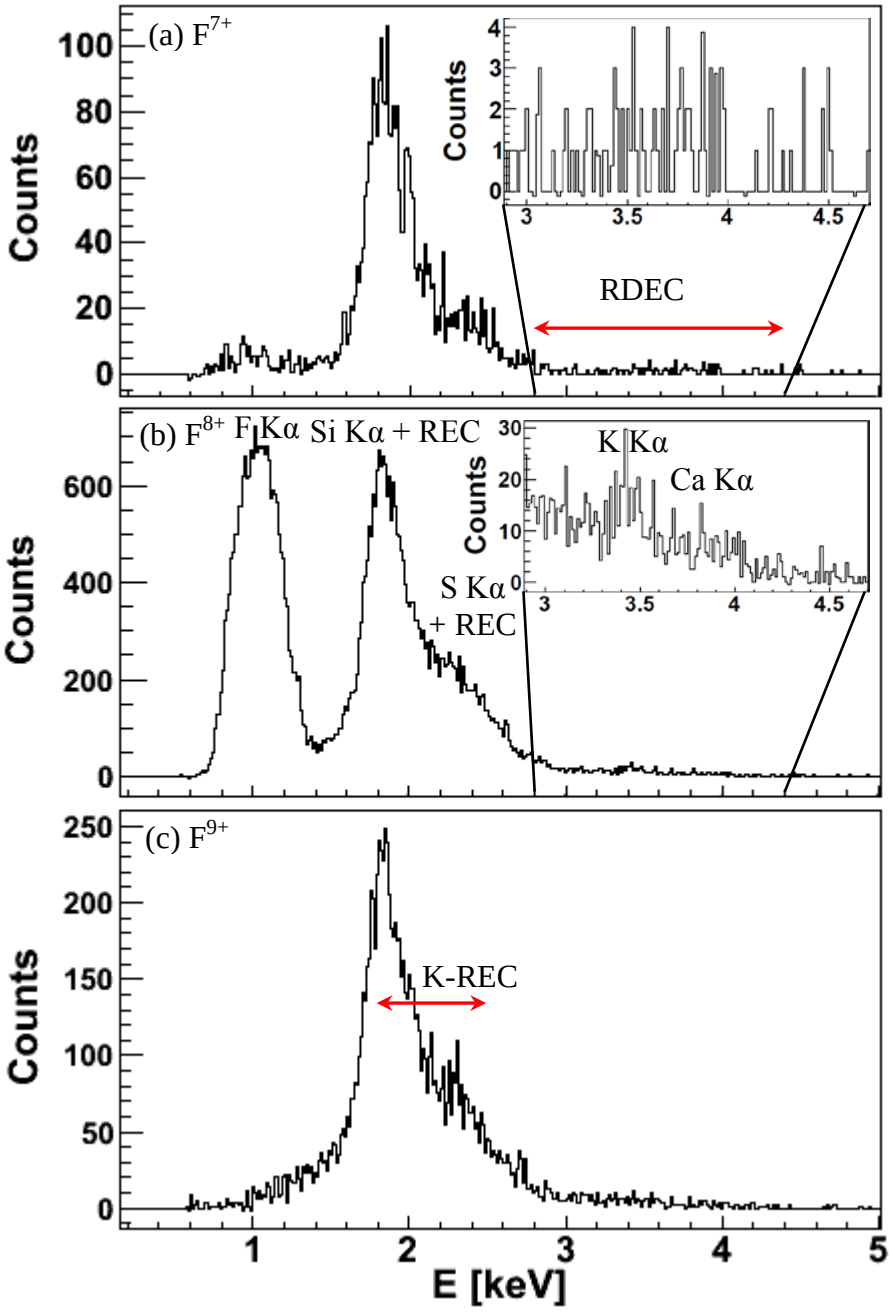

FIG. 5.5. X rays associated with charge change and no charge change with random backgrounds subtracted for 2.21 MeV/u F^{9+} + C collisions: (a) for F^{7+} (double capture), (b) for F^{8+} (single capture), (c) for F^{9+} (no capture).

5.3 REC Analysis

The contamination lines observed by means of PIXE analysis in the REC energy range (Si Kα and S Kα) were found to be distributed between the double, single, and no capture channels. The contamination line is observed when a k-shell electron is captured by the projectile from the contaminating atom, leaving a K-vacancy that can be filled by an L-shell electron, causing the emission of Kα line. This mechanism can be associated with single, double or no capture by the projectile with different probabilities depending on the collision energy and the atomic number of the contamination, i.e., the binding energy of the K-shell electron within the contamination atom. The peak at REC energy domain in the spectrum for x rays associated with double capture (F^{7+}) is mostly (78%) due to contamination with the complement dedicated to REC counts when they are accompanied with the nonradiative electron capture (NRC). This conclusion is based on the calculated total K-REC cross section obtained from the Bethe-Salpeter formula [67] and a percentage of 5.2% of the total REC counts crossing over to the double capture channel due to NRC accompanying REC as discussed below in detail. Hence, the spectrum for x rays associated with single capture (F^{8+}) can be corrected for contamination in the region of REC if the F^{7+} spectrum is superimposed on the F^{8+} spectrum and normalized to it at the position of the Si Kα line as shown in Fig. 5.6(a). Owing to Table 5.1, the normalization was made at the Si Kα line based on this peak partially overlapping with the REC energy domain in the single capture channel at the low-energy tail of

the K-REC peak, while the S Kα line almost coincides with the K-REC peak due to the capture of a target valence electron. The Bethe-Salpeter formula [67] was used to calculate the correct REC cross section for fluorine to determine how the Si Kα line has to be normalized to the Si Kα line in the single capture channel, so that the counts leftover after subtraction (found to be 8864 counts) of the contribution from the contamination lines (Si Kα and S Kα) give the REC cross section of 525 b/atom. This value is equal to the value obtained from the Bethe-Salpeter formula [67] corrected by a factor of 6, which is the number of target electrons ($N_t = 6$) in the C atom according to Eq. (2.21). Hence, the spectrum for F^{7+} at the position of the Si Kα peak was normalized to the spectrum for F^{8+} in Fig. 5.6(a) and to that for F^{9+} in Fig. 5.6(b) so that the counts leftover after the subtraction of the normalized double-capture (F^{7+}) channel from the single (F^{8+}) and the no capture (F^{9+}) channels are dedicated to REC counts in each channel. The scale of the normalization of the F^{7+} spectrum is determined based on the single capture, no capture, and the double capture fractions of the total charge-changing events, which were found from the measurements to be 61.4%, 33.4%, and 5.2%, respectively, which are deduced based on the ratios 1.0:18.3:9.2 in which the ions F^{7+}, F^{8+}, and F^{9+} were registered, respectively, for the present experiment with incident 2.21 MeV/u F^{9+} ions. This means that the F^{7+} spectrum has to be normalized to the F^{8+} spectrum so that the counts leftover in the F^{8+} spectrum within the K-REC energy domain (1.8–2.5 keV) after the subtraction of the normalized F^{7+} spectrum has to represent 61.4% of the total number of REC

counts (8864) obtained from Bethe-Salpeter [67]. The same approach applies to extract the REC counts associated with the no capture (F^{9+}) channel. After the x rays dedicated to contaminations lines are subtracted, the x rays associated with single capture were added to those associated with no capture. The histogram resulting from this addition was normalized upwards by a factor of 1.055, as shown in Fig. 5.6(c), to include the REC counts existing in the x rays associated with F^{7+} due to NRC accompanying REC as two independent processes. Accordingly, the REC counts were distributed as 5443, 2961, and 460 counts in the single capture, no capture, and double capture channels, respectively, which correspond to 31%, 48%, and 22% of the total x-ray counts over the REC energy domain in each channel, respectively. The complement parts of these percentages can be then attributed to contamination, which is in support of the choice of the double capture to be scaled up and subtracted from the single capture channel for which the x rays over the same range originate partially from REC and primarily from contamination lines as shown in Fig. 5.6(a).

The capture of valence and 1s target electrons was taken into account when K-REC was investigated. The counts leftover are dedicated to K-REC, corresponding to a total cross section σ_{REC}^{1s} of 525 b/atom. The corresponding differential cross section at an observation angle of 90° and a collision energy of 2.21 MeV/u is a factor of $3/8\pi$ of σ_{REC}^{1s} based on Eq. (2.21), which reveals a value of 125 b/sr.atom. The Compton profiles displayed in Fig. 5.6(d) were calculated as functions of photon

energy by employing Eq. (2.7) to show how the overlapped K-REC lines are expected to appear. The expected REC lines are listed in Table 5.1, while the measured REC peaks corresponding to the Bethe-Salpeter [67] value of K-REC total cross section are shown in Fig. 5.6(c) for the sake of comparison with Fig. 5.6(d). The REC line of lower energy is emitted when a K-shell (1s) electron is captured, while the higher-energy line is due to the capture of a valence (L-shell) target electron (2s or 2p), both into the projectile K-shell. The small separation of about 274 eV between the two REC lines is not enough to measure them as two resolved peaks based on an actual energy resolution of 240 eV for the used Si(Li) x-ray detector. The energy separation of 274 eV can be deduced from the two expected REC-line energies given in Table 5.1, which is the difference between binding energy of the captured K-shell electron (288.23 eV) and the average binding energy of the 2s and 2p electrons (16.59, 11.26 eV) according to the National Institute of Standards and Technology (NIST) [196].

It is seen that there is a clear discrepancy between the experimental and calculated structures shown in Fig. 5.6(c,d), respectively, which might be attributed to the lower probability of capturing a target valence (L-shell) electron than that for a K-shell electron, noticing that the structure shown in Fig. 5.6(d) assumes equal probabilities for the two captures. The discrepancy can also be due to the contamination contribution not being subtracted accurately, which apparently led to a deformation of the REC peak shown in Fig. 5.6(c). The main source of the counts of K-REC from K-shell is the spectrum of x rays associated with F^{9+} as seen in

Fig. 5.6(b), while the K-REC of a valence target electron was associated to single and no capture at comparable rates as seen in Fig. 5.6(a,b). However, this discrepancy has no impact on the analysis for the RDEC/REC cross section ratio since the Bethe-Salpeter formula [67] is used as a reliable theory to calculate the K-REC cross section regardless of the corresponding REC structure obtained from experimental data. In Table 5.2, the calculated REC cross sections are presented in comparison with the measured values during all RDEC experiments conducted up to the moment.

TABLE 5.2. Measured versus calculated (from Bethe-Salpeter) total K-REC cross sections for the four conducted RDEC experiments.

Z_p	E_p (MeV/u)	κ	Z_t	σ_{REC}^{1s} (b/atom)	
				B-S [67]	Exp
18 [51]	11.4	0.84	6	360	685 ± 40
92 [52]	297	0.84	18	1080	---
8 [54]	2.38	0.82	6	331	432
9 [61]	2.21	0.96	6	525	---

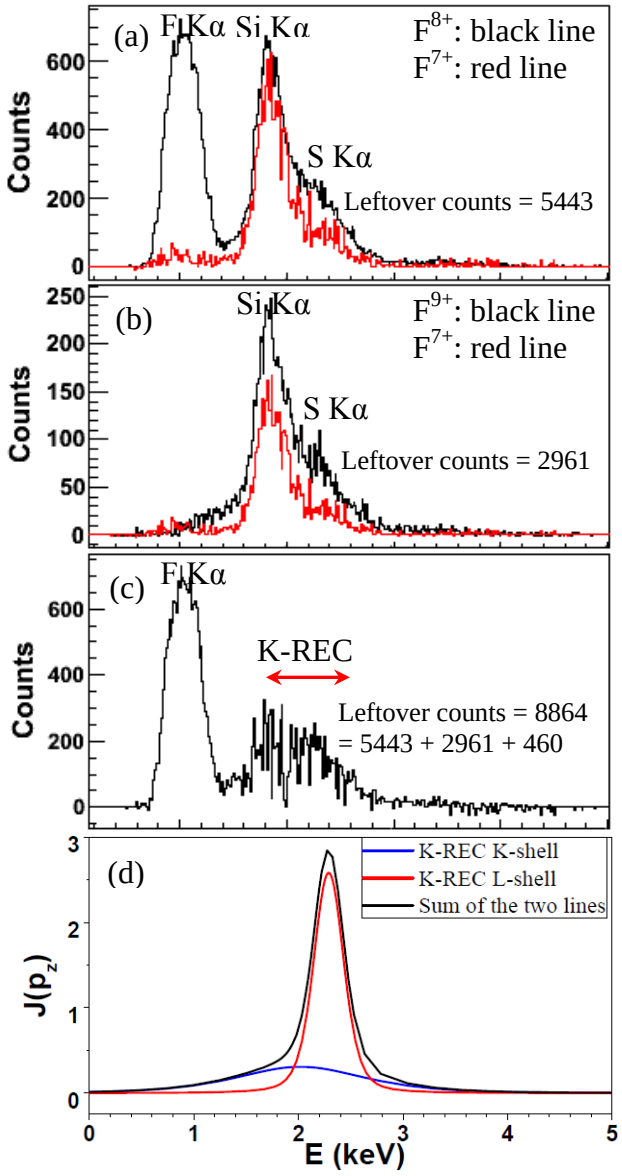

FIG. 5.6. X rays associated with charge change for 2.21 MeV/u F^{9+} + C collisions: (a) for F^{8+} with the spectrum of x rays associated with F^{7+} normalized and superimposed on it, (b) for F^{9+} with the spectrum of x rays associated with F^{7+} normalized and superimposed on it, (c) for K-REC spectrum as a result of summing up the leftovers from the spectra F^{8+} (61.4%), F^{9+} (33.4%), F^{7+} (5.2%) (not shown), (d) Compton profiles of the two K-shell electrons (blue), the four L-shell electrons (red), and the sum of the two profiles (black), which represents the Compton profile of the C atom. The normalizations in (a) and (b) are made so that the counts leftover after subtracting the normalized F^{7+} represent 61.4% and 33.4%, respectively, of the Bethe-Salpeter [67] value of REC. Small random backgrounds were subtracted from each spectrum and normalizations were made at the position of the Si Kα line.

5.4 RDEC Analysis

To correct the F^{7+} spectrum for contamination in the region of RDEC, the spectrum for x rays associated with single capture (F^{8+}) was superimposed at the position of the K Kα line on the spectrum for x rays associated with double capture as

shown in the left panels of Fig. 5.7 and Fig. 5.8(a). Two well-resolved peaks dedicated to the K Kα and Ca Kα lines are seen in the spectrum of x rays associated with single capture as shown in Fig. 5.5(b), where they are not overlapped with x rays from any other process, except for a negligible pileup contribution from REC photons as indicated in detail in Sec. 5.5. These two peaks overlap with some of the RDEC events within the x rays associated with double capture as shown in Fig. 5.1. Hence, the normalized F^{8+} spectrum is subtracted from the F^{7+} spectrum as shown in the right panels of Fig. 5.7 and Fig. 5.8(b) so that the counts leftover in the double capture channel can be attributed to RDEC.

The contamination lines contribute to the single capture channel if a K-shell electron from a contaminant target atom is captured to the projectile followed by L→K-shell transition within the contamination atom, producing the corresponding characteristic Kα line. Hence, the subtraction is performed based on the assumption that x rays associated with single capture over the RDEC energy domain are predominantly due to contamination lines from K and Ca over the KL-RDEC range where there is no other source of x rays other than contaminations except for the negligible contribution from pileup as indicated in Sec. 5.5. The x rays associated with double capture over the RDEC energy range originate from contamination lines and partially from KL-RDEC. No evidence of contamination lines was seen in the high-energy side of KK-RDEC.

A careful analysis covering the lower limit to the upper limit of the RDEC cross section is shown in Fig. 5.7. The left panels of Fig. 5.7 indicate the x rays associated with F^{7+} (in black) and the x rays associated with F^{8+} normalized and superimposed on the F^{7+} spectrum. The right panels of the same figure show the leftover counts after the subtraction of the normalized F^{8+} from the F^{7+} spectra. The trials shown in Fig. 5.7 show that the best subtraction of contamination lines (K Kα and Ca Kα) from the double capture channel is between the panels (b,b′) and (c,c′), where the normalized x rays associated with F^{8+} and the x rays associated with F^{7+} are of the same level of intensity at the expected photon energies of the contamination lines (K Kα and Ca Kα).

A fitting that gives the average between the best two trials (b,b′) and (c,c′) of Fig. 5.7 is given in Fig. 5.8. This average fitting has a leftover of 33 counts in the energy range 2.9–4.7 keV dedicated to the entire range of RDEC, i.e., KL- and KK-RDEC. As seen in Fig. 5.8, the intensities of contamination lines match between the two x-ray spectra of F^{7+} and F^{8+}.

It has been taken into account that RDEC can occur when two K-shell electrons, two valence electrons, or one K-shell and one valence electron, are captured from the target simultaneously to the projectile bound states ($1s^12s^1$ or $1s^2$). The collected counts of RDEC were separated into two groups as indicated in Figs. 5.7 and 5.8 based on the calculated energies in Table 5.1. The two groups of RDEC counts are KL-RDEC (2.9–3.9 keV), having 15 counts, and KK-RDEC

(3.9–4.7 keV), having 18 counts, when two electrons are captured to the fluorine metastable state ($1s^12s^1$) and the ground state ($1s^2$), respectively. Comparing to theory, the KL-RDEC/KK-RDEC counts ratio is found to be 0.65 and 1.11 in the case of the two panels (b,b′) and (c,c′) of Fig. 5.7, respectively, versus 0.9 from Nefiodov [49], while all other trials were found to be in disagreement with Nefiodov.

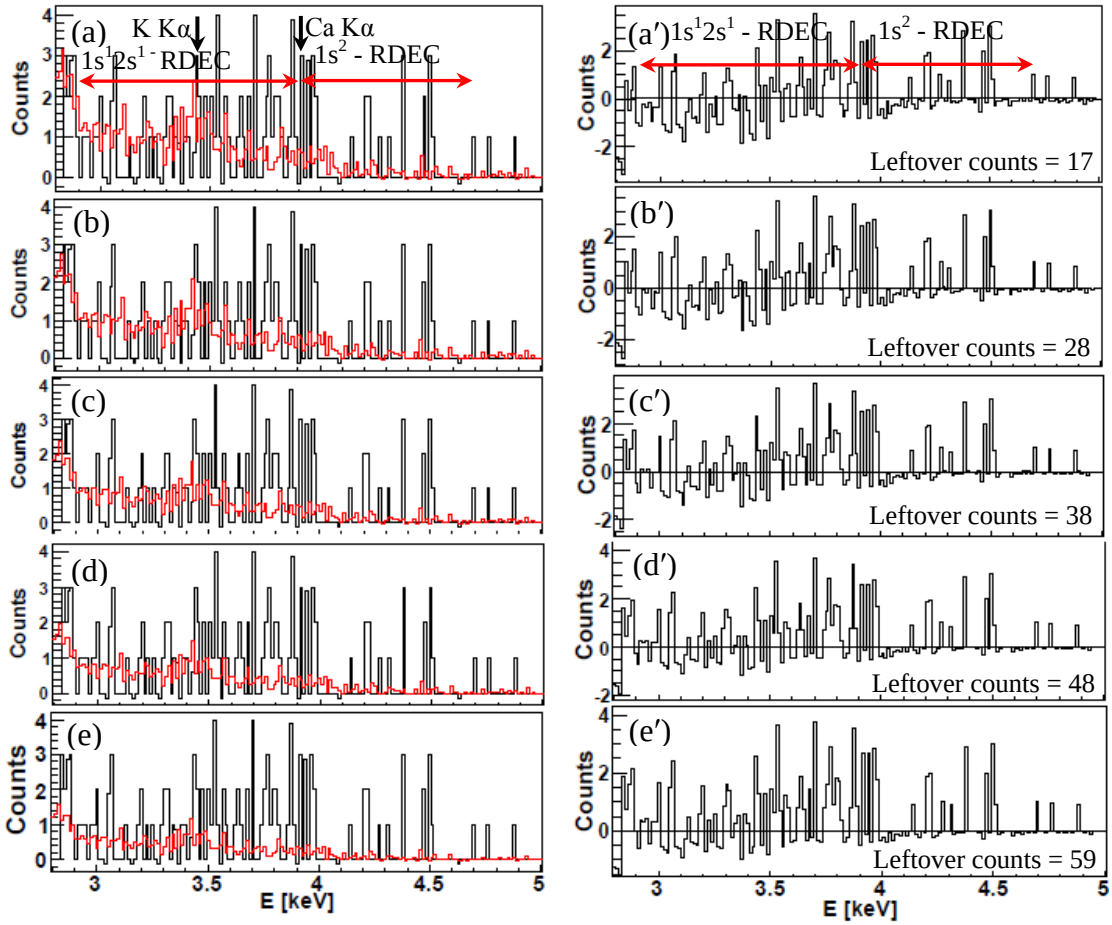

FIG. 5.7. Analysis trials for RDEC showing the normalized spectra of x rays associated with F^{8+} (in red) superimposed on the spectra of x rays associated with F^{7+} (in black) in the left panels. The right panels show the leftover counts after subtraction of the normalized F^{8+} spectra from the F^{7+} spectra. Trials are shown in ascending order from the lower limit of 17 leftover counts after subtraction [panel (a,a′)] to the upper limit of 59 counts [panel (e,e′)].

In Table 5.3, a detailed analysis is given for the distribution of the RDEC counts obtained after the subtraction. In the table, the Nefiodov [49] ratio is calculated for the sake of comparison with theory for each trial.

TABLE 5.3. Distribution of RDEC counts based on the trials given in Fig. 5.7.

Panel	N_{RDEC}	$N_{KL\text{-}RDEC}$	$N_{KK\text{-}RDEC}$	Counts ratio (KL/KK)	Corresponding Nefiodov ratio
(a,a′)	17	1	16	0.06	
(b,b′)	28	11	17	0.65	
(c,c′)	38	20	18	1.11	0.9
(d,d′)	48	29	19	1.53	
(e,e′)	59	37	22	1.68	

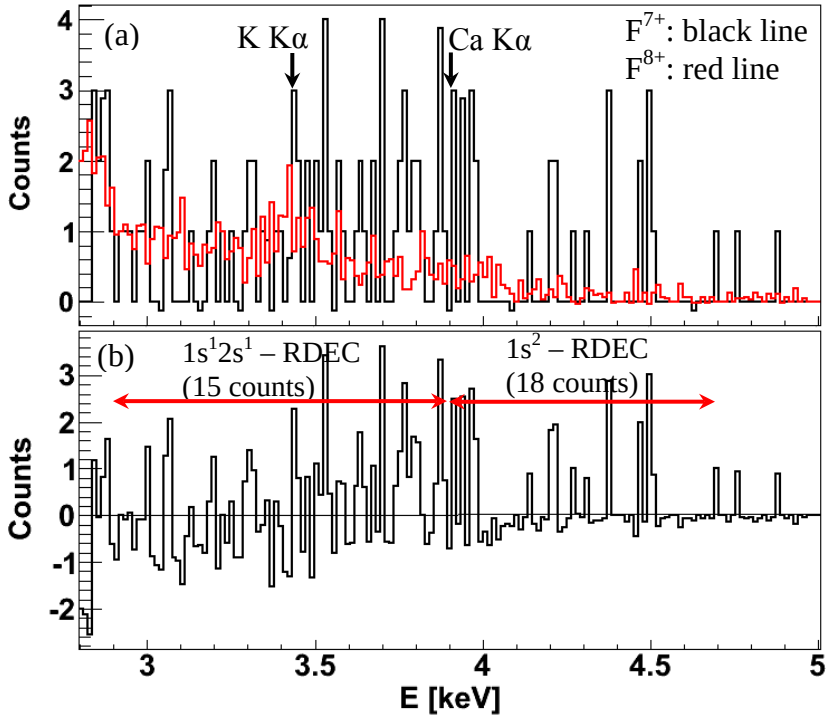

FIG. 5.8. Fitting to give the average between the best two trials (b, b′) and (c, c′) of Fig. 5.7 showing x rays associated with charge change for 2.21 MeV/u F^{9+} + C collisions with random backgrounds subtracted: (a) for F^{7+} (double capture) with the spectrum of x rays associated with F^{8+} (single capture) normalized to it at the position of the K Kα line and superimposed on it, (b) for F^{7+} with normalized x rays associated with F^{8+} subtracted.

5.5 Analysis for Background Processes

In ion-atom collisions, several background processes are likely to contribute to the singles x rays and may overlap with the desired x rays due to REC and RDEC. In the current analysis, the most significant background processes as possible mechanisms of x-ray emission are considered [62] to be radiative electron capture to continuum (RECC), secondary electron bremsstrahlung (SEB), the two-step process of independent double radiative electron capture (DREC), as well as REC combined with nonradiative electron capture (NRC).

The current experiment was conducted with a beam of bare fluorine at a collision energy of 2.21 MeV/u on a thin carbon foil, corresponding to an energy of 1204 eV for a captured target valence electron in the projectile frame. The maximum photon energy emitted due to QFEB is T_r given by Eq. (3.6), which is the kinetic energy of the captured target electron in the projectile frame, while SEB is characterized by a range of photon energies up to T_m owing to Eq. (3.12), which is the maximum energy transferred from the projectile to a free electron at rest. The two characterizing energies T_r and T_m are found to be 1.2 and 4.8 keV, respectively [62]. The REC and RDEC energy ranges are calculated to be 1.8–2.5 and 2.9–4.7 keV, respectively, which do not overlap with QFEB ($\leq$1.2 keV), while SEB was found to be of negligible contribution to x rays [138,139] in the energy range $T_r < \hbar\omega < T_m$ for low-Z targets such as the C target used in the current work., i.e., 1.2–4.8 keV.

In the case of high-beam intensities, the rate of the collisions increases, allowing for an increase in the pileup probability, i.e., the probability to have two ions emitting REC photons and detected as a single photon of double energy in the single capture channel. The rate of photons detected for the current measurements was found to be 4 counts/s as a result of the low beam intensity used of <1 pA. Based on the total REC cross section and the target thickness values of 525 b/atom and $(7.7 \pm 1.1) \times 10^{17}$ atom/cm^2, respectively, the probability of pileup from REC photons was found to be 1.3×10^{-12} [62]. Comparing this result to the K-REC probability of 4.1×10^{-4}, this implies a negligible loss of REC photons due to pileup.

As discussed in Sec 3.2 and Ref [62], it is possible that REC counts appear in the spectrum of x rays associated with double capture if two target electrons are captured independently to the same projectile, one radiatively (REC) and the other nonradiatively (NRC). The probability of having NRC and REC accompanying each other was found to be 2.1×10^{-5} based on a K-REC probability of 4.1×10^{-4} and under the experimental conditions of the current work, which caused 5.2% of the total REC counts to be associated with double capture [84].

As discussed in Sec. 3.3 and Ref. [62], DREC contributes at the energy region of REC in the spectrum of x rays associated with double capture (F^{7+}) when two independent REC photons are emitted due to the separate capture of two target electrons by the same projectile. Making use of Eq. (3.29), where σ_{REC} is the total K-REC cross section calculated from Bethe-Salpeter [67], the KK-DREC cross

section is found to be 0.0031 b/atom, which corresponds to a probability of 2.4×10^{-9} compared to three and six orders of magnitude higher values for the calculated K-REC and the measured KK-RDEC total cross sections, respectively [61]. Thus, this represents a negligible contribution of DREC to REC as well as RDEC energy ranges in the F^{7+} channel.

5.6 RDEC Cross Sections

5.6.1 Total RDEC Cross Sections

The x-rays counts registered from the gated LGS were found to be 2.3 times greater than those obtained by summing up all the coincidence spectra within the RDEC energy range, meaning that about 57% of the x-ray counts were lost and thus those coincidences are never seen. Based also on the negligible contribution of DREC to the RDEC energy domain, the measured differential KL-RDEC and KK-RDEC cross sections for the current system of collision (2.21 MeV/u F^{9+} + C) were found to be 0.20 ± 0.12 and 0.23 ± 0.14 b/sr.atom, respectively, for a net differential RDEC cross section of 0.43 ± 0.26 b/sr.atom. The corresponding total RDEC cross sections $\sigma_{RDEC}^{1s^1 2s^1}$, $\sigma_{RDEC}^{1s^2}$, and σ_{RDEC} are 1.6 ± 1.0, 1.9 ± 1.2, and 3.6 ± 2.1 b/atom, respectively. For the sake of comparison with the collision system 2.38 MeV/u O^{8+} + C [54], the total RDEC cross sections measured for this system were found to be 2.3 ± 1.3, 3.2 ± 1.9, and 5.5 ± 3.2 b/atom for $\sigma_{RDEC}^{1s^1 2s^1}$, $\sigma_{RDEC}^{1s^2}$, and σ_{RDEC}, respectively, which are in excellent compatibility with the F^{9+} results. The total KK-RDEC cross section

calculated by Chernovskaya [50] by means of the first approximation $\left(\sigma_{RDEC,A}\right)$, where the electrons are assumed to be distributed homogeneously in the whole volume of the atom, was found to be closest (0.9 b/atom) to the corresponding measured value (1.9 b/atom), while the prediction of Yakhontov [45] (0.12 b/atom) is the worst. Thus, the approaches of Chernovskaya [50] and Yakhontov [45] gave underestimates of the KK-RDEC cross section by 2.1 and 16.1 times, respectively.

The probabilities and corresponding cross sections of all the processes of interest as well of the background processes are listed in Table 5.4, while all the total KL-RDEC and KK-RDEC cross sections calculated from the available theories up to the moment are presented in Table 5.5 in comparison with the measured values or upper limits from all the experiments performed till today [62].

TABLE 5.4. Cross sections and the corresponding probabilities in descending order for REC, RDEC, and the other background processes for 2.21 MeV/u F^{9+} + C.

Atomic process	Measured vs. calculated	Energy domain (keV)	Cross section (b/atom)	Probability
K-REC ($1s^1$)	calculated	1.8–2.5	525	4.1×10^{-4}
K-NRC/K-REC ($1s^2$)	calculated	1.8–2.5	27	2.1×10^{-5}
Total RDEC ($1s^2 + 1s^12s^1$)	measured	2.9–4.7	3.6 ± 2.1	$(2.8 \pm 1.7)\times10^{-6}$
KK-RDEC ($1s^2$)	measured	3.9–4.7	1.9 ± 1.2	$(1.5 \pm 0.9)\times10^{-6}$
KL-RDEC ($1s^12s^1$)	measured	2.9–3.9	1.6 ± 1.0	$(1.3 \pm 0.8)\times10^{-6}$
KK-DREC ($1s^2$)	calculated	1.8–2.5	0.0031	2.4×10^{-9}
Pileup (two REC photons)	calculated	3.6–5.0	1.7×10^{-6}	1.3×10^{-12}

5.6.2 The Ratio $R = \sigma_{RDEC}^{1s^2} / \sigma_{REC}^{1s}$

The KK-RDEC/K-REC cross section ratio $R = \sigma_{RDEC}^{1s^2} / \sigma_{REC}^{1s}$ is found to be 0.0037 ± 0.0022, which is a factor of 2.0 smaller than the measured value in the case of the O^{8+} experiment and factors of 7.4, 20.6, and 32.2 greater than the values calculated from Mikhailov [47], the principle of detailed balance [12], and Yakhontov [45], as given by Eqs. (2.36), (2.37), and (2.41), respectively. The comparison with the measured O^{8+} result of *R* [54] shows good consistency, while the Mikhailov prediction [47] is in fair agreement with the measured value and Yakhontov [45] is about 3 times worse. The underestimation of the value given by Mikhailov of 7.6 times is attributed to the assumption in Eq. (2.41) of the capture of only the K-shell electrons. However, adding the contribution of the KK-RDEC cross section due to the capture of two valence target electrons (0.19 mb/atom) to the value of the KK-RDEC cross section due to the capture of two K-shell electrons (221 mb/atom) does not improve the ratio *R*, which implies a disagreement of Eq. (2.42) with the current measurements. The slight difference between the κ values of the two compared systems was an origin of the disagreement of the Yakhontov prediction [45], where Eq. (2.37) was used to calculate R^{F} based on $R^{Ar} = 3.6 \times 10^{-6}$. This equation has a restriction that the two compared systems must have similar or very close Sommerfeld parameters. The system to which this work is compared has a κ value of 0.84 versus 0.96 for this work. All the cross-section ratios of KK-RDEC/K-REC are

introduced in Table 5.6 for the available theories compared to all the RDEC experiments performed up to the moment.

5.6.3 The Ratio $R' = \sigma_{RDEC}^{1s^1 2s^1} / \sigma_{REC}^{1s}$

The measured value for this work was found to be a factor of 1.7 smaller than the value measured in the case of O^{8+} experiment [54]. The factor between the two values is reasonable taking into account that the two projectiles have two successive atomic numbers. The only theory that introduced a prediction for the KL-RDEC/K-REC cross section ratio is given by Nefiodov [49], which underestimated the measured KL-RDEC cross section by a value that is more than 22 times lower according to Eq. (2.45) with the aid of the right panel of Fig. 2.11. The poor statistics due to the low count rate of the RDEC measurement and considering only the capture of tightly-bound (K-shell) target electrons could be the origins of the discrepancy. All the cross-section ratios of KL-RDEC/K-REC are given in Table 5.6 for the available theories compared to all the RDEC experiments performed up to the moment.

5.6.4 The Ratio $R'' = \sigma_{RDEC}^{1s^1 2s^1} / \sigma_{RDEC}^{1s^2}$

The ratio of the cross sections for KL-RDEC/KK-RDEC is found to be 0.83 ± 0.71, while the estimated theoretical value from Nefiodov [49] is 0.90 as obtained from Fig. 2.10 or calculated from Eq. (2.46) based on a Sommerfeld

parameter κ of 0.96. For the sake of comparison, the ratio R'' in the case of fully-stripped oxygen at an energy of 2.38 MeV/u [54] was found to be 0.50 ± 0.07 compared to the value of 0.7 from Nefiodov [49] based on $\kappa = 0.82$. As seen, the prediction of Nefiodov [49] for the KL-RDEC/KK-RDEC cross-section ratio as the only available approach to predict such a ratio is in good agreement with the corresponding measured ratio. The relatively-small discrepancy between his prediction and the measured value might be attributed to the poor statistics due to the low count rate of RDEC measurement. However, Fig. 2.10 predicts that the cross section of RDEC into the excited state $1s^1 2s^1$ is enhanced drastically for slow collisions ($\kappa \gg 1$) compared to the cross section of RDEC into the projectile K-shell. This was the motivation for Nefiodov to predict the RDEC cross section into the projectile excited state $1s^1 2s^1$ as given by Eq. (2.46). Hence, the theory is expected to work fine in the domain $\kappa \gg 1$ versus $\kappa = 0.96$ for this work, which is very close to the slow-collision domain, which in turn accounts for this small discrepancy between the calculated (0.90) and the measured (0.83) values of KL-RDEC/KK-RDEC ratios. The values obtained for the KL-RDEC/KK-RDEC cross-section ratio are indicated in Table 5.6 for the available theories compared to all the RDEC experiments conducted up to the moment.

TABLE 5.5. Measured versus calculated KL-RDEC and KK-RDEC cross sections for the four conducted RDEC experiments. The abbreviations Che, Nef, Mik, Yak, PDB, and Exp stand for Chernovskaya, Nefiodov, Mikhailov, Yakhontov, principle of detailed balance, and experiment, respectively.

Z_p	E_p (MeV/u)	κ	Z_t	$\sigma_{RDEC}^{1s^1 2s^1}$ (mb/atom)			$\sigma_{RDEC}^{1s^2}$ (mb/atom)				
				Che [50]	Nef [49]	Exp	Che [50]	Mik [47]	Yak [45]	PDB [12]	Exp
18 [51]	11.4	0.84	6	--- ---	2.2	---	120[7] 4.3[8]	3.2[9] 0.003[10]	1.85	45	≤5.2
92 [52]	297	0.84	18	--- ---	6×10^{-4}	---	1.73 0.003	0.025 8×10^{-7}	5000[11] 0.001[12]	5.8	≤10
8 [54]	2.38	0.82	6	50[7] 2[8]	112	2300 ±1300	550 19	160 0.13	137	228	3200 ±1900
9 [61]	2.21	0.96	6	--- ---	194	1600 ±980	940 35	221 0.19	121	180	1900 ±1200

[7] First approximation involving the whole atom
[8] Second approximation involving only the K-shell
[9] For the capture of two K-shell target electrons
[10] For the capture of two valence target electrons
[11] Relativistic
[12] Nonrelativistic

TABLE 5.6. Measured versus calculated RDEC/REC cross section ratios $R = \sigma_{RDEC}^{1s^2} / \sigma_{REC}^{1s}$ and $R' = \sigma_{RDEC}^{1s^1 2s^1} / \sigma_{REC}^{1s}$ as well as KL-RDEC/KK-RDEC cross section ratio $R'' = \sigma_{RDEC}^{1s^1 2s^1} / \sigma_{RDEC}^{1s^2}$ for the four conducted RDEC experiments. The abbreviations Mik, Yak, Mir, Amu, PDB, Nef, and Exp stand for Mikhailov, Yakhontov, Miraglia, Amusia, principle of detailed balance, Nefiodov, and experiment, respectively.

Z_p	E_p (MeV/u)	κ	Z_t	R ($\times 10^{-6}$)						R' ($\times 10^{-6}$)		R''	
				Mik [47]	Yak [45]	Mir [91]	Amu [90]	PDB [12]	Exp	Nef [49]	Exp	Nef [49]	Exp
18 [51]	11.4	0.84	6	9	3.6	~310	~31	45	≤ 3.1	2	---	0.63	---
92 [52]	297	0.84	18	0.023	0.001	---	---	5.8	---	6×10^{-4}	---	0.63	---
8 [54]	2.38	0.82	6	454	208	---	---	228	7400 ±3700	99	5300 ±2700	0.70	0.50 ±0.07
9 [61]	2.21	0.96	6	503	115	---	---	180	3700 ±2200	138	3100 ±1900	0.90	0.83 ±0.71

CHAPTER VI

CONCLUSION

In the current work, the process of RDEC was observed in collisions of fully-stripped fluorine ions with a thin carbon foil at a collision energy of 2.21 MeV/u. Analysis for the C target foil showed evidence for contamination with Si, causing overlapping between Si Kα line and the structure dedicated to K-REC. The total number of REC counts corresponding to the Bethe-Salpeter [67] value was found and utilized to determine how the Si Kα line had to be normalized and then subtracted so that the counts leftover give the REC cross section obtained from Bethe-Salpeter [67].

The measured RDEC cross sections for this work showed excellent consistency with the first observation of RDEC for fully-stripped oxygen ions in 2010 [54], as well as fair agreement with the theoretical approach introduced by Chernovskaya [50]. The measured ratios $R = \sigma_{RDEC}^{1s^2} / \sigma_{REC}^{1s}$ and $R' = \sigma_{RDEC}^{1s^1 2s^1} / \sigma_{REC}^{1s}$ for this work were found to be factors of 2.0 and 1.7, respectively, smaller than the measured values in the case of the O^{8+} experiment [54], which can also be considered good consistency. The predicted value of $R = \sigma_{RDEC}^{1s^2} / \sigma_{REC}^{1s}$ by Mikhailov [47] was found to be in fair agreement with the current measurements, while the value of $R' = \sigma_{RDEC}^{1s^1 2s^1} / \sigma_{REC}^{1s}$ predicted by Nefiodov [49] was found to be three times worse.

Normalization of REC to the Bethe-Salpeter [67] enabled to obtain $R = \sigma_{RDEC}^{1s^2} \big/ \sigma_{REC}^{1s}$ more in agreement with Mikhailov [47] than with the values calculated from the principle of detailed balance [12] and Yakhontov [45].

The current work gives a ratio for $R'' = \sigma_{RDEC}^{1s^1 2s^1} \big/ \sigma_{RDEC}^{1s^2}$ that is compatible with the measured value in case of fully-stripped oxygen ions [54] and in fair agreement with Nefiodov [49]. The main origin of discrepancy between theory and experiment is attributed to the validity of the theory in only a certain domain of collision energies as well as to the poor statistics of the collected RDEC counts.

NRC was found to accompany REC as independent processes where two target electrons are captured to a projectile bound state, one radiatively (REC) and the other nonradiatively (NRC), which caused about 5.2% of the total REC counts to be associated with double capture. On the other hand, a crossover of 33.4% of the total REC counts was found from the single capture channel to the no capture channel, which was the origin of REC counts in the x rays associated with no capture. The leftover of 61.4% of the total REC counts had to appear in the single capture channel as the normal channel of REC. Contributions from all the background processes including DREC and pileup were found to be negligible.

Foils free of contaminations are preferred to be used in upcoming experiments, and also more experiments are needed to determine accurately the best experimental conditions to observe RDEC using different systems of collisions.

Clearly, experimental conditions and longer beam times of data collection that yield better statistics are desirable in order to conclusively test theoretical predictions.

APPENDIX A

LIST OF ABBREVIATIONS

TABLE A.1. Abbreviations used in the present dissertation in the order they showed.

Acronym	Full name
PE	photoelectric effect
PI	photoionization
e-e	electron-electron
γ-e	photon-electron
PDB	principle of detailed balance
RR	radiative recombination
REC	radiative electron capture
H-like	hydrogen-like (singly-charged)
DPI	double photoionization
VUV	vacuum ultraviolet
RDEC	radiative double electron capture
GSI	Gesellschaft für Schwerionenforschung mbH
WMU	Western Michigan University
PIXE	proton-induced x-ray emission
CGS	centimeter-gram-second system of measurements
HF	Hartree Fock
K-REC	radiative electron capture into the projectile K-shell
DCS	differential cross section
KK-RDEC	radiative double electron capture into the projectile K-shell
KL-RDEC	radiative double electron capture into the projectile K- and L-shells
NRC	nonradiative electron capture
QED	quantum electrodynamics
LPA	line-profile approach

e-n	electron-nucleus
NB	nuclear bremsstrahlung
DREC	double radiative electron capture
RECC	radiative electron capture to continuum
RI	radiative ionization
SEB	secondary electron bremsstrahlung
AB	atomic bremsstrahlung
QFEB	quasi-free electron bremsstrahlung
PB	primary bremsstrahlung
DDCS	double-differential cross section
PBS	polarization bremsstrahlung
n-n	nucleus-nucleus
TDCS	triply-differential cross section
SNICS	source of negative ions by cesium sputtering
FWHM	full width at half-maximum
DAQ	data acquisition
NIM	nuclear instrumentation module
TFA	timing filter amplifiers
CFD	constant fraction discriminators
LGS	linear gate and stretcher
SCA	single channel analyzer
TAC	time-to-amplitude converter
ADC	analog-to-digital converter
GDG	gate and delay generator
LA	level adaptor
Si(Li)	silicon-lithium
NSCL	National Superconducting Cyclotron Laboratory
CERN	European Organization for Nuclear Research
LHC	Large Hadron Collider
ROOT	data analysis framework developed by CERN

BIBLIOGRAPHY

[1] H. Hertz, *Ann. Phys.* **267**, 983 (1887).

[2] R. H. Pratt, Akiva Ron, and H. K. Tseng, *Rev. Mod. Phys.* **45**, 273 (1973).

[3] Hughes, *Bull. Nat. Res. Coun.* **2**, 86 (1921).

[4] R. C. Williamson, *Phys. Rev.* **21**, 107 (1923).

[5] D. W. Missavage, S. T. Manson, and G. R. Daum, *Phys. Rev. A* **15**, 1001 (1977).

[6] G. B. Pradhan, J. Jose, P. C. Deshmukh, V. Radojevic, and S. T. Manson, *Phys. Rev. A* **80**, 053416 (2009).

[7] M. S. Pindzola, J. A. Ludlow, and J. Colgan, *Phys. Rev. A* **81**, 063431 (2010).

[8] A. M. Covington, A. Aguilar, I. R. Covington, M. Gharaibeh, C. A. Shirley, R. A. Phaneuf, I. Alvarez, C. Cisneros, G. Hinojosa, J. D. Bozek, I. Dominguez, M. M. Sant'Anna, A. S. Schlachter, N. Berrah, S. N. Nahar, and B. M. McLaughlin, *Phys. Rev. Lett.* **87**, 243002 (2001).

[9] G. A. Alna'washi, M. Lu, M. Habibi, R. A. Phaneuf, A. L. D. Kilcoyne, A. S. Schlachter, C. Cisneros, and B. M. McLaughlin, *Phys. Rev. A* **81**, 053416 (2010).

[10] V. B. Berestetskii, E. M. Lifshitz, L. P. Pitaevskii, Relativistic Quantum Theory, Part 1, Pergamon, Oxford (1971).

[11] L. D. Landau and E. M. Lifszyc, Mechanika kwantowa and Teoria nierelatywistyczna, PWN Warszawa (1979).

[12] H. F. Beyer and V. P. Shevelko, *Introduction to the Physics of Highly Charged Ions, IoP Publishing, Boston,* Philadelphia (2003).

[13] A. Kramers, *Philos. Mag.* **46**, 836 (1923).

[14] H. W. Schnopper, H. D. Betz, J. P. Delvaille, K. Kalata, A. R. Sohval, K. W. Jones, and H. E. Wegner, *Phys. Rev. Lett.* **29**, 898 (1972).

[15] A. Ichihara, T. Shirai, and J. Eichler, *Phys. Rev. A* **49**, 1875 (1994).

[16] R. Shakeshaft, *Phys. Rev. A* **20**, 779 (1979).

[17] H. Tawara, P. Richard, and K. Kawatsura, *Phys. Rev. A* **26**, 154 (1982).

[18] T. Stöhlker, C. Kozhuharov, A. E. Livingston, P. H. Mokler, Z. Stachura, and A. Warczak, *Z. Phys. D* **23**, 121 (1992).

[19] T. Stöhlker, H. Giessel, H. Irnich, T. Kandler, C. Kozhuharov, P. Mokler, G. Muenzenberg, F. Nickel, C. Scheidenberger, T. Suzuki, M. Kucharski, A. Warczak, P. Rymuza, Z. Stachura, A. Kriessbach, and T. Shirai, *Phys. Rev. Lett.* **73**, 3520 (1994).

[20] C. Blancard, Ph. Cosse, G. Faussurier, J.-M. Bizau, D. Cubaynes, N. El Hassan, S. Guilbaud, M. M. Al Shorman, E. Robert, X.-J. Liu, C. Nicolas, and C. Miron, *Phys. Rev. A* **85**, 043408 (2012).

[21] Z. Smit, M. Kregar, and D. Glavic-Cindro, *Phys. Rev. A* **40**, 6303 (1989).

[22] P. Lablanquie, J. H. D. Eland, I. Nenner, P. Morin, J. Delwiche, and M. J. Huhin-Franskin, *Phys. Rev. Lett.* **58**, 992 (1987).

[23] H. Kossmann, V. Schmidt, and T. Andersen, *Phys. Rev. Lett.* **60**, 1266 (1988).

[24] S. D. Price and J. H. D. Eland, *J. Phys. B* **22**, L153 (1989).

[25] S. L. Carter and H. P. Kelly, *Phys. Rev. A* **24**, 170 (1981).

[26] S. N. Tiwary, *J. Phys. B* **15**, L323 (1982).

[27] O. Schwarzkopf, B. Krassig, J. Elminger, and V. Schmidt, *Phys. Rev. Lett.* **70**, 3008 (1993).

[28] N. Berrah, F. Heiser, R. Wehlitz, J. Levin, S. B. Witfield, J. Viefhaus, I. A. Sellin, and U. Becker, *Phys. Rev. A* **48**, R1733 (1993).

[29] J. A. R. Samson, Z.-X. He, Y. Lin, and G. N. Haddad, *J. Phys. B* **27**, 887 (1994).

[30] J. A. R. Samson, W. C. Stolte, Z. X. He, J. N. Cutler, Y. Lu, and R. J. Bartlett, *Phys. Rev. A* **57**, 1906 (1998).

[31] G. Turri, L. Avaldi, P. Bolognesi, R. Camilloni, M. Coreno, J. Berakdar, A. S. Kheifets, and G. Stefani, *Phys. Rev. A* **65**, 034702 (2002).

[32] S. L. Carter and H. P. Kelly, *Phys. Rev. A* **16**, 1525 (1977).

[33] N. Saito and I. H. Suzuki, *Phys. Scr.* **45**, 253 (1992).

[34] K.-H. Schartner, G. Mentzel, B. Magel, B. Moebus, A. Ehresmann, F. Vollweiler, and H. Schmoranzer, *J. Phys. B* **26**, L445 (1993).

[35] P. Lablanquie, J. H. D. Eland, I. Nenner, P. Morin, J. Delwiche, and M. -J. Hubin-Franskin, *Phys. Rev. Lett.* **58**, 992 (1987).

[36] H. Le Roum and C. Dal Cappello, *Phys. Rev. A* **43**, 318 (1991).

[37] A. Dalgarno and H. R. Sadeghpour, *Comments At. Mol. Phys.* **30**, 143(1994).

[38] J. Briggs and V. Schmidt, *J. Phys. B* **33**, R1 (2000).

[39] V. A. Yerokhin and A. Surzhykov, *Phys. Rev. A* **84**, 032703 (2011).

[40] A. Huetz, P. Selles, D. Waymel, and J. Mazeau, *J. Phys. B* **24**, 1917 (1991).

[41] D. Chattarji and C. Sur, *Phys. Rev. A* **65**, 012702 (2001).

[42] H. R. Sadeghpour and A. Dalgarno, *Phys. Rev. A* **47**, R2458 (1993).

[43] A. S. Kheifets, Igor Bray, and J. Hoszowska, *Phys. Rev. A* **79**, 042504 (2009).

[44] V. L. Yakhontov and M. Y. Amusia, *Phys. Lett. A* **221**, 328 (1996).

[45] V. L. Yakhontov and M. Y. Amusia, *Phys. Rev. A* **55**, 1952 (1997).

[46] E. G. Drukarev, A. I. Mikhailov, I. A. Mikhailov, and W. Scheid, *Phys. Rev. A* **76**, 062701 (2007).

[47] A. I. Mikhailov, I. A. Mikhailov, A. Nefiodov, G. Plunien, and G. Soff, *Phys. Lett. A* **328**, 350 (2004).

[48] A. I. Mikhailov, I. A. Mikhailov, A. N. Moskalev, A. V. Nefiodov, G. Plunien, and G. Soff, *Phys. Rev. A* **69**, 032703 (2004).

[49] A. V. Nefiodov, A. I. Mikhailov, and G. Plunien, *Phys. Lett. A* **346**, 158 (2005).

[50] E. A. Chernovskaya, O. Yu. Andreev, and L. N. Labzowsky, *Phys. Rev. A* **84**, 062515 (2011).

[51] A. Warczak, M. Kucharski, Z. Stachura, H. Giessel, H. Irnich, T. Kandler, C. Kozhuharov, P. Mokler, G. Muenzenberg, F. Nickel, C. Scheidenberger, T. Stöhlker, T. Suzuki, and P. Rymuza, *Nucl. Instr. Meth. Phys. Res. B* **98**, 303 (1995).

[52] G. Bednarz, D. Sierpowski, T. Stöhlker, A. Warczak, H. B. b, F. Bosch, A. Braeuning-Demian, H. Braeuning, X. Cai, A. Gumberidze, S. Hagmann, C. Kozhuharov, D. Liesen, X. Ma, P. Mokler, A. Muthig, Z. Stachura, and S. Toleikis, *Nucl. Instr. Meth. Phys. Res. B* **205**, 573 (2003).

[53] A. Simon, J. A. Tanis, T. Elkafrawy, and A. Warczak, *J. Phys.: Conf. Ser.* **194**, 082044 (2009).

[54] A. Simon, A. Warczak, T. Elkafrawy, and J. A. Tanis, *Phys. Rev. Lett.* **104**, 123001 (2010).

[55] A. Simon, A. Warczak, and J. A. Tanis, *AIP Conf. Proc.* **1336**, 87 (2011).

[56] A. Simon, A. Warczak, and J. A. Tanis, *Phys. Scr.* **T144**, 014024 (2011).

[57] A. Simon, J. A. Tanis, T. Elkafrawy, and A. Warczak, *J. Phys.: Conf. Ser.* **388**, 012034 (2012).

[58] T. Elkafrawy, J. A. Tanis, A. Simon, and A. Warczak, *Bull. Am. Phys. Soc.* **56**(5), 182 (2011).

[59] T. Elkafrawy, J. A. Tanis, A. Simon, and A. Warczak, *Bull. Am. Phys. Soc.* **57**(5), 46 (2012).

[60] T. Elkafrawy, A. Warczak, A. Simon, and J. A. Tanis, *J. Phys.: Conf. Ser.* **388**, 082012 (2012).

[61] T. Elkafrawy, A. Warczak, A. Simon, and J. A. Tanis, *AIP Conf. Proc.*, accepted in 2012.

[62] T. Elkafrawy, A. Warczak, A. Simon, and J. A. Tanis, *Phys. Scr.* **T**, accepted in 2012.

[63] F. Biggs, L. B. Mendelsohn, and J. B. Mann, *At. Data Nucl. Data Tables* **16**, 201 (1975).

[64] P. Kienle, M. Kleber, B. Povh, R. M. Diamond, F. S. Stephens, E. Grosse, M. R. Maier, and D. Proetel, *Phys. Rev. Lett.* **31**, 1099 (1973).

[65] H. W. Schnopper, J. P. Delavaille, K. Kalato, A. R. Sohval, M. Abdulwahab, K. W. Jones, and H. E. Wagner, *Phys. Lett. A* **47**, 61 (1974).

[66] M. Stobbe, *Ann. Phys.* **7**, 661 (1930).

[67] H. A. Bethe and E. E. Salpeter, *Handbuch der Physik*, edited by S. Flugge, Springer, Berlin Vol. **35**, (1957).

[68] D. R. Bates and R. McCarroll, *Adv. Phys.* **11**, 39 (1962).

[69] J. S. Briggs and K. Dettmann, *Phys. Rev. Lett.* **33**, 1123 (1974).

[70] A. R. Sohval, J. P. Delvaille, K. Kalata, K. Kirby-Docken, and H. W. Schnopper, *J. Phys. B* **9**, L25 (1976).

[71] E. Spindler, H. -D. Betz, and F. Bell, *Phys. Rev. Lett.* **42**, 832 (1979).

[72] D. H. Jakubassa-Amundsen, R. Hoppler, and H. -D. Betz, *J. Phys. B* **17**, 3943 (1984).

[73] S. Andriamonje, M. Chevallier, C. Cohen, J. Dural, M. J. Gaillard, R. Genre, M. Hage-Ali, R. Kirsch, A. L'Hoir, D. Mazuy, J. Mory, J. Moulin, J. C. Poizat, J. Remillieux, D. Schmaus, and M. Toulemonde, *Phys. Rev. Lett.* **59**, 2271 (1987).

[74] J. A. Tanis and S. M. Shafroth, *Phys. Rev. Lett.* **40**, 1174 (1978).

[75] E. Spindler, H. -D. Betz, and F. Bell, *Phys. Rev. Lett.* **42**, 832 (1979).

[76] J. A. Tanis, W. W. Jacobs, and S. M. Shafroth, *Phys. Rev. A* **22**, 483 (1980).

[77] J. A. Tanis, S. M. Shafroth, J. E. Willis, and J. R. Mowat, *Phys. Rev. A* **23**, 366 (1981).

[78] R. Anholt, S. A. Andriamonje, E. Morenzoni, Ch. Stoller, J. D. Molitoris, W. E. Meyerhof, H. Bowman, J. -S. Xu, Z. -Z. Xu, J. O. Rasmussen, and D. H. H. Hoffmann, *Phys. Rev. Lett.* **53**, 234 (1984).

[79] T. Stöhlker, C. Kozhuharov, P. H. Mokler, A. Warczak, F. Bosch, H. Geissel, R. Moshammer, C. Scheidenberger, J. Eichler, A. Ichihara, T. Shirai, Z. Stachura, and P. Rymuza, *Phys. Rev. A* **51**, 2098 (1995).

[80] M. Kleber and D. H. Jakubassa, *Nucl. Phys. A* **252**, 15242 (1975).

[81] R. Anholt, Ch. Stoller, J. D. Molitoris, D. W. Spooner, E. Morenzoni, S. A. Andriamonje, W. E. Meyerhof, H. Bowman, J. -S. Xu, Z. -Z. Xu, J. O. Rasmussen, and D. H. H. Hoffmann, *Phys. Rev. A* **33**, 2270 (1986).

[82] J. C. Slater, Quantum Theory of Atomic Structure, McGraw–Hill, New York Vol. **I** (1960).

[83] D. J. McLaughlin and Y. Hahn, *Phys. Rev. A* **43**, 1313 (1991).

[84] T. Stöhlker, T. Ludziejewski, H. Reich, F. Bosch, R. W. Dunford, J. Eichler, B. Franzke, C. Kozhuharov, G. Menze, P. H. Mokler, F. Nolden, P. Rymuza, Z. Stachura, M. Steck, P. Swiat, A. Warczak, and T. Winkler, *Phys. Rev. A* **58**, 2043 (1998).

[85] A. Gojska, D. Chmielewska, P. Rymuza, J. Rzadkiewicz, Z. Sujkowski, T. Adachi, H. Fujita, Y. Fujita, Y. Shimbara, K. Hara, Y. Shimizu, H. P. Yoshida, Y. Haruyama, J. Kamiya, H. Ogawa, M. Saito, and M. Tanaka, *Eur. Phys. J. A* **27**, s01, 181 (2006).

[86] H. Tawara, T. Azuma, T. Ito, K. Komaki, Y. Yamazaki, T. Matsuo, T. Tonuma, K. Shima, A. Kitagawa, and E. Takada, *Phys. Rev. A* **55**, 808 (1997).

[87] R. Schule, H. Schmidt-Bocking, and I. Tserruya, *J. Phys. B* **10**, 889 (1977).

[88] J. Eichler, A. Ichihara, and T. Shirai, *Phys. Rev. A* **51**, 3027 (1995).

[89] K. Hino and T. Watanabe, *Phys. Rev. A* **36**, 5862 (1987).

[90] M. Ya. Amusia, E. G. Drukarev, V. G. Gorshkov, and M. O. Kazachkov, *J. Phys. B* **8**, 1248 (1975).

[91] J. E. Miraglia and M. S. Gravielle, XVI ICPEAC, Brighton, *Book of Abstracts*, pp. 517 (1987).

[92] Wm. J. Veigele, *At. Data Nucl. Data Tables* **5**, 51 (1973).

[93] K. Zaharakis, R. L. Watson, and V. Horvat, at Texas A&M (2001), unpublished.

[94] N. Winters, A. Warczak, J. A. Tanis, A. Gumberidze, C. Kozhuharov, S. Hagmann, P. M. Hillenbrand, N. Petridis, R. Reuschl, M. Schwemlein, R. Strzalka, D. Sierpowski, U. Spillmann, S. Trotsenko, G. Weber, D. F. A. Winters, Z. Yin, and T. Stöhlker, *HCI Conference Book of Abstracts*, pp. A-b33 (2012).

[95] A. I. Akhiezer and V. B. Berestetskii, Quantum Electrodynamics, Wiley, New York, (1974).

[96] S. A. Boman, E. M. Bernstein, and J. A. Tanis, *Phys. Rev. A* **39**, 4423 (1989).

[97] J. A. Tanis, E. M. Bernstein, M. W. Clark, S. M. Ferguson, and R. N. Price, *Phys. Rev. A* **43**, 4723 (1991).

[98] O. Yu. Andreev, L. N. Labzowsky, G. Plunien, and D. A. Solovyev, *Phys. Rep*. **455**, 135 (2008).

[99] M. Komma and W. Nakel, *J. Phys. B* **15**, 1433 (1982).

[100] F. Folkmann, K. O. Groeneveld, R. Mann, G. Nolte, S. Schumann, and R. Spohr, *Z. Phys. A* **275**, 229 (1975).

[101] H. W. Koch and J. W. Motz, *Rev. Mod. Phys.* **31**, 920 (1959).

[102] E. Haug and W. Nakel, "*The Elementary process of bremsstrahlung", World Scientific Lecture Notes in Physics* Vol. **73**, (2004).

[103] W. C. Roentgen, *Nature* **53**, 274 (1896).

[104] F. Folkmann, C. Gaarde, T. Huus, and K. Kemp, *Nucl. Instr. Meth.* **116**, 487 (1974).

[105] F. Folkmann, K. Cramon, and N. Hertel, *Nucl. Instr. Meth. Phys. Res. B* **3**, 11 (1984).

[106] K. W. Rothe, P. F. M. Koehler, and E. H. Thorndike, *Phys. Rev. Lett.* **16**, 1118 (1966).

[107] H. A. Bethe and W. Heitler, *Proc. R. Soc. (London) Ser. A* **146**, 83 (1934).

[108] W. Duane and F. L. Hunt, *Phys. Rev.* **6**, 166 (1915).

[109] H. A. Kramers, *Phil. Mag.* **46**, 836 (1923).

[110] C. T. Ulrey, *Phys. Rev.* **11**, 401 (1918).

[111] D. Jakubassa-Amundsen, *J. Phys. B* **16**, 1767 (1983).

[112] D. Jakubassa-Amundsen, *J. Phys. B* **20**, 325 (1987).

[113] G. Bednarz, A. Warczak, H. Tawara, T. Azuma, K. Komaki, and E. Takada, *Eur. Phys. J. D* **4**, 271 (1998).

[114] D. Jakubassa-Amundsen, *J. Phys. B* **36**, 1971 (2003).

[115] D. Jakubassa-Amundsen, *Rad. Phys. Chem.* **75**, 1319 (2006).

[116] D. Jakubassa-Amundsen, *Eur. Phys. J. D* **41**, 267 (2007).

[117] M. Nofal, S. Hagmann, T. Stöhlker, D. H. Jakubassa-Amundsen, Ch. Kozhuharov, X. Wang, A. Gumberidze, U. Spillmann, R. Reuschl, S. Hess, S. Trotsenko, D. Banas, F. Bosch, D. Liesen, R. Moshammer, J. Ullrich, R.

Dorner, M. Steck, F. Nolden, P. Beller, H. Rothard, K. Beckert, and B. Franczak, *Phys. Rev. Lett.* **99**, 163201 (2007).

[118] R. Anholt and T. K. Saylor, *Phys. Lett. A* **56**, 455 (1976).

[119] K. Ishii, *Rad. Phys. Chem.* **75**, 1135 (2006).

[120] K. Ishii, S. Morita, and H. Tawara, *Phys. Rev. A* **13**, 131 (1976).

[121] M. Ya. Amusia, *Comments At. Mol. Phys.* **11**, 123 (1982).

[122] K. Ishii and S. Morita, *Phys. Rev. A* **30**, 2278 (1984).

[123] R. Anholt and H. Gould, *Adv. At. Mol. Phys.* **22**, 315 (1986).

[124] C. R. Vane, S. Datz, P. F. Dittner, J. Giese, N. L. Jones, H. F. Krause, T. M. Rosseel, and R. S. Peterson, *Phys. Rev. A* **49**, 147 (1994).

[125] A. Yamadera, K. Ishii, K. Sera, M. Sebata, and S. Morita, *Phys. Rev. A* **23**, 24 (1981).

[126] T. C. Chu, K. Ishii, A. Yamadera, M. Sebata, and S. Morita, *Phys. Rev. A* **24**, 1720 (1981).

[127] P. Kienle, M. Kleber, B. Povh, R. M. Diamond, F. S. Stephens, E. Grosse, M. R. Maier, and D. Proetel, *Phys. Rev. Lett.* **31**, 1099 (1973).

[128] H. W. Schnopper, J. P. Delvaille, K. Kalata, A. R. Sohval, M. Abdulwahab, K. W. Jones, and H. E. Wegner, *Phys. Lett. A* **47**, 61 (1974).

[129] K. Ishii and S. Morita, *Nucl. Instr. Meth. Phys. Res. B* **22**, 68 (1987).

[130] K. Dettmann, K. G. Harrison, and M. W. Lucas, *J. Phys. B* **7**, 269 (1974).

[131] R. Shakeshaft and L. Spruch, *Rev. Mod. Phys.* **51**, 369 (1979).

[132] A. Salin, *J. Phys. B* **2**, 631 (1969).

[133] G. B. Crooks and M. E. Rudd, *Phys. Rev. Lett.* **25**, 1599 (1970).

[134] J. Macek, *Phys. Rev. A* **1**, 235 (1970).

[135] Y. Ning, B. He, C. L. Liu, J. Yan, and J. G. Wang, *Phys. Rev. A* **72**, 022702 (2005).

[136] E. Merzbacher and H. W. Lewis, In: S. Flugge, (Ed.), *Ecyclopedia of Physics*, *Springer, Berlin* Vol. **34**, 166 (1958).

[137] M. Inukoti, *Rev. Mod. Phys.* **43**, 297 (1971).

[138] H. Tawara, T. Azuma, T. Ito, K. Komaki, Y. Yamazaki, T. Matsuo, T. Tonuma, K. Shima, A. Kitagawa, and E. Takada, *Phys. Rev. A* **55**, 808 (1997).

[139] T. Azuma, T. Ito, K. Komaki, H. Tawara, T. Matsuo, T. Tonuma, K. Murakami, and A. Warczak, *Phys. Scr.* **T73**, 250 (1997).

[140] K. Ishii, M. Kamiya, K. Sera, S. Morita, and H. Tawara, *Phys. Rev. A* **15**, 2126 (1976).

[141] K. Ishii, *Nucl. Instr. Meth. Phys. Res. B* **99**, 163 (1995).

[142] E. V. Gnatchenko, A. N. Nechay, V. N. Samovarov, and A. A. Tkachenko, *Phys. Rev. A* **82**, 012702 (2010).

[143] V. M. Buimistrov and L. I. Trakhtenberg, *Sov. Phys.-JETP* **42**, 55 (1975).

[144] M. Ya. Amusia, A. S. Baltenkov, A. A. Paiziev, *Sov. Phys.-JETP Lett.* **24**, 332 (1976).

[145] M. S. Pindzola and H. P. Kelly, *Phys. Rev. A* **14**, 204 (1976).

[146] B. A. Zon, *Sov. Phys.-JETP* **46**, 65 (1977).

[147] G. Wendin and K. Nuroh, *Phys. Rev. Lett.* **39**, 48 (1977).

[148] M. C. Pacher and J. E. Miraglia, *Phys. Rev. A* **41**, 2574 (1990).

[149] K. Ishii and S. Morita, *Phys. Rev. A* **30**, 2278 (1984).

[150] K. Alder, A. Bohr, T. Huus, B. Mottelson, and A. Winther, *Rev. Mod. Phys.* **28**, 432 (1956).

[151] D. H. Jakubassa and M. Kleber, *Z. Phys. A* **273**, 29 (1975).

[152] H. P. Trautvetter, J. S. Greenberg, and P. Vincent, *Phys. Rev. Lett.* **37**, 202 (1976).

[153] S. Jeon, J. Kapusta, A. Chikanian, and J. Sandweiss, *Phys. Rev. C* **58**, 1666 (1999).

[154] W. Heitler, The Quantum Theory of Radiation, Clarendon, Oxford (1954).

[155] K. Ishii and S. Morita, *Phys. Rev. A* **30**, 2278 (1984).

[156] K. Ishii, T. Satoh, S. Matsuyama, H. Yamazaki, Y. Tokai, A. Sugimoto, K. Yamamoto, *Int. J. PIXE* **9**, 1 (1999).

[157] J. W. Motz, *Phys. Rev.* **100**, 1560 (1955).

[158] D. H. Rester, *Nucl. Phys. A* **118**, 129 (1968).

[159] E. Haug, *Phys. Lett. A* **54**, 339 (1975).

[160] W. Nakel and E. Pankau, *Phys. Lett. A* **38**, 307 (1972).

[161] W. Nakel and E. Pankau, *Phys. Lett. A* **44**, 65 (1973).

[162] O. Scherzer, *Ann. Phys. (Leipzig)* **13**, 137 (1932).

[163] I. Hodes, *Ph.D. Thesis*, University of Chicago (1953), unpublished.

[164] W. Nakel, *Phys. Lett.* **22**, 614 (1966).

[165] W. Nakel, *Phys. Lett. A* **25**, 569 (1967).

[166] W. Nakel, *Z. Physik A* **214**, 168 (1968).

[167] E. Haug and M. Keppler, *J. Phys. B* **17**, 2075 (1984).

[168] M. Komma and W. Nakel, *J. Phys. B* **15**, 1433 (1982).

[169] L. H. Lanzl and A. O. Hanson, *Phys. Rev.* **83**, 959 (1951).

[170] J. Eichler and T. Stöhlker, *Phys. Rep.* **439**, 1 (2007).

[171] A. S. Schlachter, J. W. Stearns, W. G. Graham, K. H. Berkner, R. V. Pyle, and J. A. Tanis, *Phys. Rev. A* **27**, 3372 (1983).

[172] W. E. Meyerhof, *Phys. Rev. A* **32**, 3291 (1985).

[173] J. H. McGuire and L. Weaver, *Phys. Rev. A* **16**, 41 (1977).

[174] P. Gombas, *Statistische Theorie des Atoms, Springer, Wien* (1949).

[175] G. Bednarz, D. Sierpowski, T. Stöhlker, A. Warczak, H. Beyer, F. Bosch, A. Brauning-Demian, H. Brauning, X. Cai, A. Gumberidze, S. Hagmann, C. Kozhuharov, D. Liesen, X. Ma, P. H. Mokler, A. Muthig, Z. Stachura, S. Toleikis, *Nucl. Instr. Meth. Phys. Res. B* **205**, 573 (2003).

[176] E. B. Saloman, J. H. Hubbell, and J. H. Scofield, *At. Data Nucl. Data Tables* **38**, 1 (1988).

[177] R. J. Van de Graaff, J. G. Trump, and W. W. Buechner, *Rep. Prog. Phys.* **11**, 1 (1948).

[178] R. J. Van de Graaff, *Phys. Rev.* **38**, 1919 (1931).

[179] Particle Accelerator Physics I: Basic Principles and Linear Beam Dynamics, H. Wiedermann, *Springer, Verlag, Berlin* (1999), ISBN 3540565507.

[180] D. A. Edwards and M. J. Syphers, *An introduction to the physics of high energy accelerators, Wiley series in beam physics and accelerator technology* (1993), ISBN 0471551635.

[181] http://tesla.physics.wmich.edu/acceleratorlab/pic/accelerator/Accelerator_map.jpg

[182] http://tesla.physics.wmich.edu/ResearchFacilities.php?PG=1&SC=1

[183] W. H. Trzaska, V. Lyapin, T. Alanko, M. Mutterer, J. Raisanen, G. Tjurin, and M. Wojdyr, *Nucl. Inst. Meth. Phys. Res. B* **195**, 147 (2002).

[184] SRIM, http://www.srim.org/

[185] ORTEC, www.ortec-online.com/download/SLP.pdf

[186] ORTEC, http://www.ortec-online.com/download/Overview-of-Semiconductor-Photon-Detectors.pdf

[187] ORTEC, http://www.ortec-online.com/download/ULTRA.pdf

[188] ORTEC, http://www.ortec-online.com/Solutions/RadiationDetectors/si-charged-particle-detectors-data-summary-selection-chart.aspx

[189] http://www-esd.fnal.gov/esd/catalog/main/egg/ad811-spec.htm

[190] NSCL, http://docs.nscl.msu.edu/daq/spectcl/

[191] http://spectcl.sourceforge.net/

[192] ROOT data analysis framework developed by CERN, http://root.cern.ch/drupal/

[193] http://na49info.web.cern.ch/na49info/

[194] R. L. Kauffman, J. H. McGuire, and P. Richard, *Phys. Rev. A* **8**, 1233 (1973).

[195] J. McWherter, D. K. Olsen, H. H. Wolter, and C. Fred Moore, *Phys. Rev. A* **10**, 200 (1974).

[196] http://physics.nist.gov

[197] Handbook of Chemistry & Physics, ed. 72nd. http://www.hbcpnetbase.com/.